NASA Technical Paper 2690

February 1987

Solar Array Flight Experiment/Dynamic Augmentation Experiment

Leighton E. Young
and Homer C. Pack, Jr.

NASA

NASA Technical Paper 2690

1987

Solar Array Flight Experiment/Dynamic Augmentation Experiment

Leighton E. Young
and Homer C. Pack, Jr.

George C. Marshall Space Flight Center
Marshall Space Flight Center, Alabama

NASA
National Aeronautics
and Space Administration

Scientific and Technical Information Branch

DEDICATION

This report is dedicated to the memory of NASA Mission Specialist Dr. Judith A. Resnik, who died in the Space Shuttle Challenger tragedy, January 28, 1986. The authors and investigators for this report are beholden to Dr. Resnik for her substantial contributions to the success of the Solar Array Flight Experiment/Dynamic Augmentation Experiment program. Dr. Resnik had prime responsibility for operating the SAFE/DAE during STS-41D, a six-day Shuttle mission launched August 30, 1984. Her efforts during the mission facilitated testing in addition to that necessary to achieve basic objectives. Experiment investigators benefited substantially from the additional data which provided technical insight that would otherwise have been unattainable.

The authors and investigators are grateful to the entire crew of Space Shuttle mission STS-41D for their support and contribution to the success of the SAFE/DAE program and the mission. The special interest shown by them in the program, combined with their knowledge and experience in space flight operations, benefited the program substantially and is highly appreciated. They are:

Henry W. Hartsfield, Jr.	Commander
Michael L. Coats	Pilot
Steven A. Hawley	Mission Specialist
Richard M. Mullane	Mission Specialist
Judith A. Resnik	Mission Specialist

Gratitude is expressed to the following individuals of the MSFC data reduction and computation facilities for their timely contributions to analyses of flight data which makes this report possible.

Von L. Burton	MSFC
Dena D. Heflin	New Technology Inc.
John C. Pooley	New Technology Inc.

AUTHORS: Leighton E. Young and Homer C. Pack Jr., MSFC
PRINCIPAL INVESTIGATOR: Leighton E. Young, MSFC
CO-INVESTIGATOR FOR PHOTOGRAMMETRY: Larry Brumfield, LaRC
CO-INVESTIGATOR FOR THE DYNAMIC AUGMENTATION EXPERIMENT: Richard W. Shock, MSFC

ACKNOWLEDGMENTS

The authors and investigators acknowledge the contributions of the individuals listed below who were instrumental in the origination and definition of this experiment.

GOVERNMENT

Anne B. Folsom (Retired)	SAFE	MSFC
Edward A. Gabris	SAFE	NASA Headquarters, OAST
Peggy K. Geddings	SAFE	MSFC
Jim Lazar	SAFE	NASA Headquarters, OAST
Jimmy L. Miller	SAFE	MSFC
Homer C. Pack, Jr.	SAFE	MSFC
Richard A. Smith	SAFE	MSFC
Tyrus M. White	SAFE	MSFC
Leighton E. Young	SAFE	MSFC
Richard R. Adams	Photogrammetry	LaRC
Marcus L. Brumfield	Photogrammetry	LaRC
Henry C. Hill	Photogrammetry	NASA Hdqs., OAST/ Now MSFC
James B. Miller	Photogrammetry	LaRC
Richard S. Pappa	Photogrammetry	LaRC
Dr. James C. Blair	Dynamic Augmentation Exp.	MSFC
Richard F. Carlisle	Dynamic Augmentation Exp.	NASA Headquarters, OAST
Ronald E. Jewell	Dynamic Augmentation Exp.	MSFC
Walter R. McIntosh	Dynamic Augmentation Exp.	MSFC
Charles W. Morris	Dynamic Augmentation Exp.	MSFC
Richard W. Schock	Dynamic Augmentation Exp.	MSFC

INDUSTRY AND UNIVERSITY

Darius T. Chung	SAFE	LMSC
R. V. Elms	SAFE	LMSC
D. E. Lindberg	SAFE	LMSC
Dan Lott	SAFE	LMSC
Dr. Dave Brown	Dynamic Augmentation Exp.	Univ. of Cincinnati
Frank Wargocki	Dynamics Augmentation Exp.	Ball Aerospace Systems Division

TABLE OF CONTENTS

		Page
I.	INTRODUCTION	1
	A. Foreword	1
	B. Background Information	1
II.	SOLAR ARRAY FLIGHT EXPERIMENT (SAFE) DESCRIPTION	2
	A. SAFE Wing	2
	B. SAFE Wing Support Structure	6
	C. SAFE Data Acquisition System (DAS)	6
	D. Photogrammetry	10
III.	DYNAMIC AUGMENTATION EXPERIMENT DESCRIPTION	10
IV.	FLIGHT OPERATIONS	12
	A. Overview	12
	B. Extension/Retraction Testing	12
	C. Dynamic Testing	12
	D. Solar Cell Module Performance Testing	14
V.	EXPERIMENT ANALYSES AND DATA REDUCTION	14
	A. Array Extension/Retraction Testing	14
	B. Dynamics of the Deployed Array	19
	C. Solar Cell Module Performance Testing	41
VI.	CONCLUSIONS AND RECOMMENDATIONS	60

ACRONYMS AND SYMBOLS

A	Ampere
AFD	Aft Flight Deck
AM0	Air-Mass Zero
BSF	Back Surface Field
BSR	Back Surface Reflector
C	Centigrade
CCTV	Closed-Circuit Television
cm	Centimeter
DAE	Dynamic Augmentation Experiment
DAS	Data Acquisition System
DC	Direct Current
deg	Degree
ERA	Eigensystem Realization Algorithm
ft	Feet
FFT	Fast Fourier Transform
g	Gravity
GMT	Greenwich Mean Time
HRES	High Resolution
Hz	Hertz
I	Current
I_{mp}	Maximum Power Point Current
$I_{mp(m)}$	Measured Solar Cell Module Maximum Power Point Current in the Laboratory
$I_{mp(p)}$	Predicted Solar Cell Module Maximum Power Point Current in Space
in.	Inch
I_{sc}	Short-Circuit Current
$I_{sc(m)}$	Measured Solar Cell Module Short-Circuit Current in the Laboratory
$I_{sc(p)}$	Predicted Solar Cell Module Short-Circuit Current in Space
IV	Current Voltage
JSC	Johnson Space Center

kg	Kilogram
K_I	Standard Cell Calibration Correction Factor
K_{Imp}	Temperature Coefficient for Solar Cell Module Maximum Power Point Current
K_{mp}	Temperature Coefficient for Solar Cell Module Maximum Power
K_{Vmp}	Temperature Coefficient for Solar Cell Module Maximum Power Point Voltage
K_{Voc}	Temperature Coefficient for Solar Cell Module Open-Circuit Voltage
Lab	Laboratory
LaRC	Langley Research Center
lbs	Pounds
LMSC	Lockheed Missiles and Space Company
LSS	Large Space Structures
m	Meters
ma	Milliamperes
mil	Milli-inch
min	Minute
mm	Millimeter
mW	Milliwatt
MSFC	George C. Marshall Space Flight Center
NASA	National Aeronautics and Space Administration
OAST	Office of Aeronautics and Space Technology
PCM	Pulse Coded Modulation
PIC	Pyrotechnic Initiator Circuit
$P_{mp(m)}$	Solar Cell Module Maximum Power at the Panel as Derived from Lab Measurements
$P_{mp(p)}$	Predicted Solar Cell Module Maximum Power in Space at the Panel
PSD	Power Spectral Density
Pwr	Power
R	Resistance
Ref.	Reference
RFT	Retroreflector Field Tracker

RMS	Remote Manipulator System
SA	Single Amplitude
SAFE	Solar Array Flight Experiment
SCCF	Solar Cell Calibration Facility
Si	Silicon
T_L	Laboratory Temperature
T_S	Space Temperature
TV	Television
UV	Ultra-Violet
V	Voltage
V_{mp}	Maximum Power Point Voltage
$V_{mp(m)}$	Measured Solar Cell Module Maximum Power Point Voltage in the Laboratory
$V_{mp(p)}$	Predicted Solar Cell Module Maximum Power Point Voltage in Space
V_{oc}	Open-Circuit Voltage
$V_{oc(m)}$	Measured Solar Cell Module Open-Circuit Voltage in the Laboratory
$V_{oc(p)}$	Predicted Solar Cell Module Open-Circuit Voltage in Space
VRCS	Vernier Reaction Control System
VTR	Video Tape Recorder
W	Watts

TECHNICAL PAPER

SOLAR ARRAY FLIGHT EXPERIMENT/DYNAMIC AUGMENTATION EXPERIMENT FINAL REPORT

I. INTRODUCTION

A. Foreword

This report updates and expands the Solar Array Flight Experiment/Dynamic Augmentation Experiment (SAFE/DAE) brochure report, released in the second quarter of Fiscal Year 1985. Since the 1985 brochure report presented the results of a preliminary study of flight data, results contained herein supersede that previously reported. The Lockheed Missiles and Space Company (LMSC) SAFE final Report [1] is an additional source of information pertaining to the experiment. The LMSC report is broader in its coverage of the SAFE design, thermal analyses, and postflight inspections. This report provides a broader and more indepth coverage of solar cell module electrical performance and the structural dynamics experiments.

B. Background Information

In September 1984, NASA tested the Solar Array Flight Experiment/Dynamic Augmentation Experiment (SAFE/DAE) on Shuttle mission STS-41D. This testing qualified advanced solar array and large space structures technologies applicable to a variety of future space missions. This report discusses these new technologies and provides a review of the SAFE/DAE design, flight operations, and flight results.

The principal component of the SAFE/DAE was a large, lightweight solar array wing designed for retraction as well as deployment operations in space. Both operations were accomplished by means of a fold/unfold method of solar cell panel deployment. Compared with the Skylab solar arrays (launched in 1973), that were similar in size, the SAFE solar array had the following unique features:

a) Approximately 1/8 the weight — Enables more payload to be carried per shuttle launch.

b) Retractable as well as deployable — Facilitates repair or replacement of the solar array in orbit.

c) Deployment/retraction to an intermediate position — Exposes only the amount of solar array needed to the space radiation environment, thereby reducing degradation and providing for increased lifetime; accommodates mission operations with higher spacecraft accelerations.

d) Restowage to survive docking and landing loads as well as launch loads — Facilitates on-orbit docking and return to Earth for testing and refurbishment.

The lightweight characteristics of this solar array technology led to the need for experimental testing in space. Since elaborate test fixtures are required in Earth's gravity to support the wing in any configuration, except fully retracted, deployment/retraction capabilities could fully be proven only by testing in space. Similarly, the

dynamic behavior of the deployed wing in space could not be determined with confidence through ground evaluations. For these reasons and because future NASA missions could benefit from this technology, the Office of Aeronautics and Space Technology (OAST) made the decision in 1977 to test a full scale wing as an experiment aboard the Shuttle.

The objectives of SAFE/DAE were as follows:

a) To demonstrate the readiness of large area, lightweight, photovoltaic array technology.

b) To demonstrate the capability to deploy and retract such arrays in the space environment.

c) To measure the electrical and thermal performance of advanced solar cell modules for comparison with predictions.

d) To measure the deployed wing dynamics for comparison with analytical model predictions.

e) To demonstrate advanced methods for data acquisition, reduction, and analysis of the dynamics of large space structures.

The STS-41D mission accomplished these objectives when it provided for 18 hr of testing and test data. After the flight, the SAFE hardware was returned to Lockheed Missiles and Space Company (LMSC) for inspection and tests to determine the effects of space operations. The results of the Marshall Space Flight Center (MSFC) analyses and the LMSC inspection and tests are reported herein.

II. SOLAR ARRAY FLIGHT EXPERIMENT (SAFE) DESCRIPTION

A. SAFE Wing

The SAFE wing design was developed to achieve a specific performance of at least 30 W/lb (66 W/kg). Weight reductions were achieved by using thin polymer films and composite materials throughout the design. However, in order to reduce program costs, these materials were used in wing hardware only in those elements where technology readiness for fabrication, handling and performance needed to be established. A weight summary for the SAFE is provided in Table 1. The "as-built" wing design is given in the discussion that follows.

The SAFE wing (Fig. 1) is a flat-fold flexible substrate solar array, sized to output more than 12.5 kW at the base of the wing at 55°C normal to the Sun in near-Earth space. The array blanket consists of 84 panels, 0.37 m × 4.0 m (14.5 in. × 13.1 ft) in size, that are mechanically hinged together to allow easy replacement of panels. Only two of the 84 panels have active solar cells. The third panel from the outboard end of the blanket contains two active solar cell modules (Fig. 2). One module employs 8-mil thick 2 cm × 4 cm silicon solar cells with 6 mil covers. The 704 cells in this module are electrically connected, 4 in parallel × 176 in series. The other module is made with 150 each, 8-mil thick 5.9 cm × 5.9 cm silicon solar cells in series. For cost reasons, there was not an attempt to maximize packing factor (cell area ÷ panel area) on these modules. All the cells on this panel have wraparound contacts and are welded to a printed circuit copper interconnect system that is encapsulated between two each 1-mil thick Kapton sheets with high temperature polyester adhesive. A third module, which is located on the first panel from the outbooard end, employes 2-mil thick, 2 cm × 2 cm silicon cells with 3-mil covers. This module contains

80 cells connected four in parallel by 20 in series. The interconnect system is welded to contacts located on the top and bottom sides of these cells. A 2-mil thick Kapton sheet serves as the substrate for these cells. Additional details are given in Table 2. The remaining 82 panels in the blanket use cell size glass mass simulators, cell size aluminum mass simulators, and 7.5 cm × 17.5 cm aluminum mass simulators. The simulators are bonded to 2-mil thick Kapton panels.

TABLE 1. SAFE WEIGHT SUMMARY

COMPONENTS	WEIGHT (LB)
EXPERIMENT TOTAL	940.0
SUPPORT STRUCTURE & SEPARATION SYSTEM	270.0
SEPARABLE WING ASSEMBLY	670.0
BLANKET	303.0
PANELS	280.5
HARNESS	18.5
TENSION BARS	4.0
CONTAINER	90.5
BASE HARDWARE	43.5
TENSION SYSTEM	18.5
LATCH SYSTEM	16.0
SUPPORT STRUTS	9.0
COVER	27.0
TIP HARDWARE	32.0
LATCH SYSTEM	22.0
TIP FITTING	10.0
MAST	122.0
BOOM	45.0
CANISTER	49.0
DRIVE	25.0
LOCK	3.0
JETTISON CAPABILITY	34.0
GRAPPLE	21.0
GRAPPLE FITTING	7.0
REAR SUPPORT	6.0
WIRES & CONNECTORS	7.0
MISC. FASTENERS & ADHESIVES	11.0

An aluminum flat-conductor cable harness assembly, bonded with an adhesive on each edge of the blanket, carries the module power as well as instrumentation signals to the base of the array. Blanket panels did not employ on-array padding for cell protection since development tests and analyses did not determine it to be necessary. The panels have local stiffening of graphite-epoxy ribs on the active modules to aid the zero-gravity foldup of the blanket. Aluminum stiffening is used on the remainder of the experiment blanket to reduce costs.

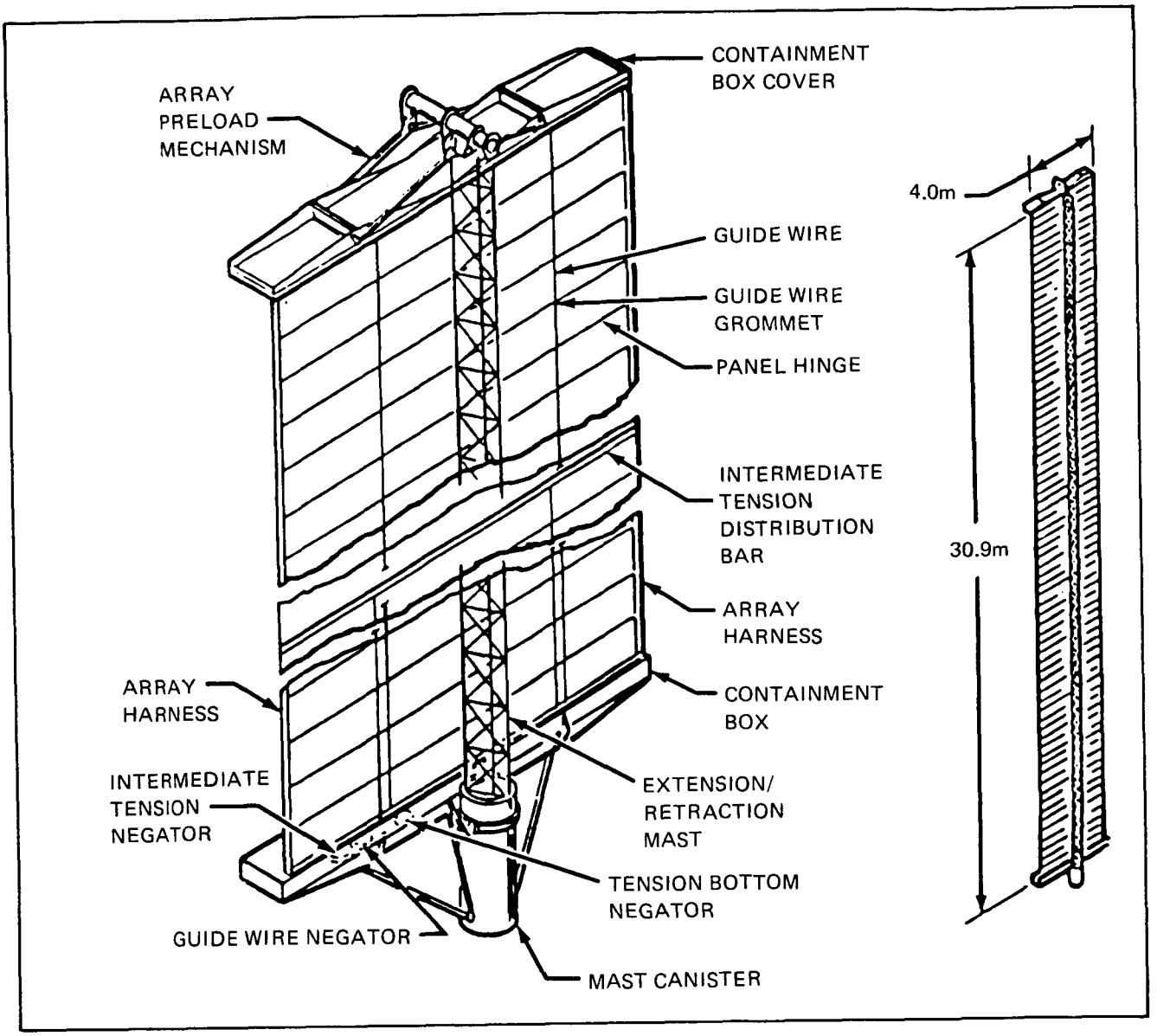

Figure 1. SAFE wing.

The array containment box is an aluminum structure with an aluminum honeycomb floor. The box cover employs a graphite-epoxy structure with aluminum honeycomb to demonstrate methods for reducing weight. The mast (Fig. 3) is a coilable longeron lattice structure using fiberglass-epoxy longerons and battens with steel diagonal cables. The longerons in the outboard 1½ bays of the mast, which are not required to coil even when fully retracted, are made of aluminum to carry the forces required to preload the blanket in its containment box during retraction and storage. Microswitches, located in the mast canister, work in conjunction with actuators on the mast to select 70 percent or 100 percent wing deployment positions. The mast, built by AEC-Able Engineering Co., Inc., is driven by redundant brushless DC motors acting through a differential. The mast motor drive assembly is built by Aeroflex Laboratories, Inc.

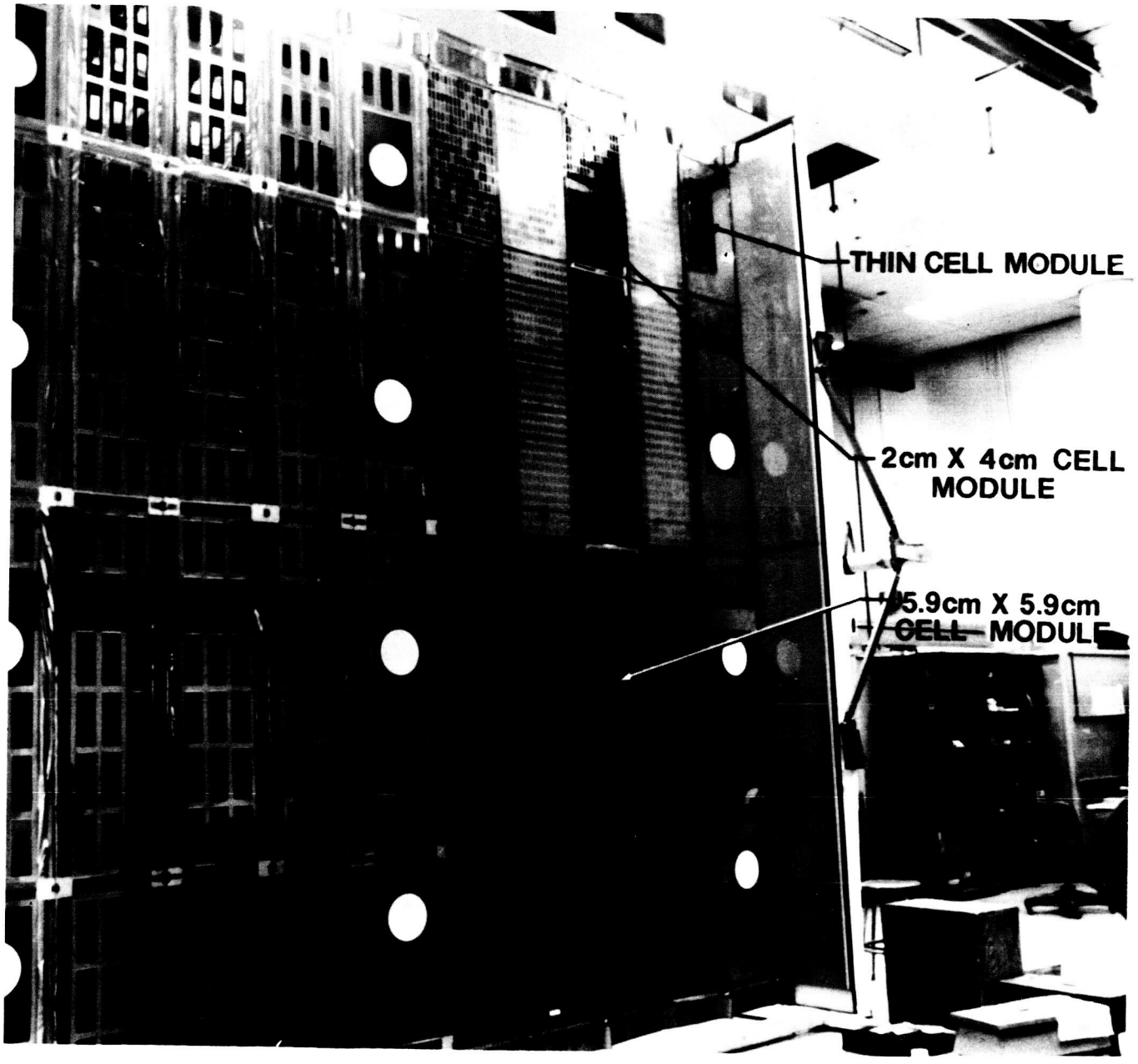

Figure 2. Active solar cell modules.

Three (3) advanced-type solar cell modules were located on panels at the outboard end of the SAFE wing. Panels composing the rest of the wing employed glass and aluminum solar cell simulators. The white circles are targets for the photogrammetry experiment.

TABLE 2. SOLAR CELL AND ELECTRICAL MODULE CHARACTERISTICS

ELECTRICAL MODULE WITH 5.9 cm x 5.9 cm SOLAR CELLS	
CELL TYPE	Si, 2 ohm - cm, BSR, WRAPAROUND CONTACT
CELL SIZE	5.9 cm x 5.9 cm x 200 MICRON
NUMBER OF CELLS IN MODULE	150 (1 PARALLEL x 150 SERIES)
CELL INTERCONNECT	COPPER
COVER SLIDE	150 MICRON MICRO SHEET
COVER SLIDE ADHESIVE	50 MICRON DC 93-500
FRONT SURFACE COATING	UV AND ANTI–REFLECTIVE
ELECTRICAL MODULE WITH 2 cm x 4 cm SOLAR CELLS	
CELL TYPE	Si, 2 ohm - cm, BSR, WRAPAROUND CONTACT
CELL SIZE	2 cm x 4 cm x 200 MICRON
NUMBER OF CELLS IN MODULE	704 (4 PARALLEL x 176 SERIES)
CELL INTERCONNECT	COPPER
COVER SLIDE	150 MICRON FUSED SILICA
COVER SLIDE ADHESIVE	50 MICRON DC 93-500
FRONT SURFACE COATING	UV AND ANTI–REFLECTIVE
ELECTRICAL MODULE WITH 2 cm x 2 cm THIN SOLAR CELLS	
CELL TYPE	Si, 2 ohm - cm, BSF, TOP/BOTTOM CONTACT
CELL SIZE	2 cm x 2 cm x 50 MICRON
NUMBER OF CELLS IN MODULE	80 (4 PARALLEL x 20 SERIES)
CELL INTERCONNECT	SILVER PLATED INVAR
COVER SLIDE	75 MICRON MICRO SHEET
COVER SLIDE ADHESIVE	DC 93-500
FRONT SURFACE COATING	NONE

B. SAFE Wing Support Structure

A wing support structure which provides mechanical interface with the Shuttle integration support structure is shown as a part of the Experiment Package in Figure 4. It also serves as a mount for the data acquisition system (DAS) box and the SAFE tape recorder, and it has provisions for separating the wing with the remote manipulator system (RMS) arm, should the wing fail to retract to a safe reentry configuration. Figure 5 is a view of the OAST payload, comprised of the SAFE/DAE and the Solar Cell Calibration Facility (SCCF), in the shuttle cargo bay aboard STS-41D. The SAFE wing is located approximately 20 ft from the crew compartment.

C. SAFE Data Acquisition System (DAS)

The DAS includes the experiment instrumentation, the signal processing to convert analog data to 8 bit PCM data, and a tape recorder to record these data during on-orbit experiment operations. The experiment contol, power distribution, and pyrotechnic initiator circuits (PICs) are a part of the DAS. The PICs facilitate wing release for separation should it become necessary.

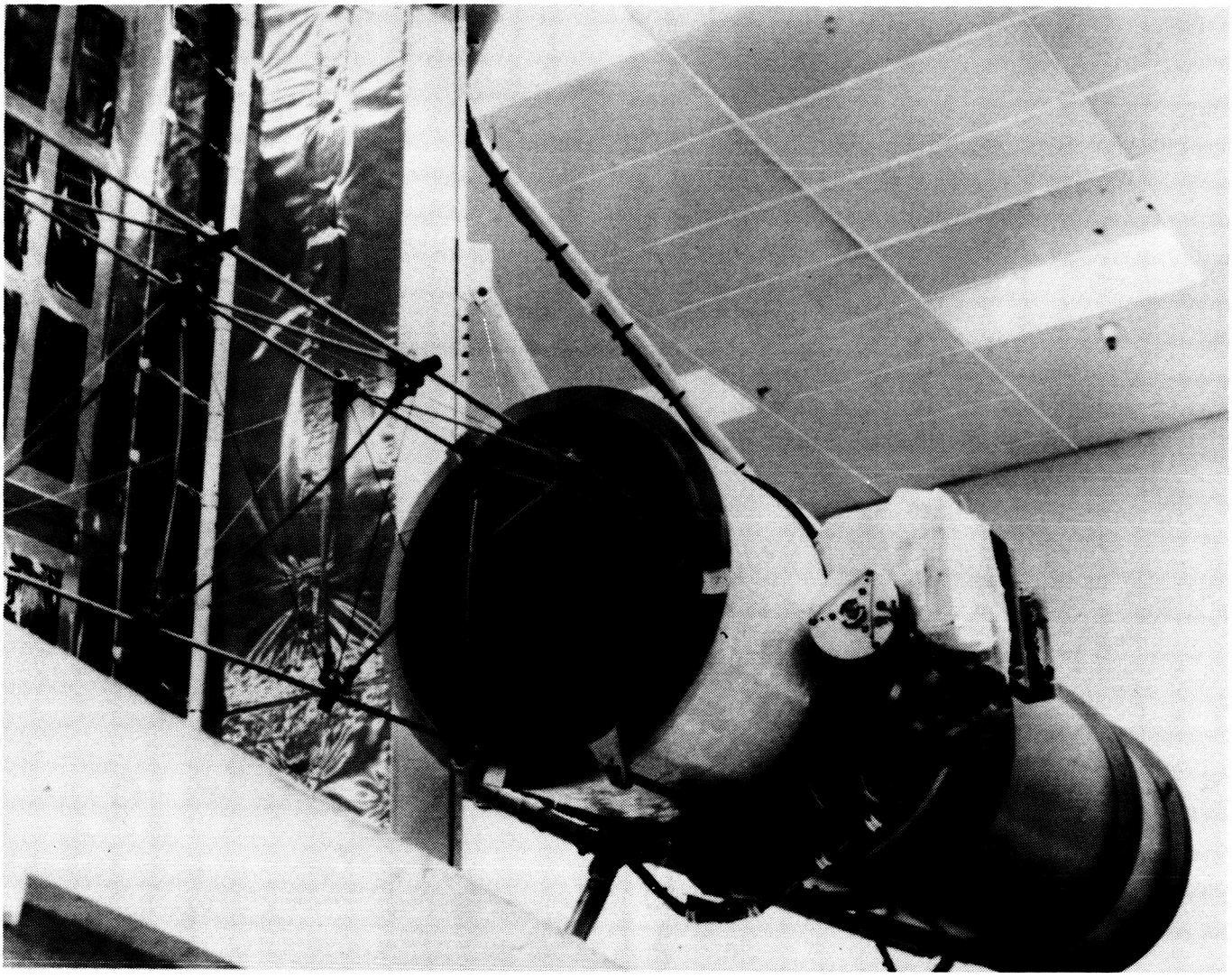

Figure 3. SAFE extension mast and canister.

The main elements of the SAFE extension mast are 3 fiberglass-epoxy longerons approximately 110 ft long that were coiled into or uncoiled from the mast canister during retraction/extension operations. The canister is approximately 15 in. in diameter by 5 ft in length. Redundant, brushless DC motors operating through a differential gear box provide the driving force for mast operations.

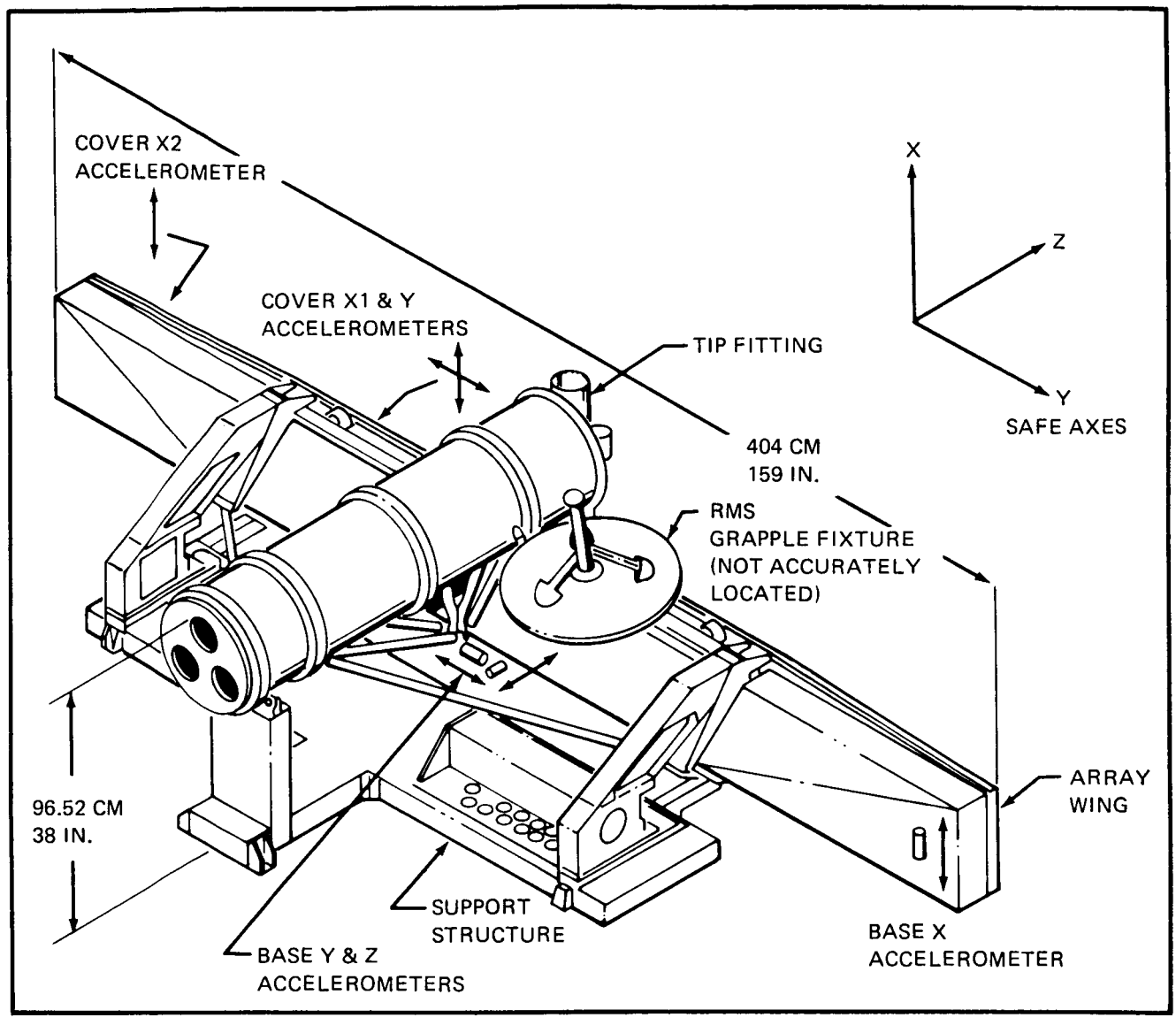

Figure 4. Experiment package.

The experiment science instrumentation consists of five thermistors, six low-"g" accelerometers, and solar cell module voltage and current monitors. One thermistor per module measures the temperature of the back surface of the three active solar cell modules. The other two thermistors are used to measure the temperatures of the cells on the 2 cm × 4 cm and 5.9 cm × 5.9 cm modules. In this way, temperature gradients through the substrate are established. Figure 4 shows the location of the accelerometers. Three are located at the base of the wing for measuring X, Y, and Z accelerations. Accelerometers for measuring X and Y motions of the end of the wing are located on the array cover near the mast tip. Torsional acceleration is detected by an accelerometer oriented in the X direction near the end of the cover. Voltage and current (IV) data are obtained for each of the three active solar cell modules by switching them through eight resistive load points. Internal voltages and mast motor current are also measured. The Orbiter supplemented the DAS by providing closed circuit TV (CCTV) coverage of test operations and onboard display and downlinking of selected SAFE data.

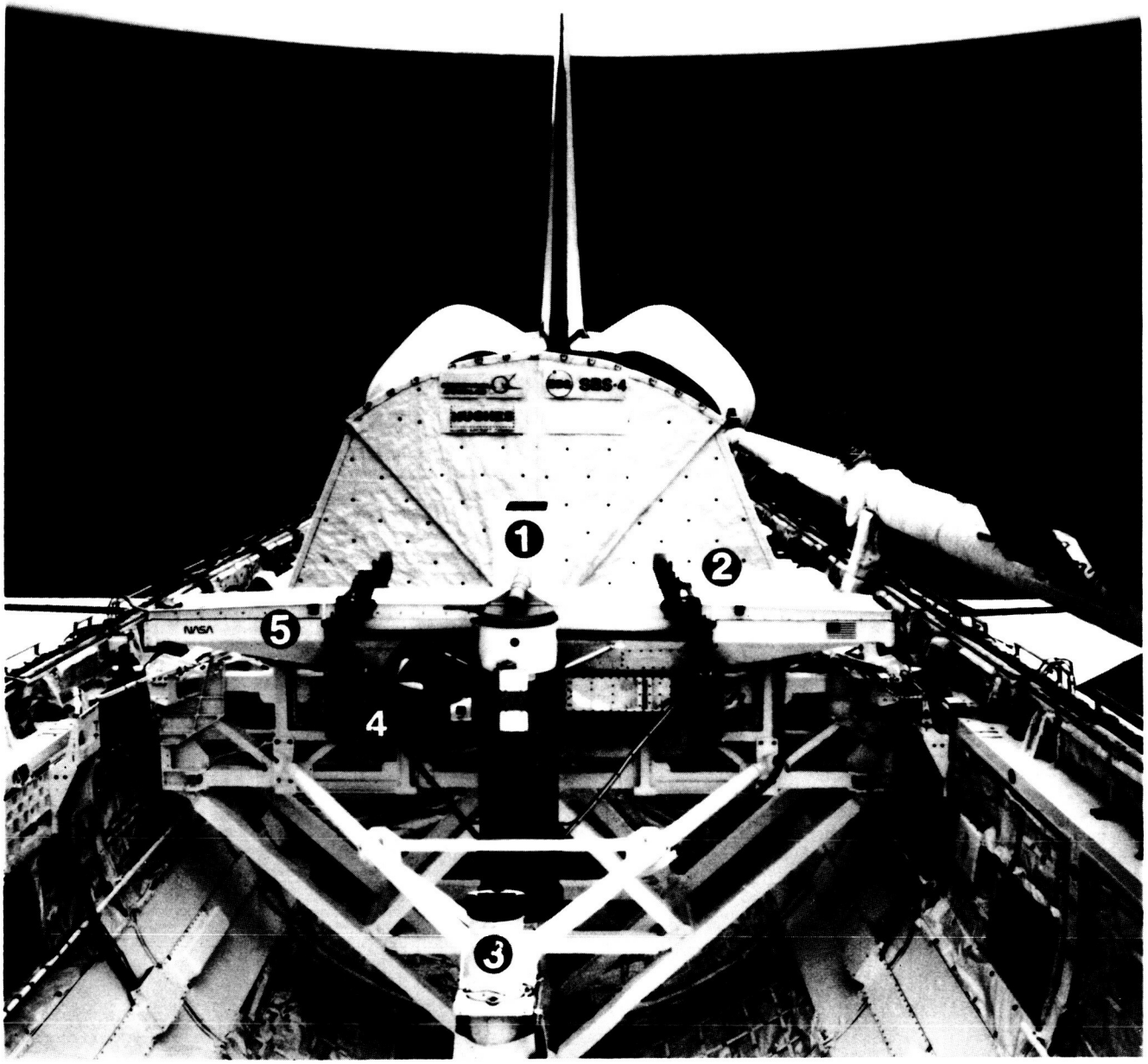

(1) SCCF (2) ELCTRONICS PACKAGE, DAE (3) RETROREFLECTOR FIELD TRACKER DAE (4) RMS GRAPPLE FIXTURE (5) SAFE WING

Figure 5. OAST-1 in orbit.

OAST-1 was taken into orbit aboard the Shuttle Discovery (Mission STS-41D) on August 30, 1984. The picture was taken by a crew member through the Aft-Flight Deck (AFD) window. OAST-1 was located approximately 20 ft from the AFD bulkhead. Three (3) satellites were successfully deployed before OAST-1 test operations were conducted.

The experiment control circuitry interfaces with the Orbiter aft flight deck (AFD) standard switch panel. Switch commands on the panel operate relays in the DAS box to control 28 VDC power to the DAS electronics, component heaters, tape recorder, mast motors, and the PICs. Displays on the switch panel and a TV monitor near the panel provide the experiment operator with the status of the experiment hardware. The PICs are separate and redundant and can utilize both primary and auxiliary orbiter power. Electrical interfaces with the experiment are at connectors on the DAS box.

The experiment tape recorder is a Lockheed Electronics Company Mark V, Type 4200. It employs 450 ft of high temperature tape and will record for 6 hr.

A more detailed description of the SAFE wing, wing support structure, and data acquisition system are given in Reference 1.

D. Photogrammetry

As part of the SAFE, the Shuttle television cameras were used to gather photogrammetric data on the dynamic motions of the structure. Sixty-three white circles, approximately 16.5 cm (6.5 in.) in diameter, are located at regular intervals on the front of the blanket. Another 63 circles are located at the same positions on the back of the blanket. The Shuttle CCTV system monitored and recorded the relative motion of these targets in response to controlled excitations of the deployed structure. Cameras located near the four corners of the cargo bay were used, with diagonally opposite camera pairs focused on the same position of the blanket to obtain stereoscopic images for photogrammetric analysis. These data were analyzed after the flight to determine the wing dynamics and to verify photogrammetric utilization of television cameras and recorders as a remote sensing system.

The Langley Research Center report [2] provides a detailed description of the photogrammetry hardware, analysis methodology, and flight results.

III. DYNAMIC AUGMENTATION EXPERIMENT DESCRIPTION

The DAE is an adaptation of a multifield star tracker that was designed to determine the dynamic characteristics of the SAFE wing during special SAFE wing dynamics tests. A retroreflector field tracker (RFT) (Fig. 5), positioned near the base of the wing, uses laser diodes to illuminate 23 targets on the wing. Ball Aerospace Systems Division contracted with MSFC to develop and provide the RFT. The targets are made of retroreflective tape placed on small aluminum supports. Sixteen (16) of these targets are located on the back of the blanket (Fig. 6). As the blanket flattens during deployment, these targets stand off the blanket surface to provide the best reflective angle. Four targets are located on the wing mast, two on the containment box cover and one on the tip fitting of the mast.

The targets return the emitted energy to a receiver in the RFT that focuses the reflector images on a solid state sensor. The sensor samples the image position in the focal plane, and a microprocessor computes the position of the targets. A second microprocessor computes the dynamic array displacement from the line of sight and provides a 12 bit digital output, through a PCM multiplexer, to a digital tape recorder. The data are recorded and returned for ground processing. The PCM multiplexer, tape recorder, and a Power Conditioning and Distribution Assembly are located in the DAE Electronics Package (Fig. 5).

Figure 6. DAE retroreflector targets.

Twenty-three (23) retroreflector targets for the DAE were located on the SAFE wing. A tape made by 3-M Company served as the retroreflective element. The picture was taken, using a flash camera and a darkened room, with the SAFE wing in its horizontal test fixture at LMSC.

IV. FLIGHT OPERATIONS

A. Overview

The flight test timeline allotted approximately 23½ hr for SAFE/DAE testing over a three-day period. Included were extension/retraction testing, dynamic testing, and solar cell module performance testing. As described below, test operations proceeded without difficulty, facilitating testing in addition to that timelined to be conducted.

B. Extension/Retraction Testing

Four extension/retraction cycles had been identified by the investigators as being required to demonstrate the capability of the wing to extend and retract and gather supporting data. Orbiter TV cameras, located on the cargo bay bulkheads, and the Remote Manipulator System (RMS) arm and video tape recorders (VTRs), located in the aft flight deck, were used to gather data. Postflight studies of the unfolding/refolding actions of the blanket and mast operational characteristics were performed to determine the capabilities of this technology and identify potential improvements.

Prior to flight of the experiment, an analytical model of the deployed array was developed and used in response analyses to predict the solar array dynamic response to a specific Orbiter Vernier Reaction Control System (VRCS) firing sequence. The parameter values used in the analytical model were determined or verified by on-ground testing to the extent possible or practical. Stiffness of the extension mast and mast canister interface compliance were verified by both static and dynamic testing. The tension in guidewires and blanket tension mechanisms were determined by functional tests, but only in ambient temperature. Shear stiffness of the blanket was verified by a coupon test. Weight distribution was determined by weighing individual parts, major assemblies, and the total system.

Since the adequacy of the analytical dynamic model could not be determined until dynamic tests had been conducted in space, it could not be determined with sufficient confidence prior to flight that the orbiter could be maneuvered between attitudes, with the wing extended, without exceeding the mast longeron bending moment capability. For this reason, the flight plan called for the wing to be retracted whenever the orbiter performed attitude maneuvers. As a result, 10 extension/retraction cycles were identified in the flight test timeline. However, real-time evaluation of the first dynamic test data (down-linked accelerometer data) proved the adequacy of the dynamic model to predict wing behavior (acceleration, tip deflection, etc.), confirming preflight predictions that mast longeron load capability would not be exceeded with the required orbiter maneuvers. The number of extension/retraction cycles needed to accomplish all objectives were therefore reduced to four (Table 3).

C. Dynamic Testing

Eight dynamic tests were specified in the flight test timeline to acquire data necessary to accomplish the wing dynamics objective. Four of these tests were scheduled to be conducted during the daylight periods at approximately orbital noon, with the remainder to be conducted after midnight during dark periods. Accelerometers and photogrammetry were used to gather dynamics data during daylight, while accelerometers and the DAE were used during periods of darkness.

TABLE 3. FLIGHT TEST EVENTS

EVENT	OPERATION	GMT	MET
1	UNLOCK MAST	245:16:41:34	2:03:59:43
2	1ST EXTENSION	245:17:34:43	2:04:52:52
3	1ST RETRACTION	245:17:59:39	2:05:17:48
4	2ND EXTENSION	245:19:04:52	2:06:23:01
5	SAE DYN 70% O/P	245:19:25:27	2:06:43:36
6	DAE DYN 70% O/P	245:20:13:27	2:07:31:36
7	2ND RETRACTION	245:20:48:45	2:08:06:54
8	3RD EXTENSION	246:10:40:07	2:21:58:16
9	SOLAR CELL MODULE TESTS	246:11:27:54	2:22:46:03
10	SAE DYN 70% M/M	246:13:29:27	3:00:47:36
11	DAE DYN 70% M/M	246:14:21:55	3:01:40:04
12	SAE DYN 70% O/P	246:15:00:26	3:02:18:35
13	DAE DYN 70% I/P	246:15:52:32	3:03:10:41
14	SAE DYN 70% M/M	246:16:30:22	3:03:48:31
15	DAE DYN 70% M/M	246:17:23:04	3:04:41:13
16	1ST EXTENSION TO 100%	246:17:53:12	3:05:11:21
17	SAE DYN 100% O/P	246:18:06:29	3:05:24:38
18	1ST RETRACT 100% TO 70%	246:18:18:42	3:05:36:51
19	2ND EXTENSION TO 100%	246:19:16:58	3:06:35:07
20	SAE DYN 100% M/M	246:19:31:29	3:06:49:38
21	2ND RETRACT 100% TO 70%	246:19:47:19	3:07:05:28
22	RETRACT 70% TO 0%	246:19:54:28	3:07:12:37
23	4TH EXTENSION	247:14:37:15	4:01:55:24
24	SOLAR CELL MODULE TESTS	247:14:49:58	4:02:08:07
25	SOLAR CELL MODULE TESTS	247:15:39:15	4:02:57:24
26	DAE DYN 70% M/M	247:16:02:11	4:03:20:20
27	SAE DYN 70% M/M	247:16:37:24	4:03:55:33
28	DAE DYN 70% I/P	247:17:32:39	4:04:50:48
29	SAE DYN 70% I/P	247:18:07:22	4:05:25:31
30	LAST RETRACTION	247:18:19:19	4:05:37:28
31	LOCK MAST	247:19:50:09	4:07:08:18

The smoothness of flight operations allowed testing in addition to that specified in the flight timeline to be conducted. Scientific and "housekeeping" data were obtained for all the test events. The SAFE data system had an internal elapsed time clock that was used to correlate recorded test data with the mission elapsed time (MET).

Predetermined firing sequences of the VRCS provided accelerations to excite the wing extended to the 70 or 100 percent deployed position in the out-of-plane (orbiter pitch), in-plane (orbiter roll), and multimodal (combination of pitch and roll) modes. These firings were planned to provide adequate displacement of the array for good data acquisition, without exceeding the structural capability of the array. Since the first dynamics test proved that the orbiter could maneuver between attitudes without retracting the wing, time was conserved, enabling 14 dynamics tests to be conducted during the mission. As a result of array response being less than predicted during the first two test days, excitation energy was increased to 1.5 its previous level for the third day's tests. Test cases shown repeated in Table 2 were performed to verify repeatability and to obtain redundant data.

D. Solar Cell Module Performance Testing

Two solar cell module performance tests were conducted. In the first, the wing was extended in a solar inertial attitude before sunset on orbit 47. The wing remained in this attitude until orbit 49. Performance data were recorded from 5 min before sunrise until 5 min after sunset, during orbit 48.

In the second performance test, extension of the wing was begun in a solar inertial attitude about sunrise on orbit 66. Module performance data were recorded during the extension and for 15 min thereafter. The orbiter was then maneuvered into a gravity gradient attitude for additional SAFE dynamics testing.

V. EXPERIMENT ANALYSES AND DATA REDUCTION

A. Array Extension/Retraction Testing

Two methods have been used to evaluate the performance of SAFE mechanical operations: review of flight data and postflight observations of the hardware. Flight data consist primarily of video tapes and still photos. Some information was derived from the DAE and accelerometer and motor current data. Postflight evaluation consisted of operational testing and a visual inspection of all aspects of the array structure. The array was fully deployed in the horizontal fixture at LMSC in January 1985 for this inspection.

During the first on-orbit extension test, which was performed in a tail-to-Earth gravity gradient attitude, a grouping of the unfolding panels at the outboard end of the wing was observed. Nominally, the panels are expected to unfold in a uniform accordion manner. As the extension continued, panels were released from the grouping, imparting a brief wave motion into the blanket. These effects did not significantly affect other characteristics of the extension operations. The time required to extend to the 70 percent position was nominal, taking 9 min and 18 sec. Mast motor currents were approximately the same as had been observed in ground testing. Later extensions did not exhibit the panel grouping effect. In Figure 7, the expected uniform accordian unfolding configuration can be observed. The grouping is believed to have resulted from trace amounts of adhesives that were inadvertently left on the blanket surface during fabrication and assembly of the blanket and storage of the blanket in its compressed state for several months before the flight. Panel-to-panel sticking had been observed in preflight ground testing and attempts were made to remove the adhesives when it was encountered. However, it was used extensively in the blanket design, and because of its color, was difficult to locate and remove completely. Postflight inspections gave no definite reasons for the grouping. It is possible that vacuum and the elevated temperatures experienced in space had a cleaning effect upon the blanket.

At times during the flight, a curling of the blanket with the edges toward the mast was observed (Fig. 8). It was always evident in DAE data taken about midnight with the orbiter in a gravity gradient attitude. In this attitude, the active side of the solar array blanket was facing the Earth. Having been in Earth's shadow for several minutes, blanket temperatures were low: solar cell module temperatures ranged from –60°C to –80°C.

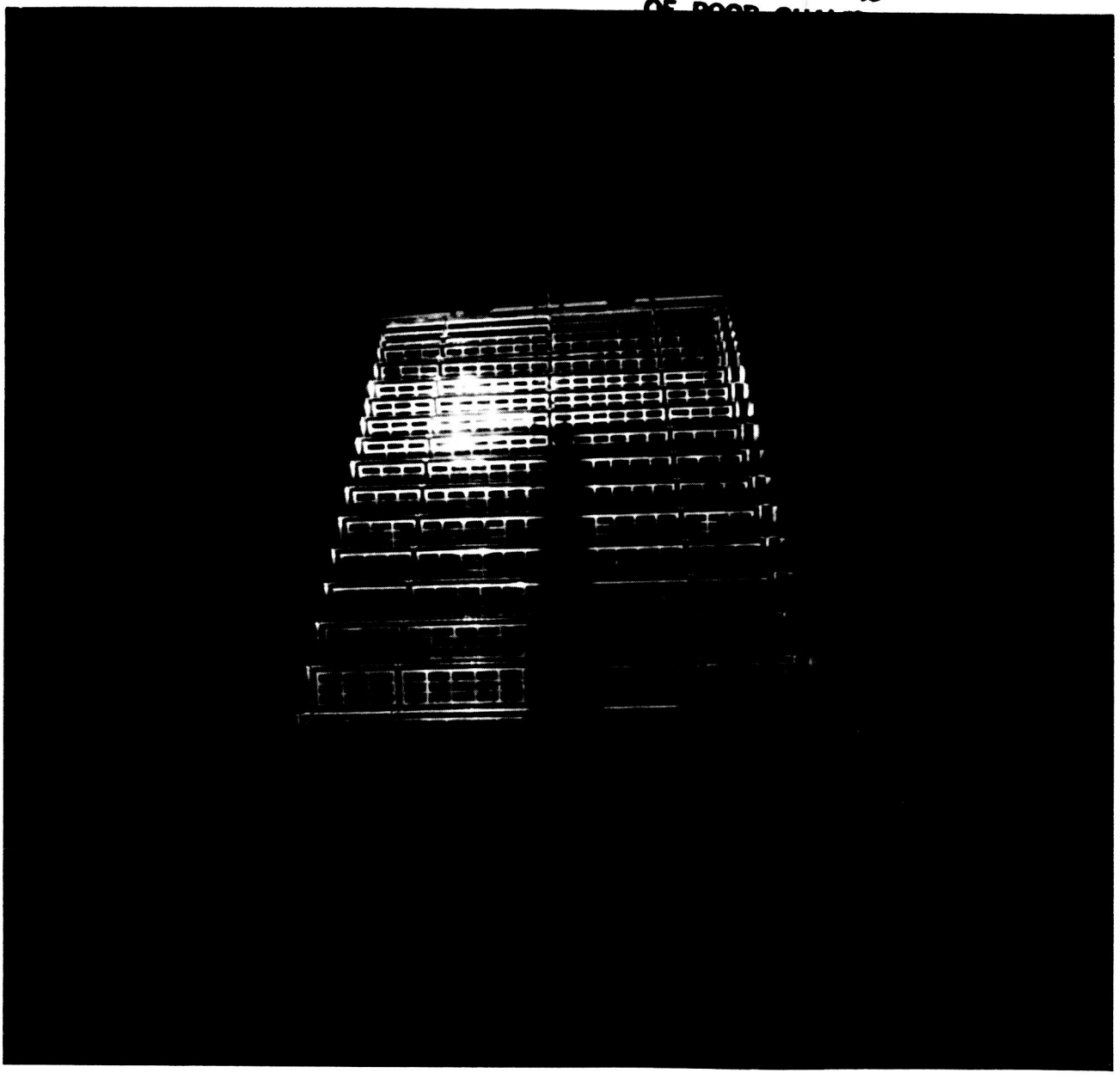

Figure 7. SAFE wing deployment.

After the first extension event, extension/retraction operations exhibited uniform accordian-like unfolding/refolding characteristics. The picture was taken about sunrise through a window of the Aft Flight Deck with the Orbiter in a solar inertial attitude. A shadow of the Orbiter vertical tail member can be seen on the blanket.

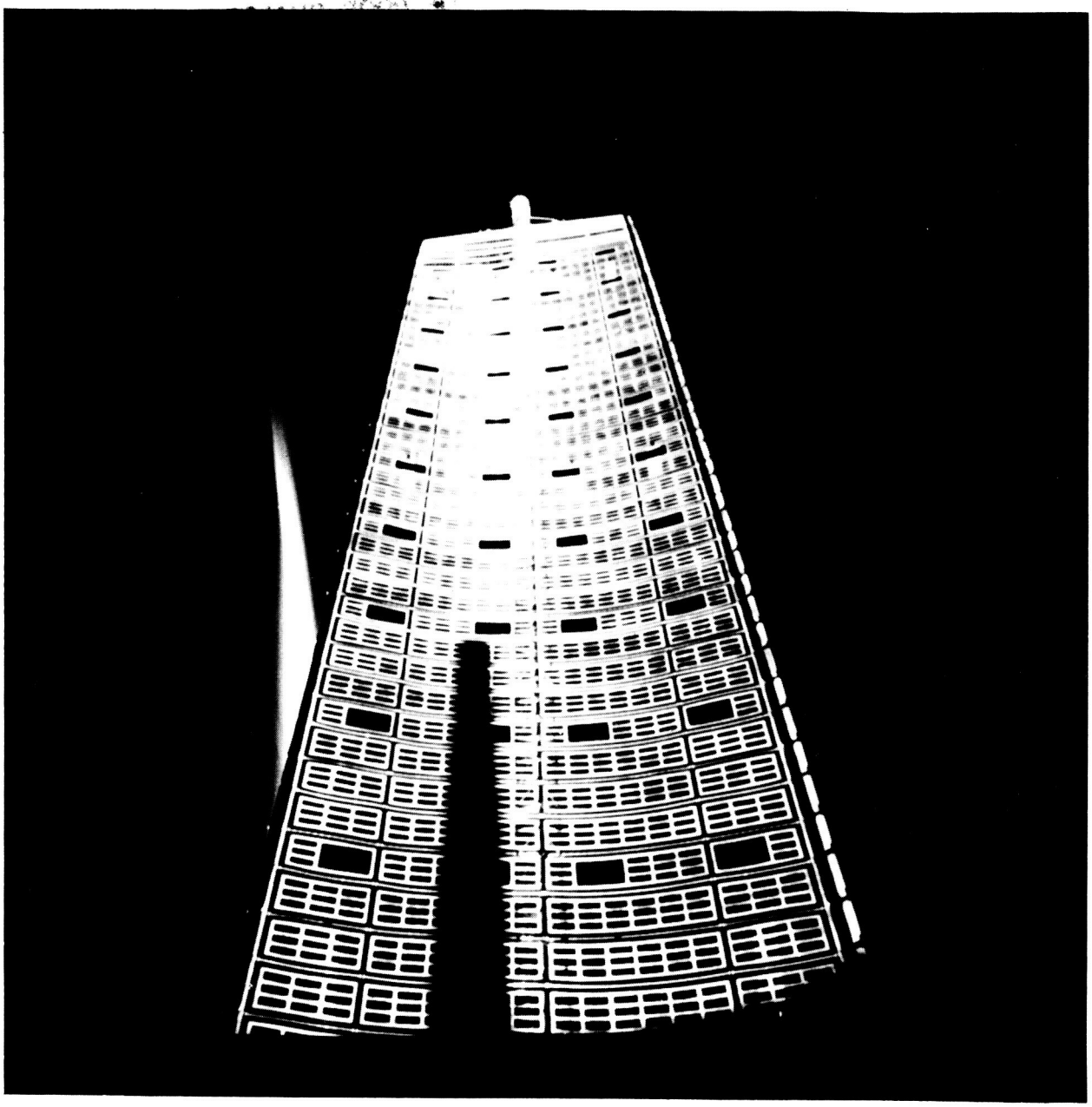

Figure 8. Curled blanket.

Improper allowances for temperature induced expansion and retraction of the SAFE blanket materials sometimes resulted in a curvature of the blanket. This picture was taken about sunset from the Aft Flight Deck with the Orbiter in a solar inertial attitude. A shadow of the Orbiter vertical tail member can be seen on the blanket.

Upon entering sunlight in this attitude, the blanket was observed to flatten (Fig. 9). An STS-41D crew member reported that the blanket became flat in about 10 min. Stabilized temperatures of the solar cell modules during this period were in the neighborhood of 50°C to 60°C. All observations of the blanket during the solar inertial attitude, with the active side of the blanket toward the Sun, showed the blanket to be curled. Temperatures of the solar cell modules over one orbit in this attitude ranged from approximately –80°C to approximately +75°C.

Review of the DAE data shows a consistency in curling from one test event to another in the same blanket cross sectional view. This consistency does not hold from one cross sectional view to another during the same test event. Maximum depth of the curl, as determined from the DAE views, is 44 cm (17.7 in.). These inconsistencies suggest that the curling of the blanket is caused by some thermal expansion condition or combination of conditions. No thermistors were in place that would measure thermal gradients in the blanket at locations other than on the active solar cell modules. Postflight testing at LMSC [1] has indicated that the panel curvature was caused by an inadequate thermal expansion gap between aluminum frames and Kapton sleeves, which serve as a stiffening mechanism in the panels that comprise the blanket. The major factors contributing to the inadequacy of the gap are Kapton shrinkage factors (when exposed to vacuum), not considered in the design, and temperature differences between the aluminum frames and the Kapton. Preflight thermal distortion analyses assumed the aluminum frames operated at the same temperature as the Kapton. Elevated frame temperature relative to the Kapton, when combined with smaller gap due to Kapton shrinkage, caused the panels to curve in the direction observed in flight.

Observations of visual recorded data (film and TV) indicate a built-in twist in the mast. This twist has been determined to be 7.8 deg from photogrammetry and DAE data. The twist was known to exist before the flight but was not corrected since it did not cause blanket alignment to fall outside specifications or detract from the wing extension/retraction capability.

Other interesting phenomena that occurred during extensions and retractions of the wing were oscillatory motions of the mast and the blanket. During extensions to and retractions from the 70 percent deployed position, a mast oscillation developed and decayed. Accelerometers indicated its peak to be approximately 11 ft from the 70 percent deployed position. During extensions from the 70 percent position to the 100 percent deployed position, accelerometers indicated that motion peaked about 4 ft from the 100 percent deployed position. During retraction from the 100 percent to the 70 percent deployed position, mast oscillatory motion was again observed, but saturation of accelerometer data circuitry prevented determination of the mast length at which maximum motion occurred. These mast motions did not detrimentally affect the unfolding/folding characteristics of the blanket.

During all retractions, when the length of the blanket was reduced to approximately 14 ft, visually detectable blanket longitudinal oscillatory motion began, grew in amplitude for approximately 20 sec, and then decayed at about the same rate. Calculations, based on video tape coverage, indicate that the frequency was about 0.75 Hz, which is the rate of mast nut rotations. The amplitude of the motion reached a level at which it appeared that active solar cells or the glass solar cell simulators could be broken. However, postflight examination of cells and simulators did not reveal any additional breakage (cracks) over that which existed before flight. The extension/retraction dynamics of the wing has been studied at MSFC and is reported in References 3 and 4.

The blanket container, locking system, release system, and tension wire system appear to have functioned properly during the flight. Close inspection of the locking levers, which provide preload to the blanket, revealed some scratches at the entrance to the cam system. These have been attributed to wobble in the mast as it approached the near-closed position. A thorough postflight inspection of the mast revealed no significant structural damage. Small amounts of contamination and discolorations were observed on the outer most panels of the wing. Samples were taken in these areas, analyzed, and determined to be BRAYCO grease from inside the mast containing fine particles from the mast rollers and the inside surface of the rotating nut. In addition, the chemical analysis revealed the presence of a waxy substance in the contamination. The source of the wax was traced to the strands of stainless steel wires used in the diagonal cables of the mast. An inspection of the wing for atomic oxygen interaction effects did not reveal any change. It was concluded that the wing was not flown with its major surfaces perpendicular to the velocity vector sufficiently long for these effects to be detectable by ordinary visual inspection.

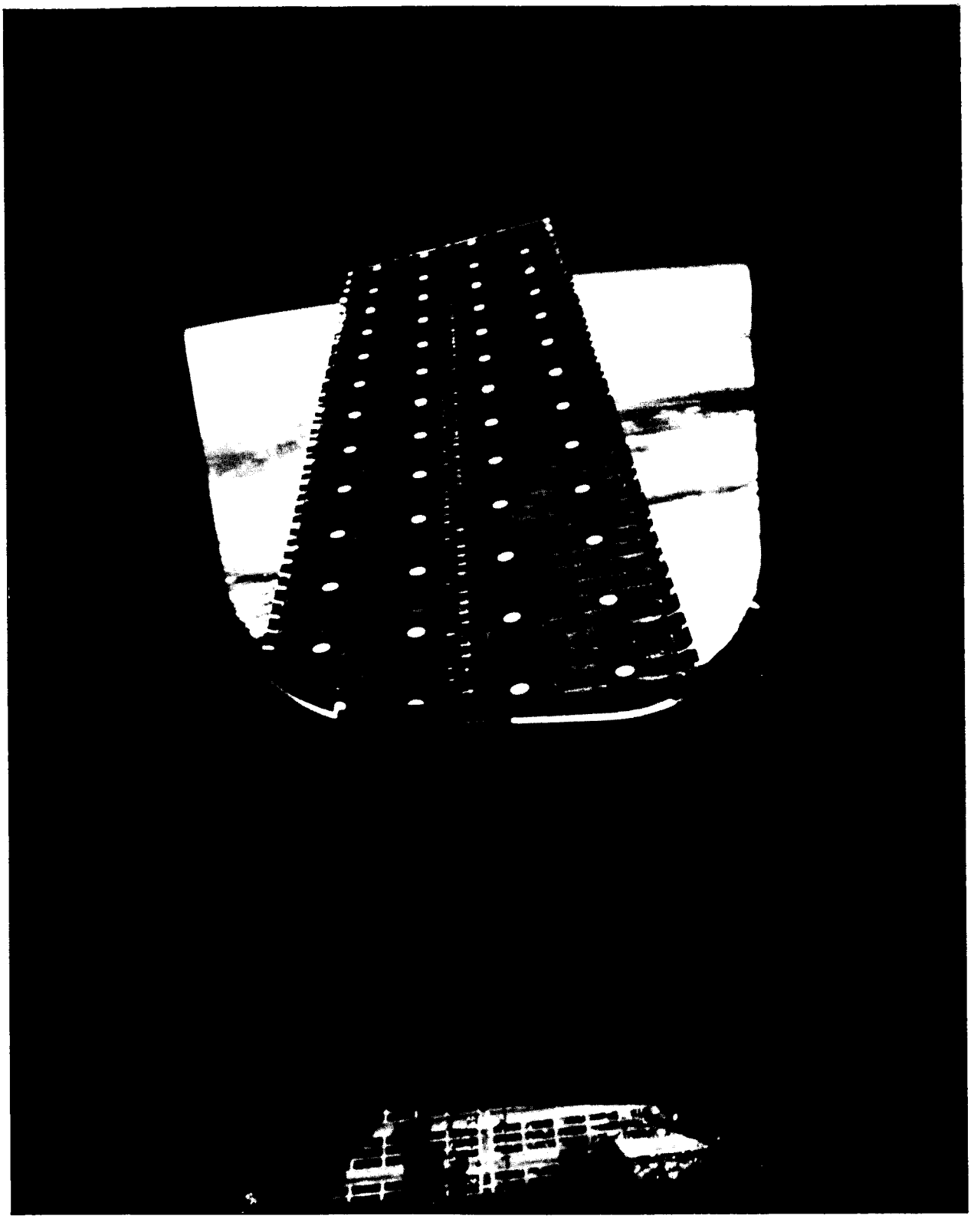

Figure 9. Flat blanket.

Additional details of flight extension/retraction operations and postflight testing, inspection, and analyses are reported in Reference 1.

B. Dynamics of the Deployed Array

1. Background. One of the original objectives of the flight experiment was to determine the on-orbit dynamic characteristics by test. This was to include determination of natural frequency, modal damping, and mode shape of the mast and blanket. Early in the development of the experiment, the decision was made to instrument the experiment with accelerometers at the base of the array and on the containment box cover. From this limited instrumentation, the natural frequency, response of the containment box cover, and the modal damping of the structure could be determined. It was not possible to obtain the mode shape. With the start of the Large Space Structures (LSS) Technology program, there was increased interest in performing dynamic testing of a large, very flexible structure in space. The solar array experiment was an excellent structure on which to implement such testing. In response to this opportunity, the Langley Research Center developed the photogrammetry technique for reducing the modal characteristics of the deployed array. Also, in response to this opportunity, the Marshall Space Flight Center developed the Dynamic Augmentation Experiment which is a different approach for accomplishing the same objective. Both of these experiments were designed to facilitate determination of dynamic mode shapes.

An additional source of dynamic data for the wing are photographs of the mast cover, taken from the crew cabin with a 35mm Nikon camera and 500mm lens.

The end result was that redundant methods of determining the dynamic characteristics of the deployed array were used. Results of the various methods will be shown and compared, where appropriate.

2. Preflight Testing. In order to develop an analytical preflight structural dynamic model of the deployed array, as much ground testing of the array was performed as could be considered practical. These tests are described as follows:

a. Static Load Tests. Static load tests of a 12-ft segment of the mast were performed. Later a static load test of the total length mast, installed in the canister, was performed with the mast in a horizontal position and supported by a water table. From these tests, the bending and torsional stiffness of the mast were determined, as well as the mast/canister interface compliance.

b. Modal Survey Tests. A modal survey test of the mast, with canister, was conducted with the mast in a horizontal position and supported along the mast length by long suspension wires. From this test, the bending stiffness and mast/canister interface compliance, determined by the static load test, were further verified (only small differences in the interface compliance were observed). Additionally, the modal damping of the mast was determined. Because of air resistance and complicated support required, the total system, with blanket attached, was not ground tested.

c. Functional Tests. Functional tests of the constant force mechanisms, used for keeping the blanket and guide wires in tension, were performed for each mechanism separately. Each mechanism had separate characteristics, and these differences were included in the analytical model.

d. Blanket Shear Stiffness Tests. A shear test of a section of blanket was performed to determine the shear stiffness to be included in the model of the blanket.

e. Weight Measurements. Components and assemblies were weighed, so that accurate mass characteristics were available for inclusion in the analytical model.

3. Preflight Analysis. A structural dynamic model was developed by LMSC for both 70 percent deployment and 100 percent deployment configurations. These analyses incorporated the results from the various structural tests. The Charles Stark Draper Laboratory performed a space shuttle on-orbit flight control system/solar array dynamic interaction study. The study was basically a response analysis of the solar array wing to the shuttle vernier reaction control system. Seventy-two response analysis cases were performed in an attempt to identify the worst loading case. Also, the response to the planned test excitations were performed. The most important purpose of these response analyses was to obtain confidence that the load-carrying capability of the mast would not be exceeded for any shuttle operation with the solar array extended. Consequently, to be conservative, a damping value of 0.5 percent of critical was used for all cases. The dynamic test of the mast alone had shown a damping of 1.5 percent of critical, and dynamic testing of a 9-ft section of similar mast had resulted in approximately 3.0 percent damping, so that the 0.5 percent value was known to be conservative. The second purpose of the response analysis was to predict the response for the planned test configuration. The results of these response analyses were verified by independent response analyses, performed by in-house personnel at MSFC and by support contractor personnel at JSC.

In summary, analyses showed the solar array wing to be capable of withstanding orbital maneuvers and station keeping with the array extended to the 70 percent extension configuration. The attitude control system was inhibited when the array was extended beyond 70 percent.

4. Operational Considerations. Fourteen on-orbit dynamic tests were performed. A description of these tests is given in Table 4. From the Table, it can be seen that photogrammetry data and DAE data were never taken simultaneously. This was necessary because of the television camera requiring light for operation and the retroreflector field tracker requiring darkness for operation. Accelerometer data were taken for all cases. The Nikon camera was used for two tests. Therefore, there was always at least two methods of taking data for any given test, allowing comparison of test results from different data sources.

There were observed anomalies that were not reflected in the preflight analysis that should be addressed before a discussion of test results. When the flight mast was originally manufactured, a twist in the mast was measured to be approximately 6 deg. By selectively replacing diagonal wires, the twist was reduced to less than 1 deg. Later, the outermost bays of the mast were damaged by overcycling that part of the mast. Because of the damage, all diagonals in the outer 16 ft of the mast were replaced. Additionally, eleven diagonals distributed throughout the remaining length of the mast were replaced. Due to cost and schedule considerations, the mast twist was not remeasured on the water table before flight. Postflight analysis, from DAE experiment data, showed the twist during flight to be 7.8 deg. Since this twist was not included in preflight models, pitch motion of the orbiter did not induce pure, out-of-plane motion in the solar array.

Another anomaly was the curved blanket about the longitudinal axis (toward the mast) during darkness and shortly after coming into daylight. The curved blanket affected the dynamics of the deployed array, such that comparison of photogrammetry results with DAE results, except in a gross sense, is not warranted. It is very beneficial that dynamic tests were performed in both daylight and darkness, as will become evident in the discussion that follows.

5. Flight Data Analyses and Results. This section discusses and compares the three approaches for determining the deployed array dynamics.

a. Accelerometer Analyses. Figure 4 shows accelerometers located at the base of the mast and on the containment box cover. For on-orbit dynamics, the accelerometers at the base of the mast were of little value, because the major acceleration would be at the outer end of the mast. There were three single axis accelerometers on the cover. Two, near the center of the cover, measured X (pitch) and Y (yaw) accelerations. There was also one near the end of the cover measuring X (pitch) acceleration, making it possible to identify torsional motion of the array by comparison of acceleration from the two X measurements. Good data were recorded for all three accelerometers for all fourteen tests. These data were recorded on tape and returned to MSFC for analysis.

TABLE 4. DYNAMIC TEST CONFIGURATION

EVENT	CONFIGURATION	ENERGY INPUT
5	SAE 70% O/P	1.0
6	DAE 70% O/P	1.0
10	SAE 70% M/M	1.0
11	DAE 70% M/M	1.0
12	SAE 70% O/P	1.0
13	DAE 70% I/P	1.0
14	SAE 70% M/M	1.0
15	DAE 70% M/M	1.0
17	SAE 100% O/P	1.0
20	SAE 100% M/M	1.0
26	DAE 70% M/M	1.5
27	SAE 70% M/M	1.5
28	DAE 70% I/P	1.5
29	SAE 70% I/P	1.5

NOTATION:

SAE – PERFORMED IN ORBITAL DAYLIGHT WITH PHOTOGRAMMETRY DATA.

DAE – PERFORMED IN ORBITAL NIGHT TIME WITH DYNAMIC AUGMENTATION EXPERIMENT DATA.

O/P – OUT–OF–PLANE DYNAMICS OF THE ARRAY EXCITED BY PITCH MOTION OF THE ORBITER.

I/P – IN–PLANE DYNAMICS OF THE ARRAY EXCITED BY ROLL MOTION OF THE ORBITER

M/M – MULTI–MODAL DYNAMICS OF THE ARRAY EXCITED BY A COMBINATION PITCH–ROLL MOTION OF THE ORBITER.

ENERGY INPUT – 1.0 MEANS THAT THE PRE–FLIGHT PLANNED EXCITATION WAS USED AND 1.5 MEANS THE EXCITATION WAS CHANGED TO PROVIDE 1.5 TIMES THE NOMINAL ENERGY INPUT.

At MSFC, the accelerometer data were filtered and static bias adjusted by the MSFC Computer Services Office support contractors. The data were filtered of unwanted frequency content, and static bias in the accelerometers was removed so that the data could be integrated to provide velocity and displacement values. From the accelerometer data, the following information was obtained: (a) adjusted acceleration time histories; (b) power spectral density (PSD) plots for each acceleration time history; (c) displacement time histories, obtained by integrating the adjusted accelerations twice (with assumption that the velocity and displacement were zero at initiation of test); (d) and, finally, modal damping, calculated from the accelerometer PSD's using the half-power method. It was realized that values obtained from such analyses must be regarded as something less than exact. For example, all sources of dynamics information indicate the solar array was not completely at rest at initiation of test, even though the Shuttle vernier reaction control system had been deactivated for 10 minutes prior to start of test. Also, the bandwidth in the data reduction was not as small as desirable, but was as small as the recorded data would allow.

From the PSDs, it was possible to identify up to three modes for out-of-plane excitation, but from multimodal and in-plane excitation, only the primary mode could be identified. This is primarily due to the higher damping for in-plane motion that will be discussed later. Attempts were made to obtain displacement of higher modes by filtering out the lower frequencies, as well as high frequency. The quality of these plots does not warrant publication.

A typical acceleration plot is shown in Figure 10. For this plot, frequencies are filtered above 3 Hz. The same data are shown in Figure 11, with frequency data above 0.08 Hz filtered. Notice that the plot is much smoother with secondary modal accelerations removed. Figure 12 shows the power spectral density for the first out-of-plane test of the blanket at 70 percent extension. Note that three distinct frequencies are evident. A fourth, less pronounced peak at 0.11 Hz, is not fully understood. Figure 13 shows the displacement for the same case with filtering above 3 Hz. Displacement with filtering above 0.08 Hz is shown in Figure 14. Again, the curve is much smoother with secondary modal contribution removed.

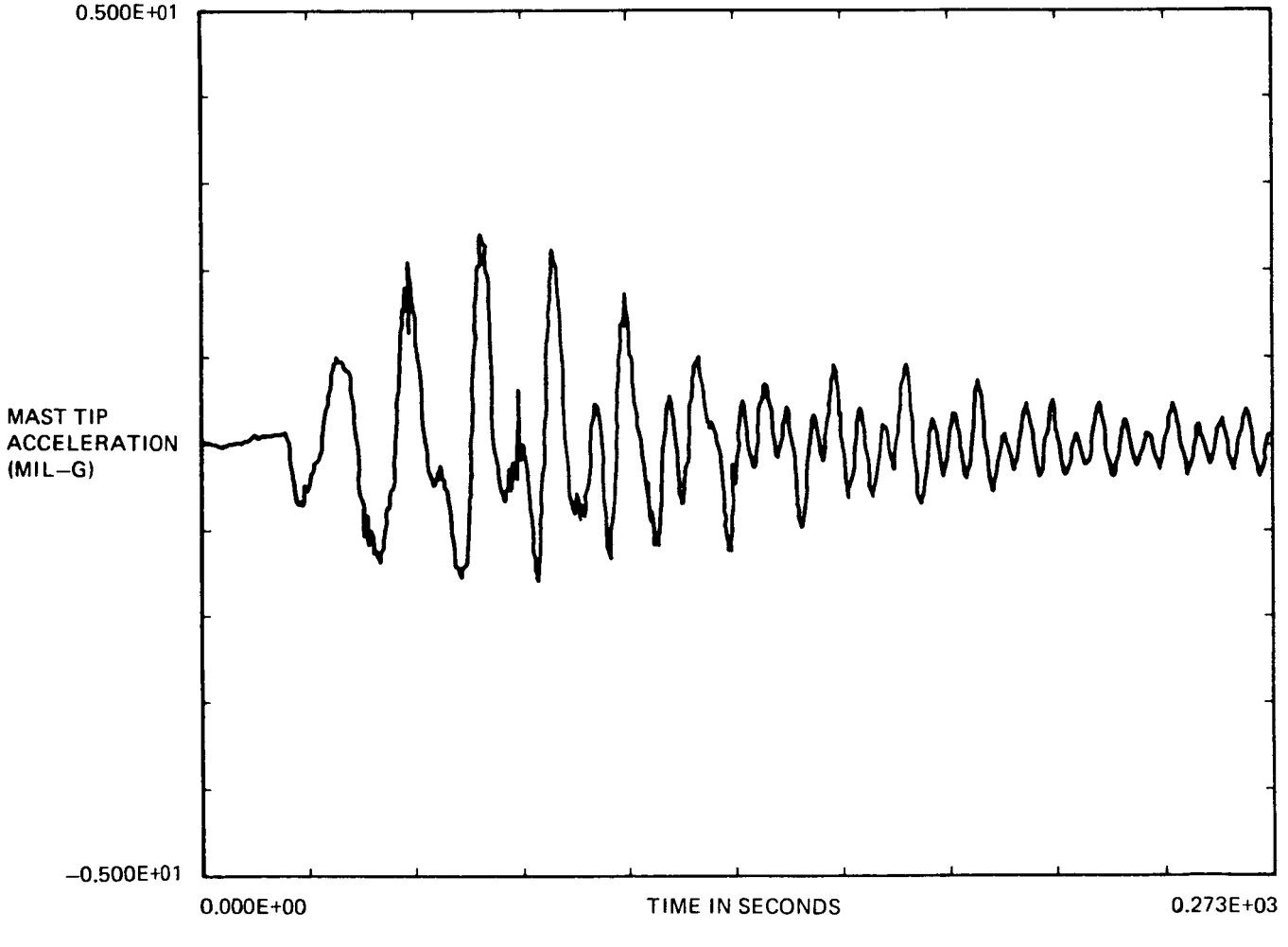

Figure 10. Mast tip acceleration for first out-of-plane test at 70 percent extension (event 5, accelerometer data, filtered above 3 Hz).

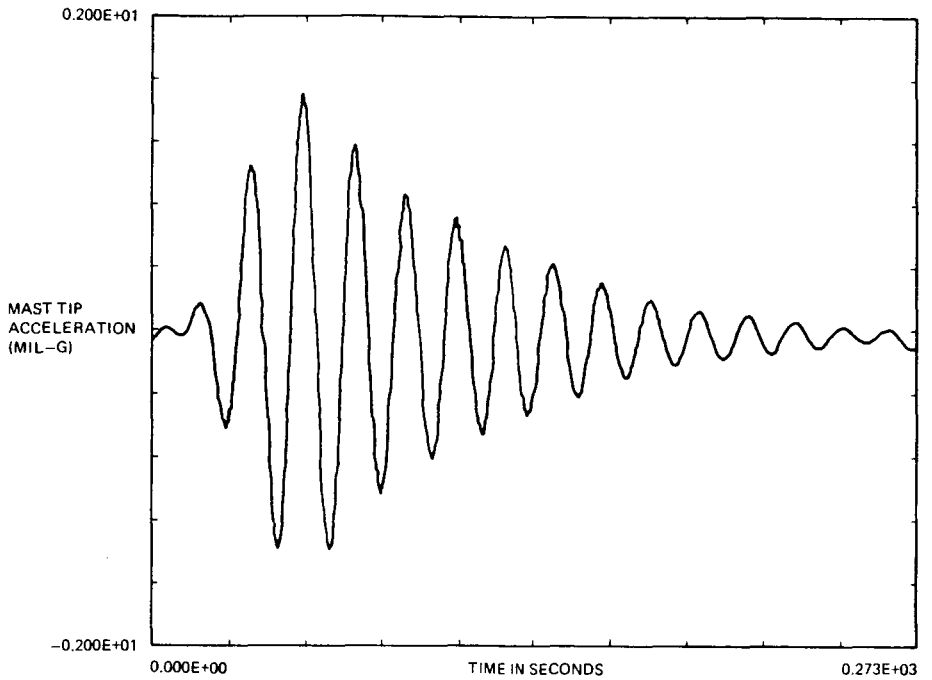

Figure 11. Mast tip acceleration for first out-of-plane test at 70 percent extension (event 5, accelerometer data, filtered above 0.08 Hz).

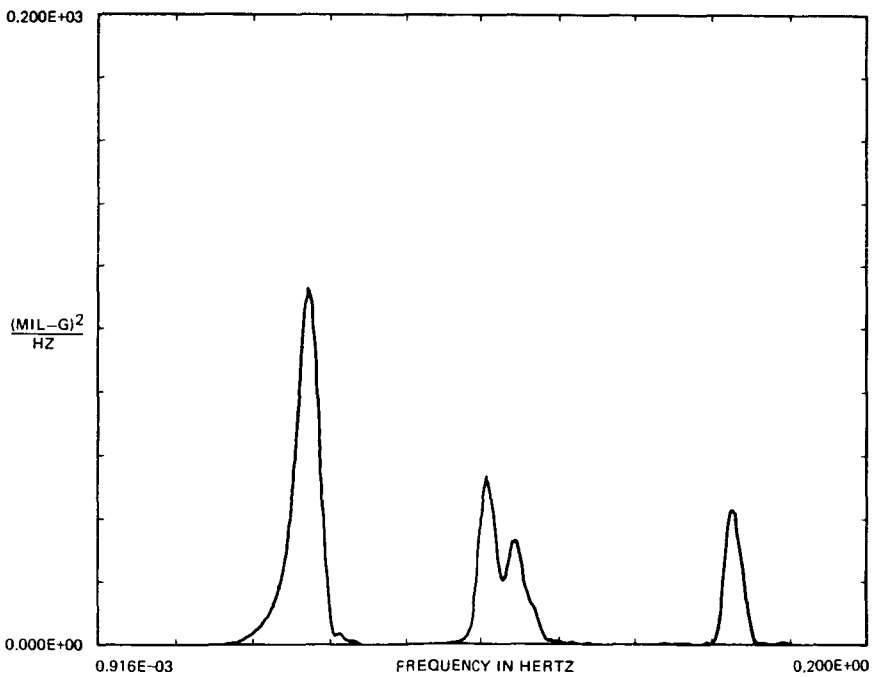

Figure 12. Power spectral density plot for first out-of-plane test at 70 percent extension (event 5, accelerometer data).

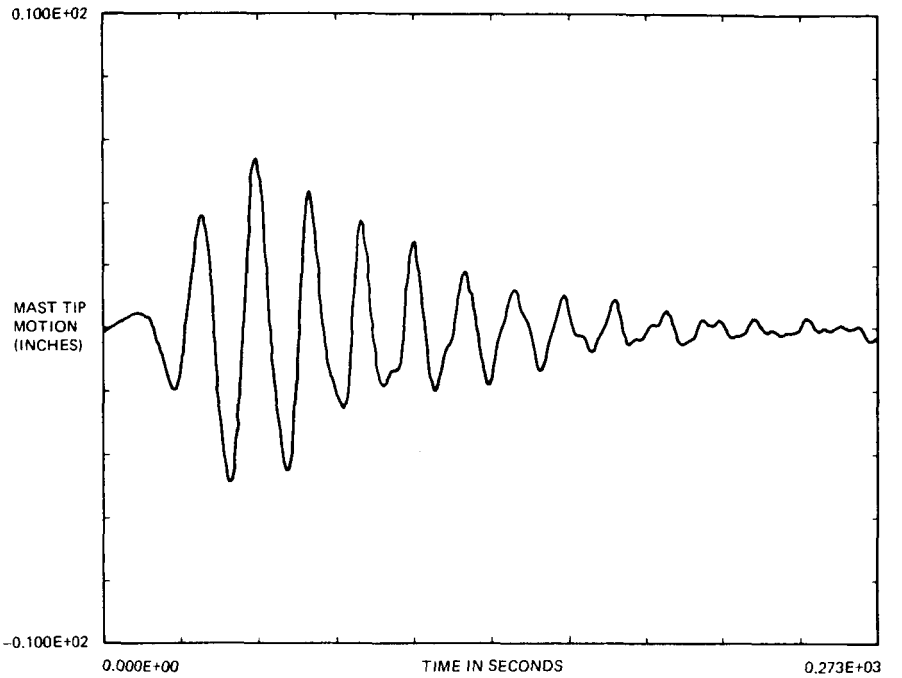

Figure 13. Mast tip displacement for first out-of-plane test at 70 percent extension (event 5, accelerometer data, filtered above 3 Hz).

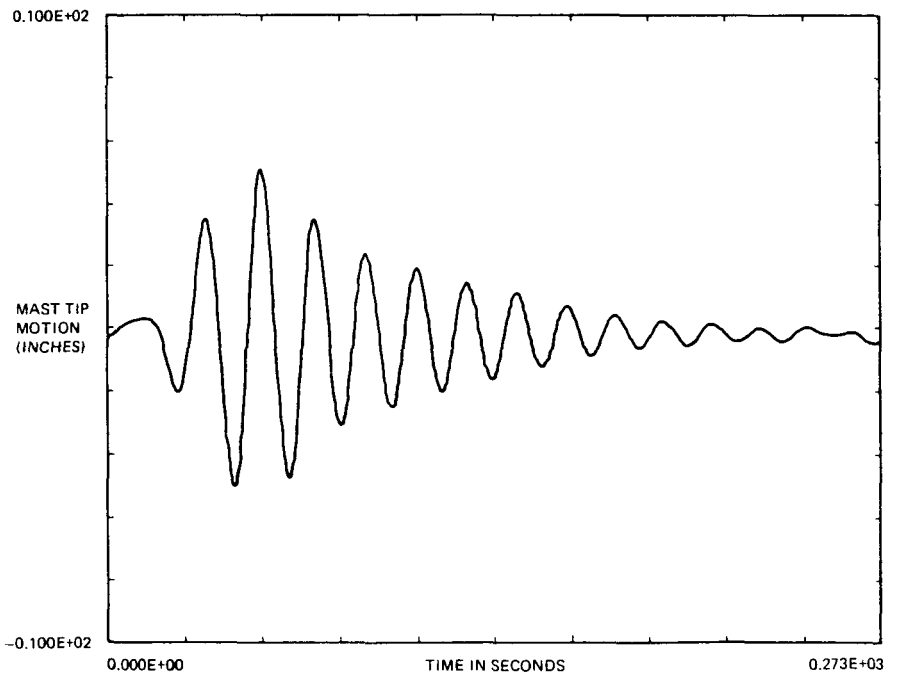

Figure 14. Mast tip motion for first out-of-plane test at 70 percent extension (event 5, accelerometer data, filtered above 0.08 Hz).

Table 5 gives a summary of dynamics test results from accelerometer data. Provided are test results and analysis results using 0.5 percent (Ref. 5) and 5.0 percent (Ref. 6) of critical damping. Preflight response analyses were performed with 0.5 percent damping, in order to be conservative in mast longeron load predictions. A postflight analysis was performed using 5.0 percent damping to show the effect on response amplitude.

It is noteworthy that there is more coupling of out-of-plane and in-plane motion than predicted in the preflight model. The twist in the mast resulted in some modal coupling; also accelerometer readings did not measure pure X and Y acceleration. For the report, the vector components have not been changed to reflect true X and Y acceleration.

The natural frequency of the deployed array was consistently higher in darkness than in daylight. The change in frequency is primarily due to the blanket curling phenomenon. A postflight analysis (Ref. 6) was performed to reflect the change in frequency due to mast twist, blanket curl, and both blanket curl and mast twist. A summary of this analysis is given in Table 6. It can be seen that the analysis shows curling phenomenon is the primary contributor to change in frequency between daylight and darkness.

TABLE 5. SAFE DYNAMIC TEST RESULTS FROM MAST TIP ACCELEROMETERS

SOLAR ARRAY DEPLOYED POSITION (%)	MODE	FREQUENCY TEST/ANALYSIS*	DAMPING	X DEFLECTION (INCHES) TEST–ANALYSIS 0.5%/5.0%	Y DEFLECTION (INCHES) TEST–ANALYSIS 0.5%/5.0%
70	O/P DAY	.056/.059	3.0	10.5–14.5/12.0	2.4–0.3/0.2
70	O/P NIGHT	.059/.059	6.0	10.0–14.5/12.0	2.2–0.3/0.2
70	I/P DAY	.062/.066 1.5 ENERGY	HIGH	1.2–1.0/–	5.5–15.8/–
70	I/P NIGHT	.070/.066	HIGH	1.2–1.0/0.8	5.0–12.0/7.1
70	M/M DAY	.058/.059	8.0	4.0–8.8/4.0	3.6–12.0/4.4
70	M/M NIGHT	.066/.059	11.0	4.4–8.8/4.0	2.6–12.0/4.4
100	O/P DAY	.037/.034	2.0	18.0–27.2/23.7	3.4–0.2/0.2
100	M/M DAY	.037/.034	4.0	14.0–18.3/15.9	5.0–19.2/14.7
70	O/P	.099/.119	–	–	–
70	O/P DAY	.165/.196	–	–	–
100	O/P DAY	.095/.097	–	–	–
100	O/P DAY	.151/.153	–	–	–

*Reference 7

Another observation is that the damping is consistently higher for in-plane motion than for out-of-plane motion. LMSC, in a search for an explanation to this phenomenon, performed a simple approximation analysis to show that if the tension wire reel-out force were greater than the reel-in force by as little as 1.0 lb, then the entire kinetic energy would be dissipated in one-half cycle of motion in the free response period. Consequently, a postflight test on a single constant torque mechanism was conducted, and the difference in wire tension force between reel-out and reel-in was found to be about 0.65 lb. A paper (Ref. 8) prepared by Mr. Earl Pinson of LMSC, documents this test and was given in the proceedings of the 20th Aerospace Mechanisms Symposium.

TABLE 6. PARAMETRIC DYNAMIC FREQUENCY STUDY RESULTS FOR 70 PERCENT DEPLOYED ARRAY

MODE	NOMINAL FREQUENCY –HZ–	FREQUENCY WITH MAST TWIST –HZ–	FREQUENCY WITH BLANKET CURL –HZ–	FREQUENCY WITH TWIST AND CURL –HZ–
1	.0593	.0594	.0644	.0643
2	.0662	.0668	.0671	.0671
3	.0764	.0853	.1142	.1154
4	.1191	.1193	.1880	.1794
5	.1454	.1653	.2016	.2136

In summary, where the test results did not agree with preflight analyses, postflight analyses and tests have been performed to provide a logical explanation for the differences.

b. Photogrammetry Analyses. A typical result of photogrammetry triangulation is shown in Figure 15. These are 3-D (3 Dimensional) displacement time histories in the orbiter X, Y, and Z axes that have been developed from 4 simultaneous 2-D CCTV images. The X axis is along the axis of the orbiter payload bay; the Y axis is in the plane of the wings; and the Z axis is perpendicular to the plane of wings.

After the 3-D time histories are obtained, the next major step of the analysis process is application of system identification techniques to determine the dynamic characteristics of the solar array. To obtain some "quick look" results from flight test data, standard Fast Fourier Transform (FFT) analysis was applied to the X axis plot from Figure 15. These data are from a test at 100 percent extension in which the excitation was chosen to excite the out-of-plane bending modes. Figure 16 shows a frequency plot obtained by the FFT analysis. The two frequencies clearly identified (0.038 Hz and 0.097 Hz) are very close to the preflight predicted frequencies for the first and second out-of-plane bending modes. Using the same response curves from Figure 15, a damping factor of 3.3 percent was calculated using the Eigensystem Realization Algorithm (ERA). The ERA system is a time domain analysis technique, developed at Langley Research Center by Mr. Richard S. Pappa and Dr. Jer-Nan Juang. Developed from principles proposed for use in the controls field, the ERA system constructs an analytical model, or realization, of a structure from measurements of its free-decay dynamic responses. Reference 9 gives a thorough discussion of the ERA system. Figure 17 shows curves representing various assumed damping factors overlayed on the plot of X axis motion from Figure 15. The important point to note here is that the damping factor calculated from flight data is significantly higher than the 0.5 percent factor that was assumed for the preflight predictions.

After the above preliminary determinations, efforts were concentrated on detailed applications of the ERA system to two tests, one at 70 percent deployment and one at 100 percent deployment, in which excitations were designed to excite multimodal responses. As an aid in interpreting dynamic responses, the ERA analysis was performed using an ICASE technique, as illustrated in Figure 18. A "data window," 250 data points wide, was established from the beginning of the free-decay response. With a sample rate of three samples per second, this "data window" is approximately 83 sec long and covers three complete response cycles. An ERA analysis was done on this data segment, then the "data window" was moved down stream five data points, or approximately 1.67 sec in time, and the ERA analysis repeated. This sequence was repeated until 100 cases were analyzed. Typical results for a multimodal test at 100 percent deployment are shown in Figures 19 and 20. Figure 19 shows results for motion in the X direction and Figure 20 shows Y direction results. Frequency is shown in the left plot, and zero-to-peak displacements are plotted on the right. The ordinate is the ICASE number or the number of the ERA analysis case. Moving up the ordinate, from ICASE-1 to ICASE-100, corresponds to increasing time in the response curves. Notice in Figure 19 that a very dominant mode occurs at just less than 0.04 Hz. There are four other frequencies identified, but their maximum amplitudes are much less than the first mode. In Figure 20, the amplitudes are much less for the Y direction motions, but the second frequency of approximately 0.06 Hz shows up more clearly.

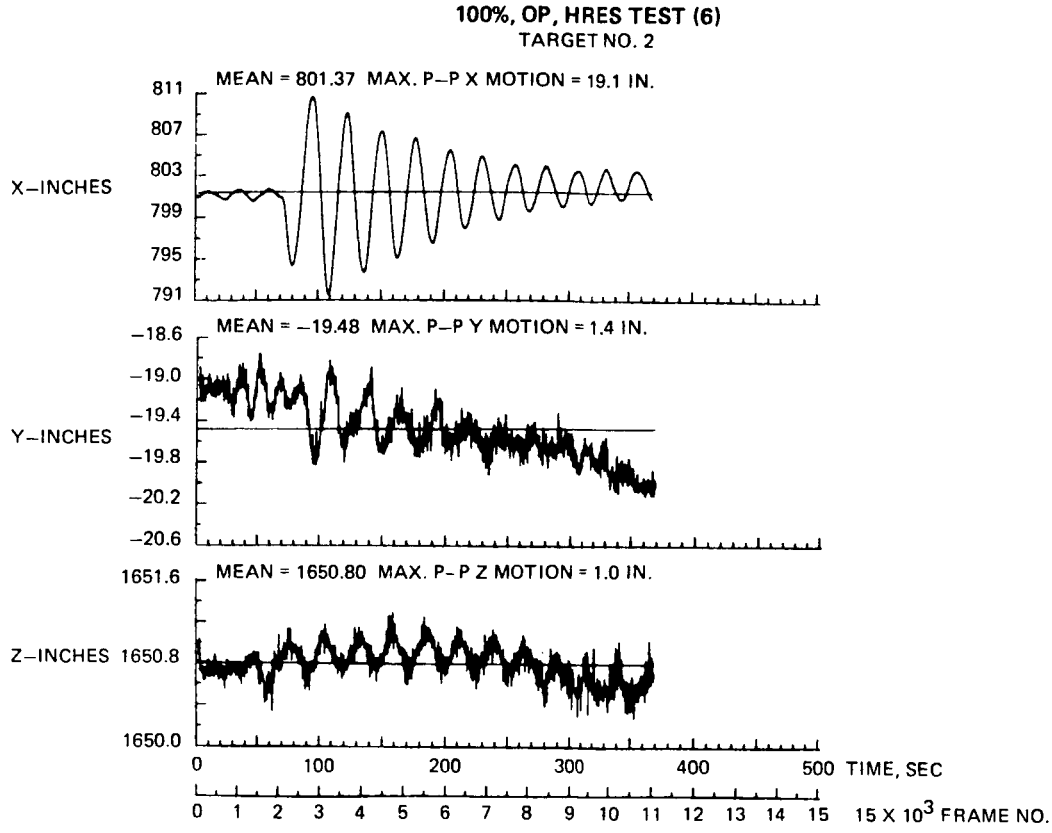

Figure 15. Typical 3-D displacement time history from photogrammetric triangulation process.

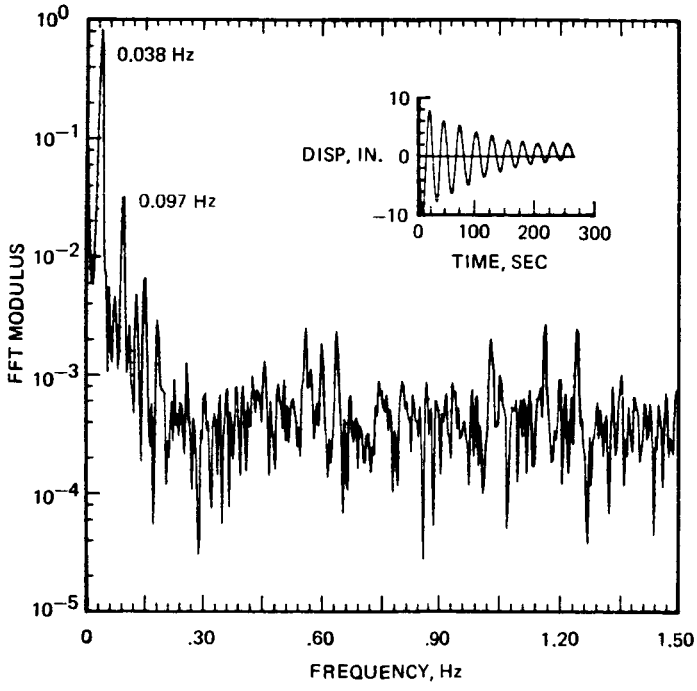

Figure 16. Results of FFT analysis of target displacement in the out-of-plane direction, 100 percent array deployment (photogrammetry experiment).

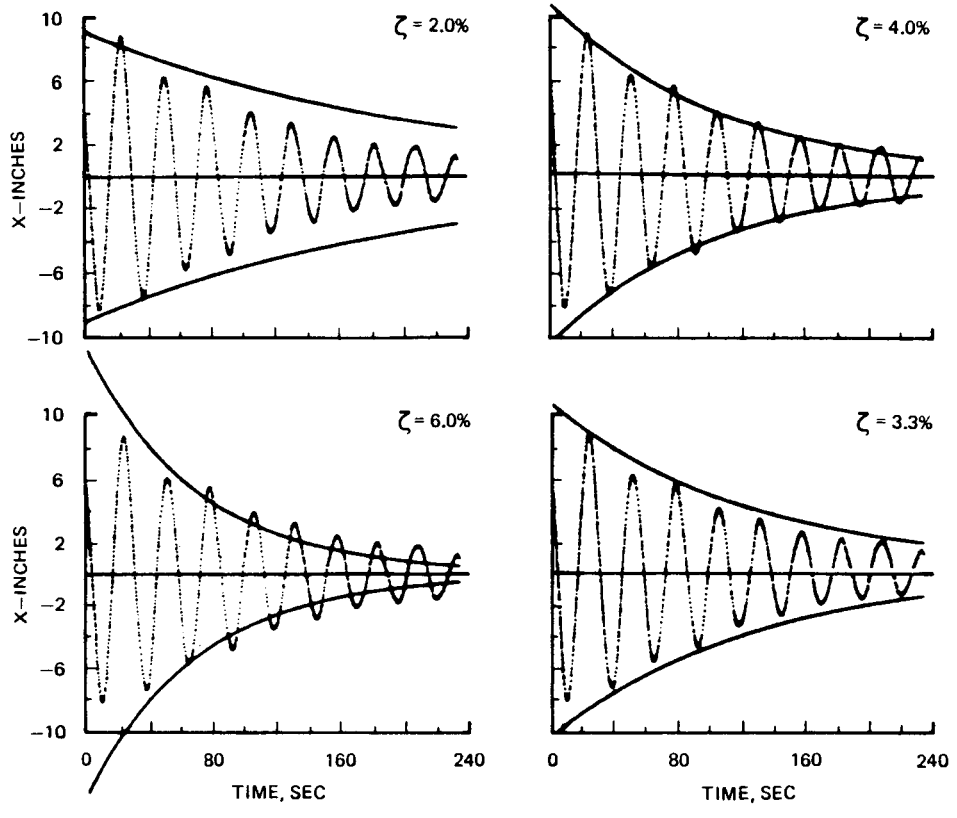

Figure 17. Calculated and assumed damping curves overlayed on plots of out-of-plane displacement, 100 percent array deployment (photogrammetry experiment).

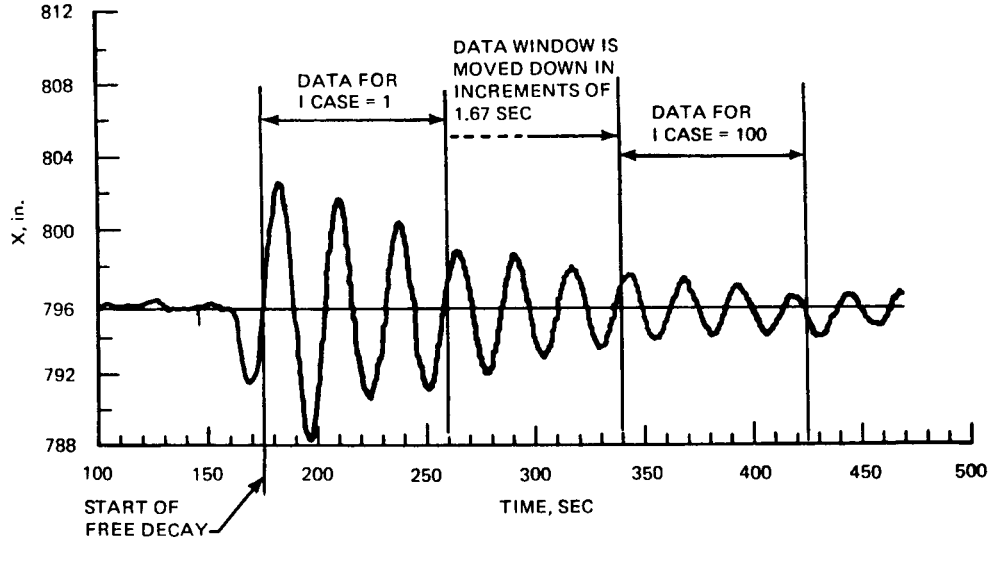

Figure 18. Illustration of ICASE multiple analysis technique (photogrammetry experiment).

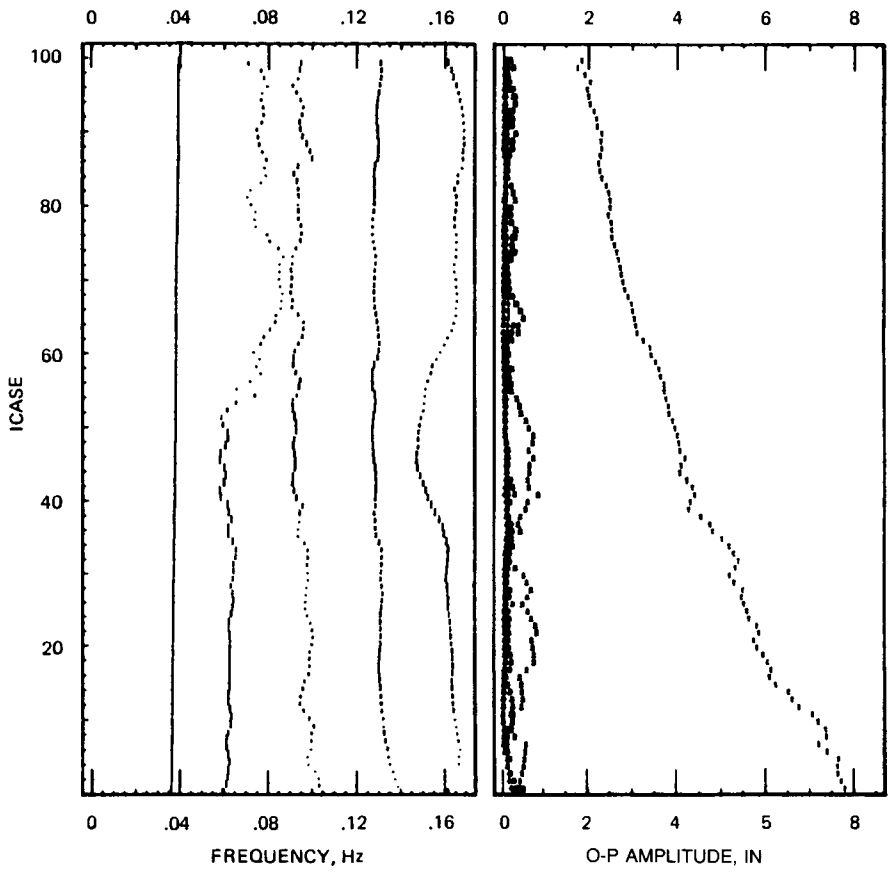

Figure 19. Typical results of multiple ERA analyses of out-of-plane tests (photogrammetry experiment).

Much difficulty was experienced in determining reliable damping factors for any but the first mode. This is not surprising when one considers the extremely low frequencies of the solar array dynamic response and the small amplitudes of the higher modes. Further examination of Figures 19 and 20 indicate that only the first mode appears to be even close to an exponential decay. Frequency information for mode 1 has been expanded in Figure 21, with damping factor replacing displacement in the right hand plot. Not only is the frequency seen to increase in time, but damping factor decreases from about 4.0 percent down to near 3.0 percent. These results indicate that the solar array dynamic characteristics are definitely non-linear.

Application of the ERA system identification technique to the solar array flight data has to date identified eight specific modes in the dynamic response. They are summarized in Table 7 and compared to preflight analytical predictions. Five of the first six modes at 70 percent deployment and three of the first four modes at 100 percent deployment have been identified from data obtained using CCTV photogrammetry measurements. Note that in both configurations, the predicted first in-plane bending mode has not been identified. In Figures 22 a through h, plots of each mode identified from flight test data are compared to the preflight, analytically predicted mode. The figures show an oblique view looking from above the X-Y plane (or the plane of the orbiter wings) and a side view looking along the Y axis in the plane of the solar array blanket, perpendicular to the X axis. Figures 22b and 22g show a view looking along the X axis down the payload bay instead of the side view. The lines at the bottom of the individual plots are a stick model representation of the orbiter, between the location of the solar array and the location of the vernier control thrusters used for excitation. This stick model plot is not complete in any of the Figures, except the X axis views in Figures 22b and 22g.

TABLE 7. SUMMARY OF WING DYNAMIC FREQUENCY TEST RESULTS COMPARED TO PREDICTIONS (PHOTOGRAMMETRY EXPERIMENT)

70% DEPLOYMENT

MODE	ANALYSIS –HZ–	TEST –HZ–
FIRST O/P BENDING	0.0594	0.059
FIRST I/P BENDING	0.0671	NOT YET IDENTIFIED
FIRST TORSION	0.0765	0.076
SECOND O/P BENDING	0.1191	0.114
SECOND TORSION	0.1454	0.148
THIRD O/P BENDING	0.1961	0.160

100% DEPLOYMENT

MODE	ANALYSIS –HZ–	TEST –HZ–
FIRST O/P BENDING	0.0345	0.037
FIRST I/P BENDING	0.0378	NOT YET IDENTIFIED
FIRST TORSION	0.0576	0.057
SECOND O/P BENDING	0.0966	0.098

Two approaches were taken to assess the capability of the CCTV based photogrammetry system to resolve motions of the solar array during orbital testing. First, statistical studies were done on the results from the triangulation analyses of a test at 100 percent deployment. Considering 20 targets seen by all four cameras, 1-sigma RMS displacement accuracies were calculated from a section of data during the quiescent period, prior to dynamic excitation. Results show that measurement of relative displacement at a distance of 31 m away is accurate to better than 1.0 mm in both X and Y directions. From the same segment of data during the quiescent period, peak to peak motions of targets at the tip of the solar array, 31 m away, were calculated to be 1.5 cm (0.59 in.) in the X direction and 0.44 cm (0.175 in.) in the Y direction. This is a significant result, in that it shows the solar array was not truly quiescent prior to dynamic excitations. In fact, all CCTV data that have been reduced to date show some residual motion of the solar array, during the quiescent period prior to dynamic excitation. No conclusive evidence has been found to identify the cause of this low-amplitude oscillation. It appears that the solar array is being driven by some low-level disturbance such as aerodynamic drag or some small background disturbances from the shuttle orbiter. Although the relative magnitude of this quiescent displacement is not large, it is important to know it is there since it could affect determinations such as damping calculations of higher order modes where the amplitude is of the same order of magnitude as the quiescent displacements.

c. Dynamic Augmentation Experiment Analyses. Data were obtained on all targets, on all tests, even though some targets were outside of their nominal positions due to the array blanket darkside curvature. The array excitations and data take started near orbital midnight and continued for 12 min.

The eighteen targets for the six 70 percent tests each provided X and Y displacement data for a total of 36 data samples per test. All 36 data samples were simultaneously evaluated by two different response analysis techniques. Both techniques utilize a time-domain curve fit of the data to obtain the modal damping information, and a Fast Fourier Transform technique to obtain modal amplitude and phase relationships.

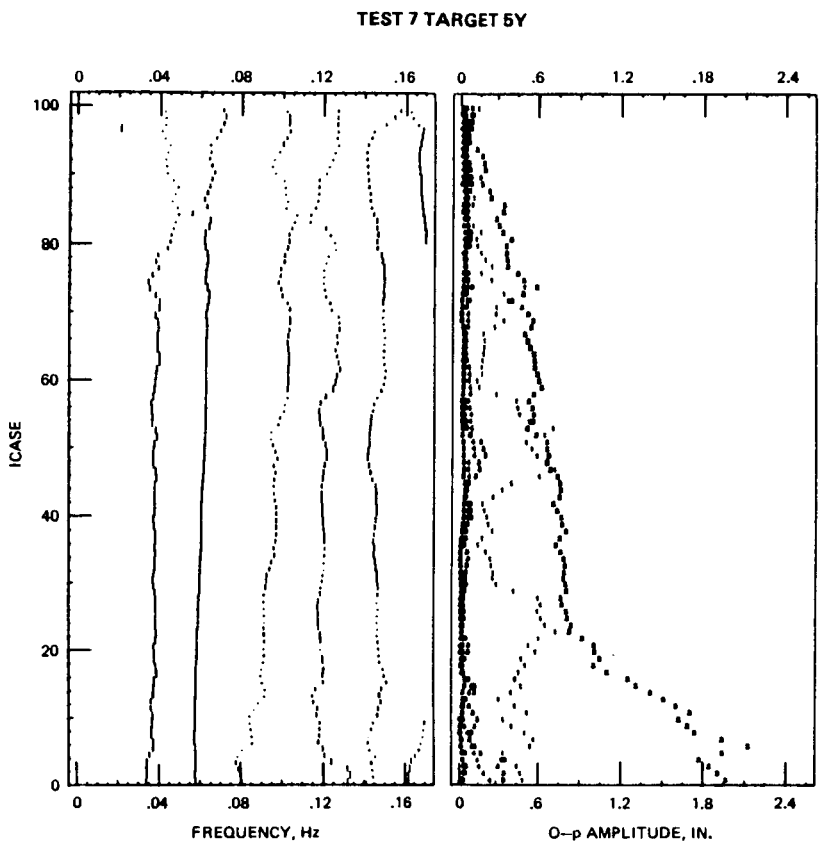

Figure 20. Typical results of multiple ERA analyses of in-plane tests.

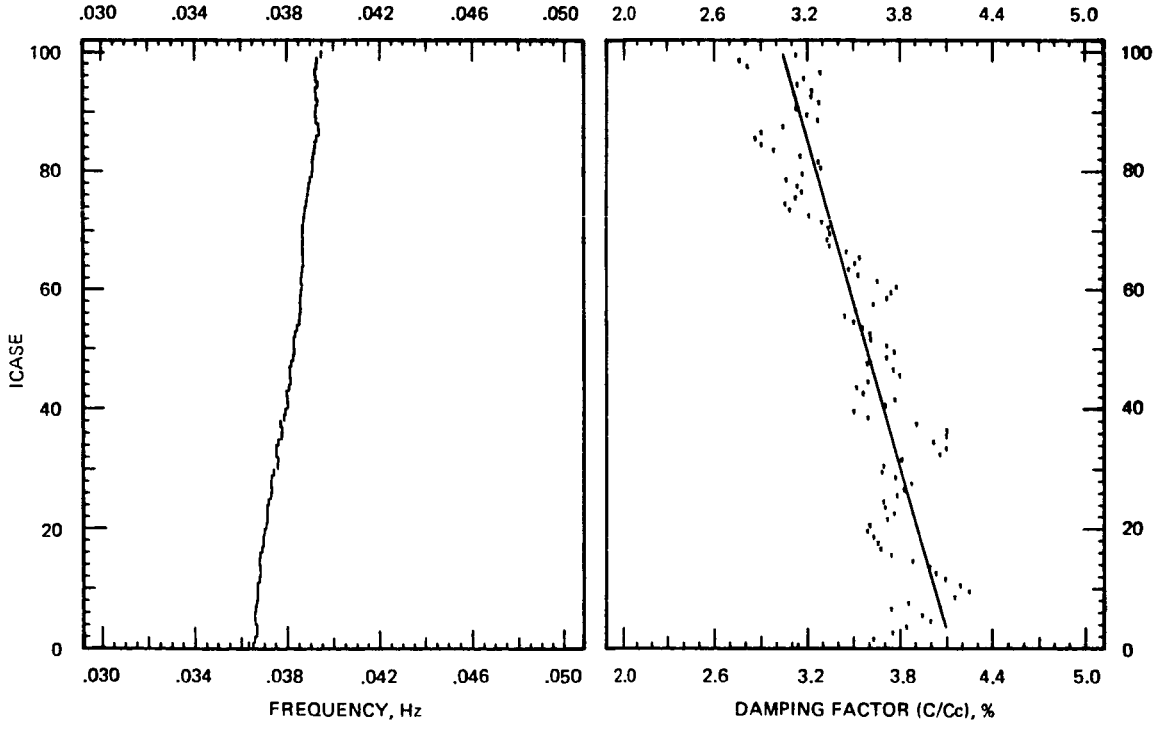

Figure 21. Expanded frequency and damping factor results for first mode, 100 percent array deployment (photogrammetry experiment).

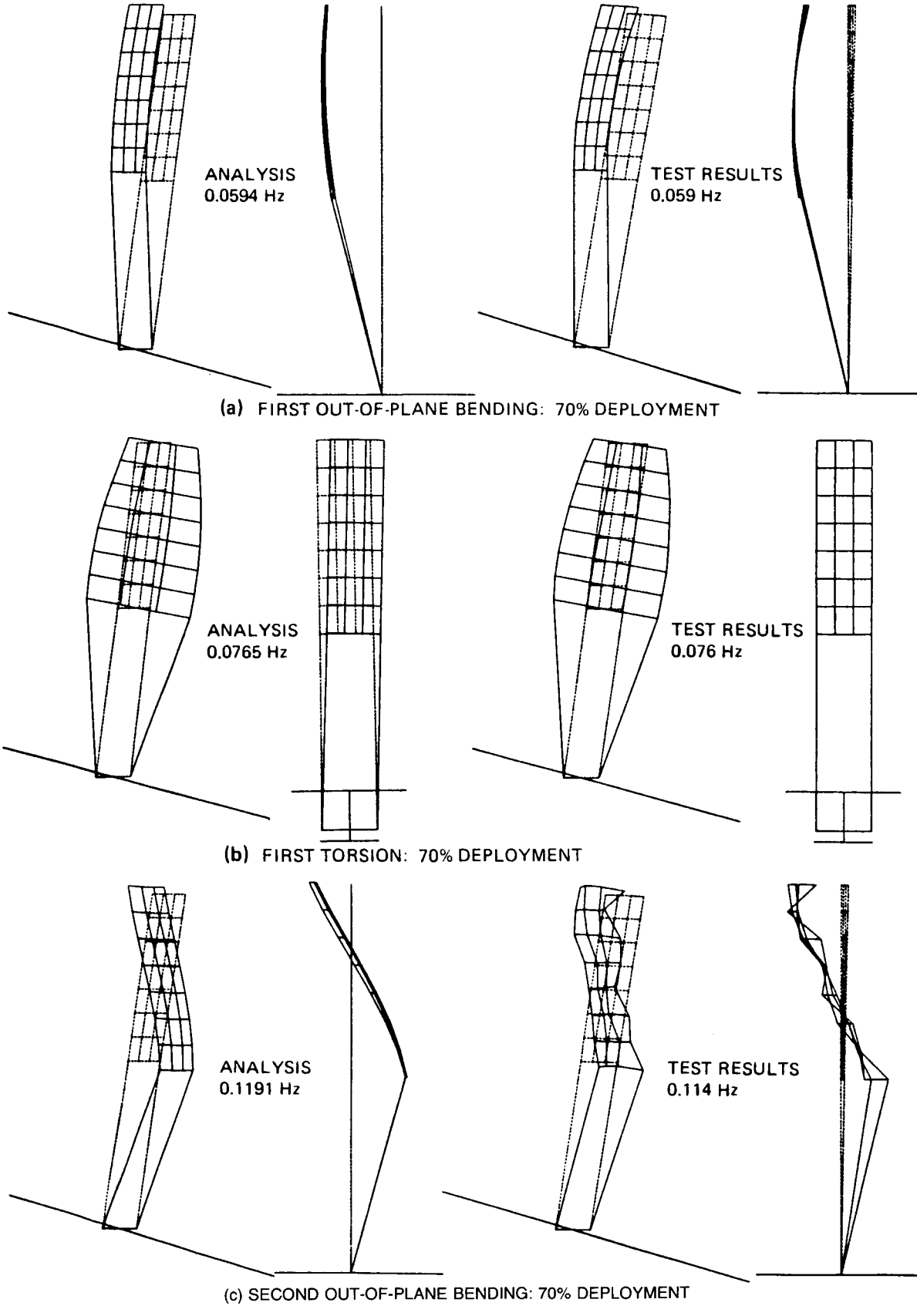

Figure 22. Array dynamics analysis/test comparison (photogrammetry experiment).

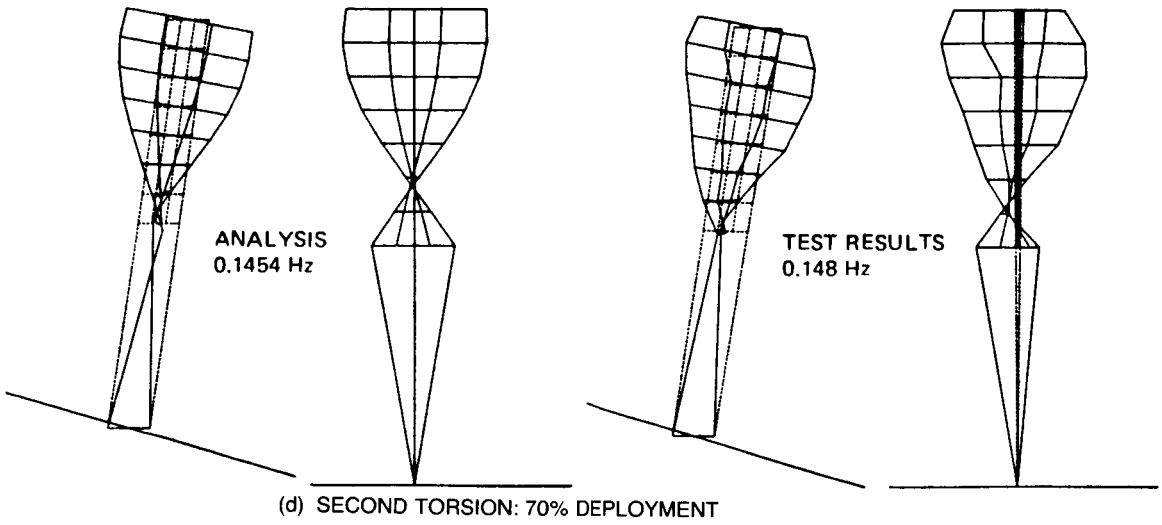

(d) SECOND TORSION: 70% DEPLOYMENT

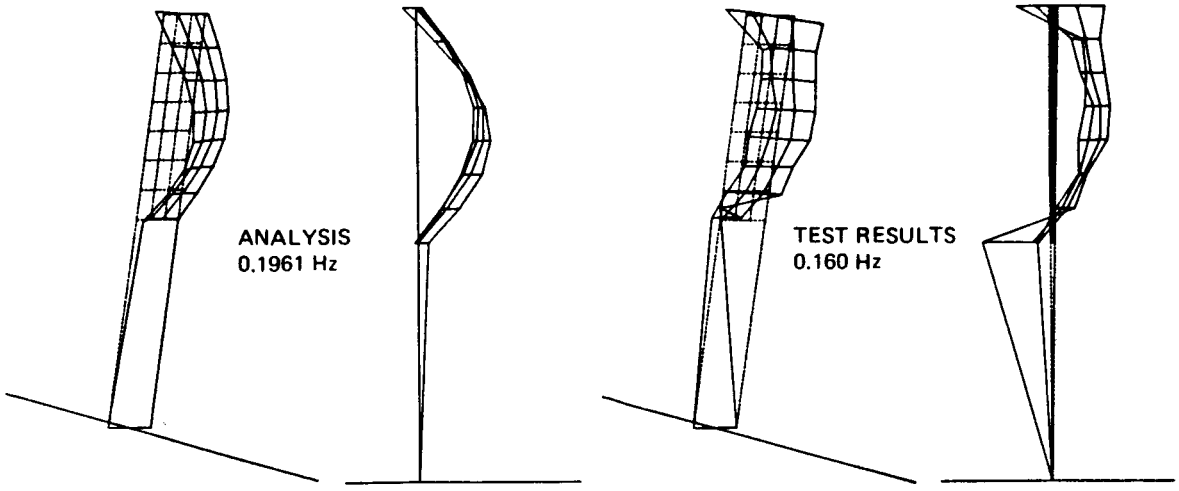

(e) THIRD OUT-OF-PLANE BENDING: 70% DEPLOYMENT

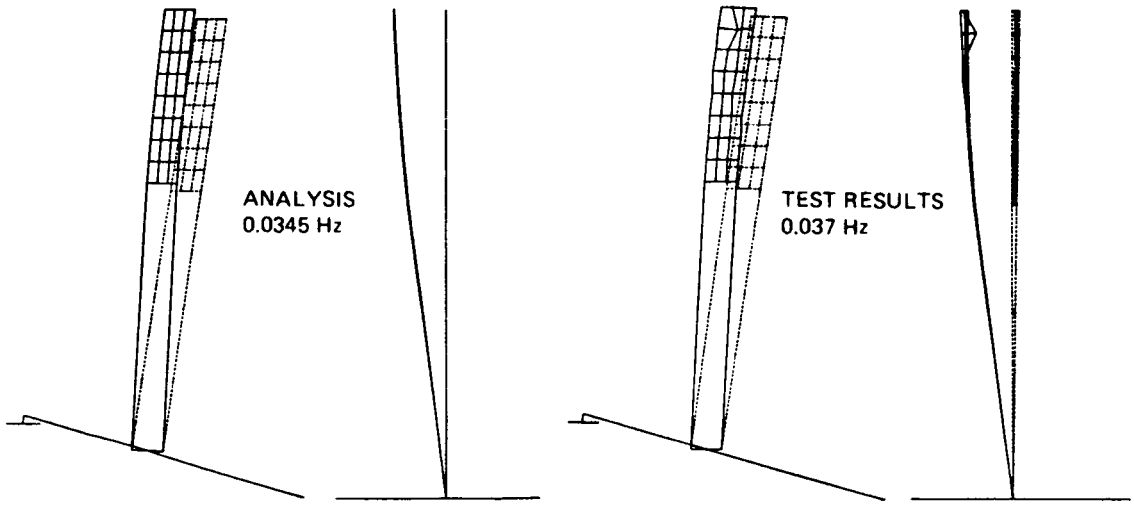

(f) FIRST OUT-OF-PLANE BENDING: 100% DEPLOYMENT

Figure 22. (Continued)

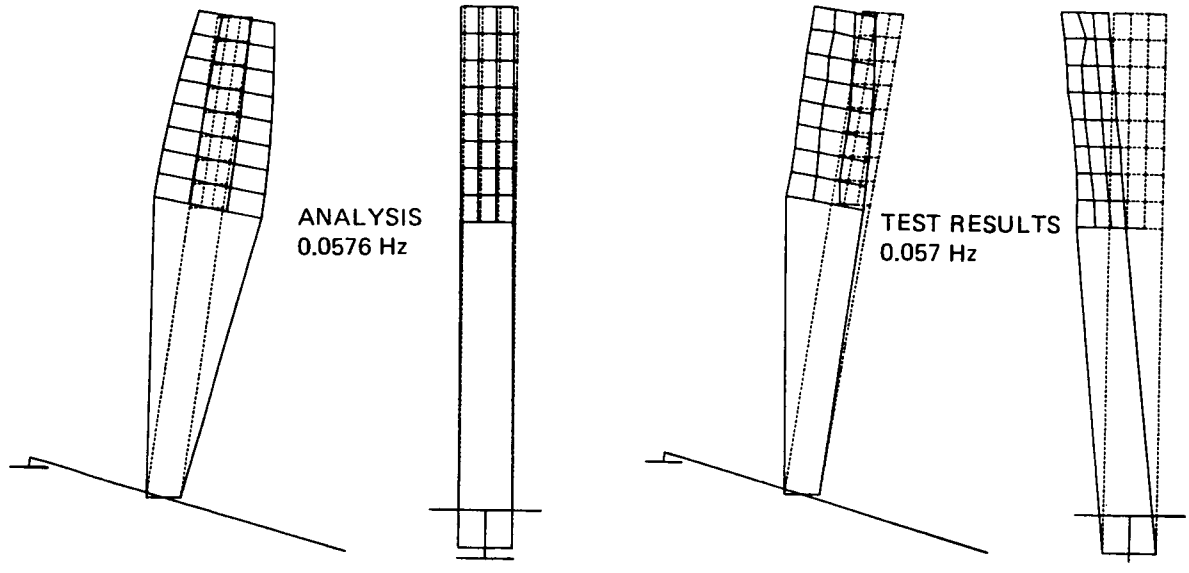

(g) FIRST TORSION: 100% DEPLOYMENT

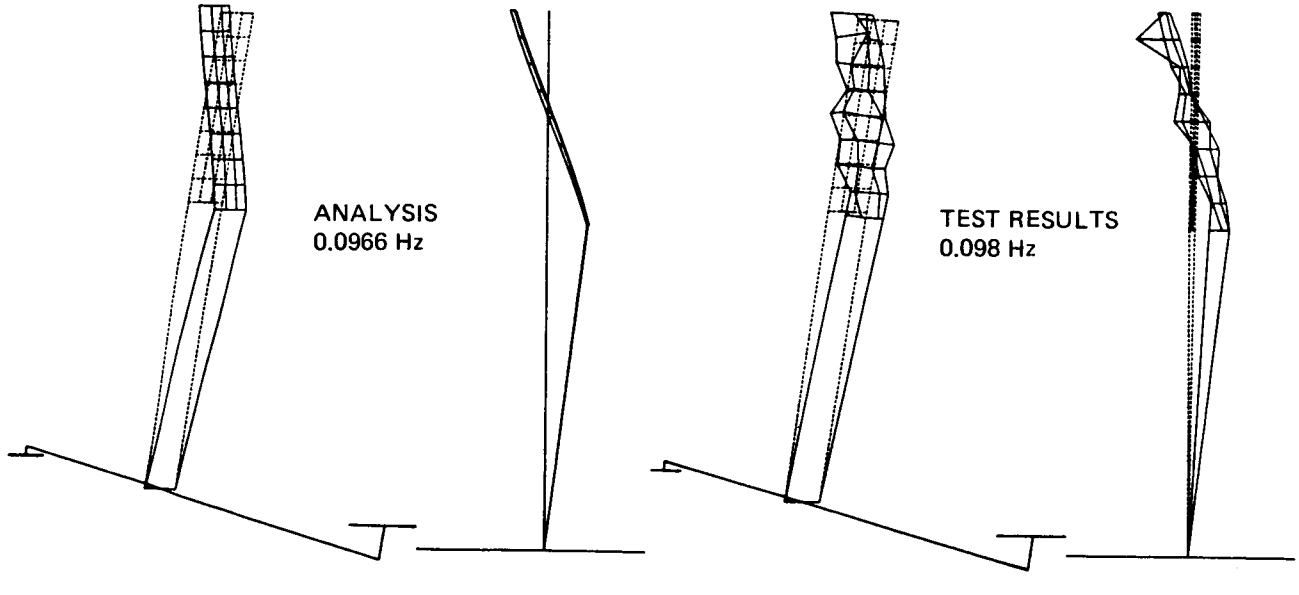

(h) SECOND OUT-OF-PLANE BENDING: 100% DEPLOYMENT

Figure 22. (Concluded)

The structural dynamic natural frequencies and mode shapes, both analytical and measured are compared in Figures 23a through 23e and Table 8. As noted in the data, the second analytical mode was not able to be extracted. This mode is a lateral response, and significant effort was expended to excite it with in-plane and multimodal tests. Mode shapes tended to match well, but natural frequencies not only differed, but changed in test from different excitations and during decay from each individual excitation. This phenomenon is characteristic of significantly nonlinear structures. The nonlinearity of the structure is illustrated in Figures 24 and 25. Figure 24 is a plot of the first mode (out-of-plane deflection) natural frequency versus tip displacement for the first DAE test. This test is illustrated, because it obtained the maximum tip response of all tests; therefore, providing the largest range of frequency and damping change. At a tip displacement of approximately 2 cm peak-to-peak, the frequency remained constant. The 0.059 to 0.072 Hz frequency change amounts to a 22 percent change. The damping change for the same mode, same test is illustrated in Figure 25. From a tip displacement of 11 cm single amplitude (SA) to 2 cm SA, the damping factor averages about 0.08. For less than 2 cm SA, the factor averages approximately 0.02.

In summary: (1) the DAE experiment successfully measured the SAFE solar array dynamic response, even under out-of-design conditions and; (2) four of the first five solar array modal characteristics were successfully test determined. Additional details describing the DAE, its design, method of operation, analyses, and flight experiment results can be found in Reference 10.

d. Comparison of Results. Since all photogrammetry data were obtained in daylight, and all DAE data were obtained in darkness, a direct comparison of test results is unwarranted, because of the before mentioned curling phenomenon. However, accelerometer data were obtained for all test cases and can be compared directly with each of the other data sets.

TABLE 8. SOLAR ARRAY DYNAMIC CHARACTERISTICS
(DYNAMIC AUGMENTATION EXPERIMENT)

ANALYTICAL FREQUENCY* HZ	MODE SHAPE	TEST FREQ. HZ	DAMPING %
0.064	OUT OF PLANE BENDING	0.059–0.072	2–8
0.067	IN PLANE BENDING	NOT IDENTIFIED	
0.115	1ST TORSION	0.089–0.092	1–2
0.179	2ND OUT OF PLANE BENDING	0.121	2–4
0.213	2ND TORSION	0.172	2

*POST FLIGHT ANALYSIS WITH WING TWIST AND CURL INCLUDED.

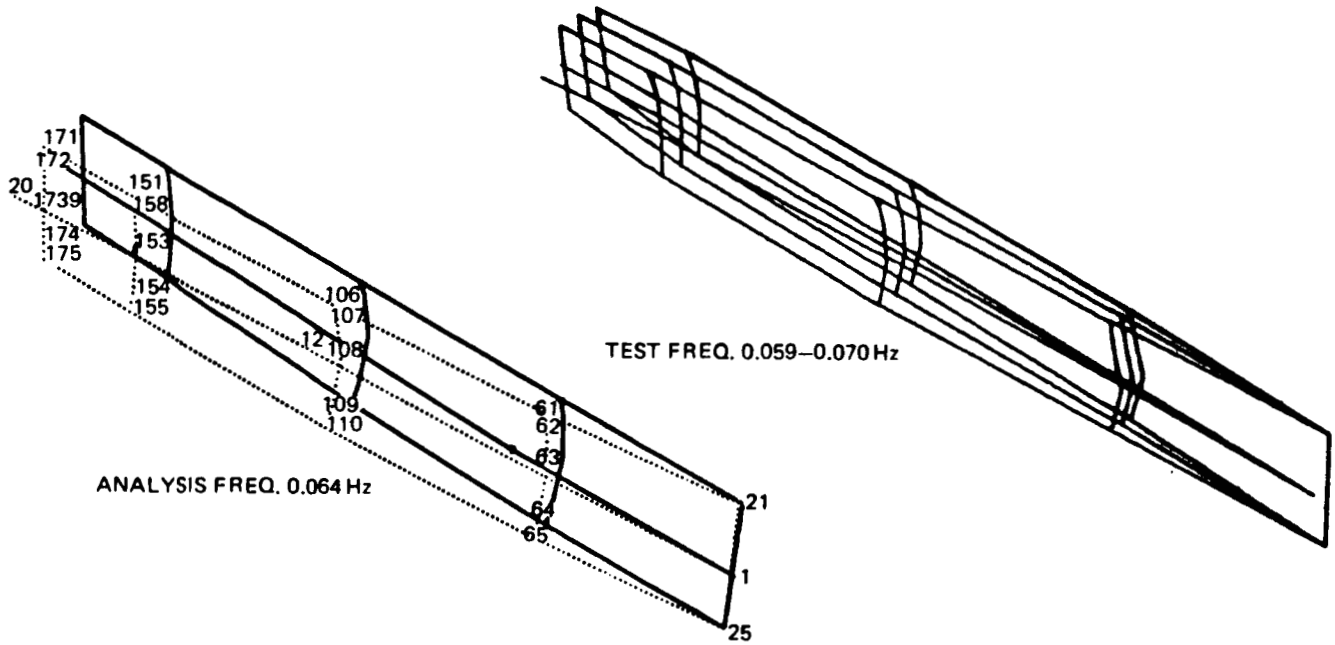

(a) 1ST MODE OUT-OF-PLANE BENDING; 70% DEPLOYMENT

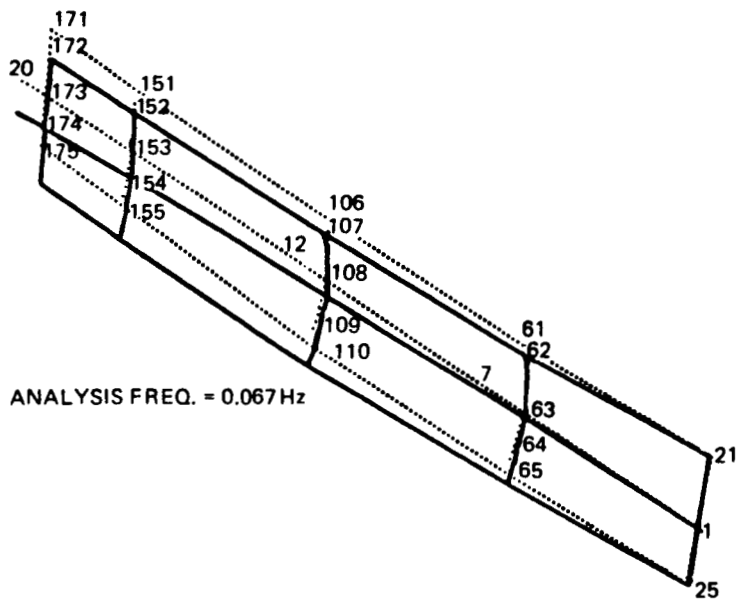

(b) 2ND MODE LATERAL BENDING; 70% DEPLOYMENT

Figure 23. Array dynamics analysis/test comparison (Dynamic Augmentation Experiment).

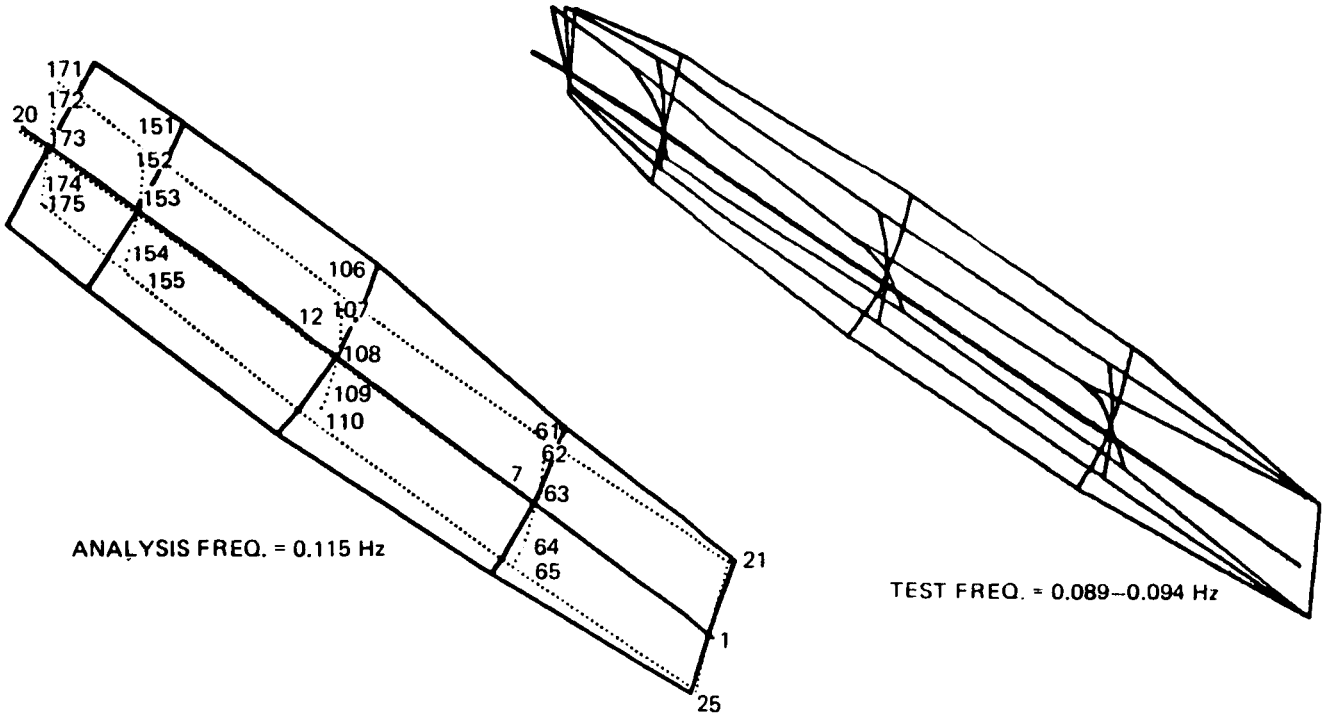

(c) 3RD MODE 1ST TORSION; 70% DEPLOYMENT

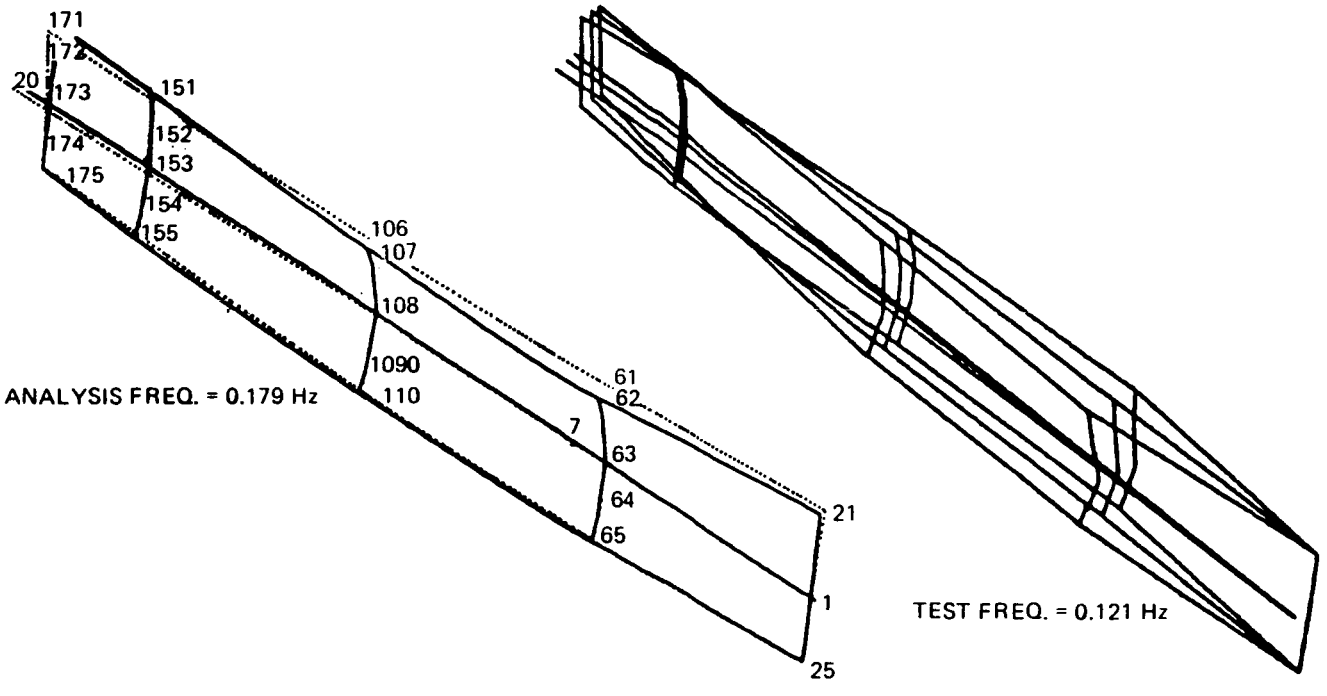

(d) 4TH MODE 2ND OUT-OF-PLANE BENDING; 70% DEPLOYMENT

Figure 23. (Continued)

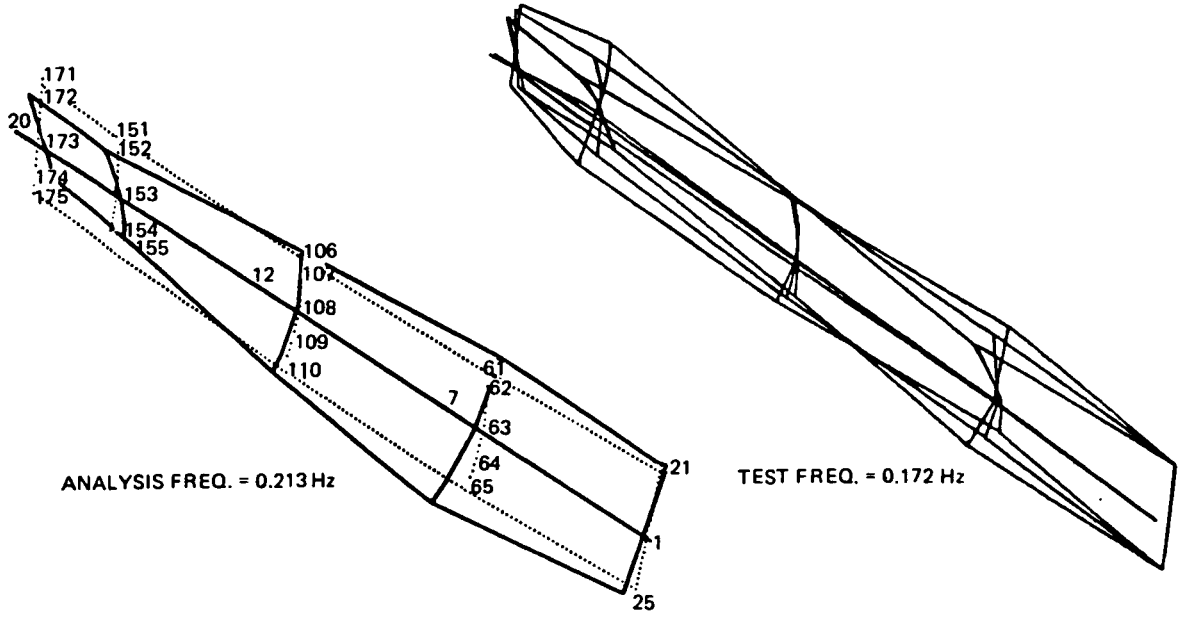

(e) 5TH MODE 2ND TORSION; 70% DEPLOYMENT

Figure 23. (Concluded)

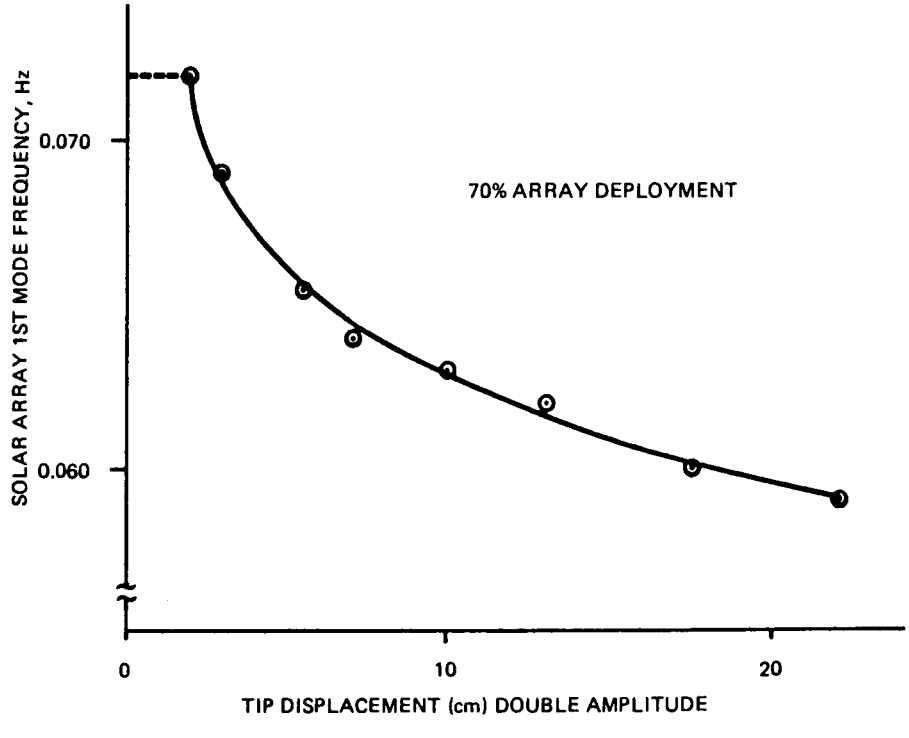

Figure 24. First mode natural frequency versus tip displacement (Dynamic Augmentation Experiment).

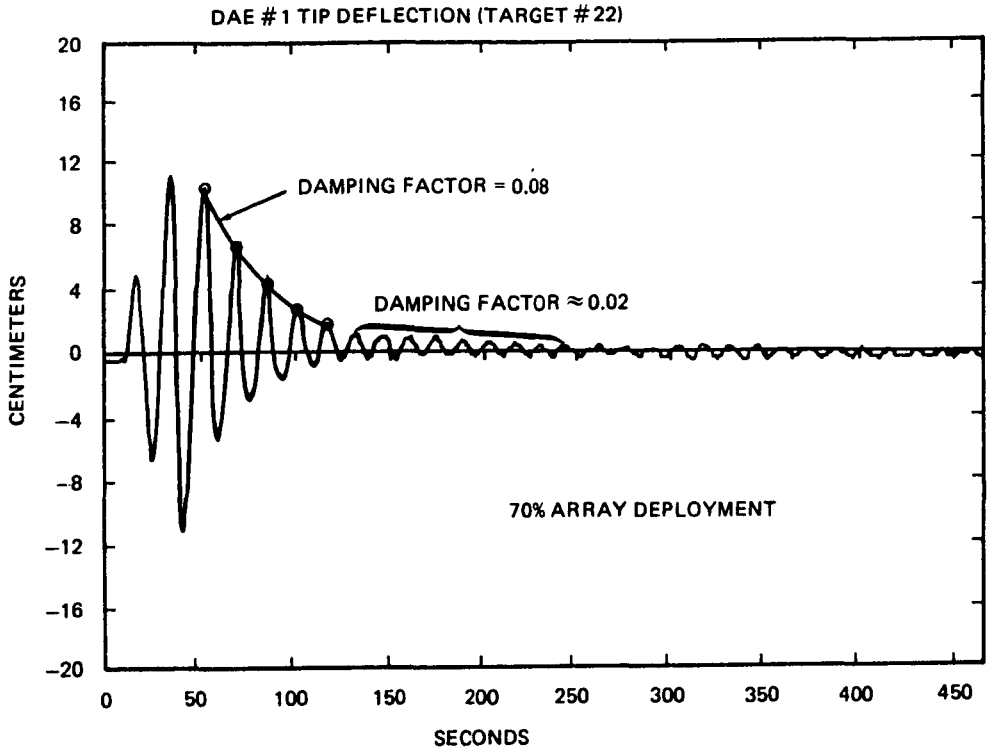

Figure 25. Solar array tip displacement versus time (Dynamic Augmentation Experiment).

Table 9 shows a comparison of frequencies obtained from photogrammetry measurement with those from accelerometer measurement and preflight analysis. Since these measurements were taken in daylight, the curling phenomenon does not affect the frequency. It can be seen from the table that there is good agreement between photogrammetry data and analysis. There is also reasonable agreement with accelerometer results. Because of the high in-plane damping, the displacement was too small for the photogrammetry technique to be applied. The damping from accelerometer and photogrammetry results was comparable where data from photogrammetry were available. The maximum mast tip deflection from the 100 percent deployed out-of-plane test was determined to be 19.1 in. from photogrammetry data compared to 18.0 in. from accelerometer data. It should be noted that photogrammetry results show that the frequency increases with time, after excitation, and damping decreases with time, indicating a nonlinear system. Consequently, frequency and damping values are to be taken as average values for the total data taking time. Overall, the comparison of photogrammetry data with accelerometer data and analysis is quite close.

Table 10 shows a frequency and damping comparison of values obtained from DAE measurement with those from accelerometer measurement, and both preflight analysis and postflight analysis. Postflight analysis values incorporated the mast twist and blanket curl that were present during darkness. This accounts for the poor comparison of test results with preflight analysis. DAE data confirm the nonlinearity of frequency and damping reported from photogrammetry. In reporting frequencies and damping results for DAE, the range of values was provided rather than a single value. If one is interested in values at times of large response amplitude, then the smallest frequency value and the largest damping value are applicable. Frequencies from both the accelerometer data and DAE data do not match well with the postflight analysis results. This may mean that the model of the curled configuration is not totally accurate, or that there are other phenomena not accounted for in the analysis. The comparison of accelerometer data and DAE data is reasonably acceptable.

TABLE 9. FREQUENCY COMPARISON OF ACCELEROMETER DATA WITH PHOTOGRAMMETRY

SOLAR ARRAY DEPLOYED POSITION (PERCENT)	MODE	PREFLIGHT ANALYSIS HZ	ACCELEROMETER HZ	PHOTOGRAMMETRY HZ
70	O/P BENDING	.0594	.056	.059
70	I/P BENDING	.0671	.063	–
70	TORSION	.0765	.075	.076
70	O/P BENDING	.1191	.099	.114
70	TORSION	.1454	–	.148
70	O/P BENDING	.1961	.165	.160
100	O/P BENDING	.0345	.037	.037
100	TORSION	.0576	.058	.0576
100	O/P BENDING	.0966	.095	.098

TABLE 10. FREQUENCY AND DAMPING COMPARISON OF ACCELEROMETER DATA WITH DAE RESULTS – 70 PERCENT SOLAR ARRAY DEPLOYMENT

MODE	PREFLIGHT ANALYSIS FREQUENCY HZ	POSTFLIGHT ANALYSIS FREQUENCY HZ	ACCELEROMETER FREQUENCY HZ	DAE FREQUENCY HZ
O/P BENDING	0.0594	0.0643	.059	0.059 –0.072
I/P BENDING	0.0671	0.0671	.062	NOT IDENTIFIED
TORSION	0.0765	0.1154	.075	0.089–0.092
O/P BENDING	0.1191	0.1794	.126	.121
TORSION	0.1454	0.2136	NOT IDENTIFIED	.172

MODE	ACCELEROMETER DAMPING PERCENT	DAE DAMPING PERCENT
O/P BENDING	6	2 – 8
I/P BENDING	–	
TORSION	2.4	1 – 2
O/P BENDING	3.7	2 – 4
TORSION	–	2

e. Dynamics Summary. The solar array behaved dynamically, as predicted for out-of-plane excitation during daylight. Differences in response to in-plane excitation and darkness tests have explanations that have been substantiated by postflight tests and analyses. The on-orbit dynamic tests proved invaluable, both to the understanding of the dynamics of the solar array and to establishment of testing techniques of large space structures.

C. Solar Cell Module Performance Testing

1. Flight Data. Current-voltage data were obtained for each of the three active solar cell modules, shown in Figure 2. A current-voltage (IV) curve for the 2 cm × 4 cm module is shown in Figure 26. Actual data points (8 each) are shown as x's connected by straight lines in the plot. The smooth curve is drawn by using the Hughes Aircraft Company solar cell model (Report No. SSD 70135R) and short-circuit current (I_{sc}), open-circuit voltage (V_{oc}), maximum power point current (I_{mp}), and maximum power point voltage (V_{mp}). The maximum power point, used as an input to the Hughes model, was determined by multiplying current times voltage at each data point to obtain a "trial" maximum power; then a curve fit to this trial maximum power point and one data point on each side was performed to determine current as a function of voltage over this range of the curve. The current and voltage values for the maximum I × V value, determined from the curve fit, were then used in the model as the true I_{mp} and V_{mp}.

Some scatter is noted in Figure 26 for the data points on the short-circuit current side slope of the IV curve. This scatter existed for the 2 cm × 4 cm and 5.9 cm × 5.9 cm modules and was noticeable in plots for each module, depending upon module temperature and the resulting voltages encountered. Since the amount of scatter was larger than the 1 bit resolution of the data system, an anomaly in the data system was implied. Postflight testing at MSFC revealed that the load circuits for the 2 cm × 4 cm and 5.9 cm × 5.9 cm solar cell modules shunted a multiple of 16.6 ma around the current sensing resistors. Since the multiplying factor (1, 2, or 3) was a function of the selected load point, current corrections to the IV curve were easily implemented in computerized reduction of the data at MSFC. Figures 27, 28, and 29 illustrate corrected IV curves for each of the three modules at quasi-static stabilized temperatures. It can be noted in these Figures that the selection of load points for the 2 cm × 4 cm module was better than for the other two modules.

Plots of I_{sc} for each of the modules are shown in Figures 30, 31, and 32. The periods of higher current at the beginning and end of each plot result from sunlight reflected off Earth's atmosphere. All plots that depict module current are corrected for off-pointing errors, in addition to the shunting corrections identified above.

Open-circuit voltage plots for each of the modules are shown in Figures 33, 34, and 35. In the early part of the daylight portion of the orbit when the modules were cold, the signal conditioners for the 2 cm × 4 cm cell module and the thin cell module were saturated, and the true V_{OC} cannot be determined. This condition existed for about 1 min and is depicted by the flat portion (slope = 0) at the top of the curves.

Maximum power point voltages, at the base of the wing, for the three modules are depicted in Figures 36, 37, and 38. Figures 39, 40, and 41 illustrate the maximum power point currents. The larger scatter observed in plots for V_{mp} and I_{mp} is caused by the insensitivity of power near the maximum power point to voltage/current changes and the one bit resolution of the data system. Observation of maximum power in Figures 42, 43, and 44 shows that the larger relative transitions in V_{mp} and I_{mp} do not result in the same magnitude of transition for power when V_{mp} and I_{mp} are multiplied.

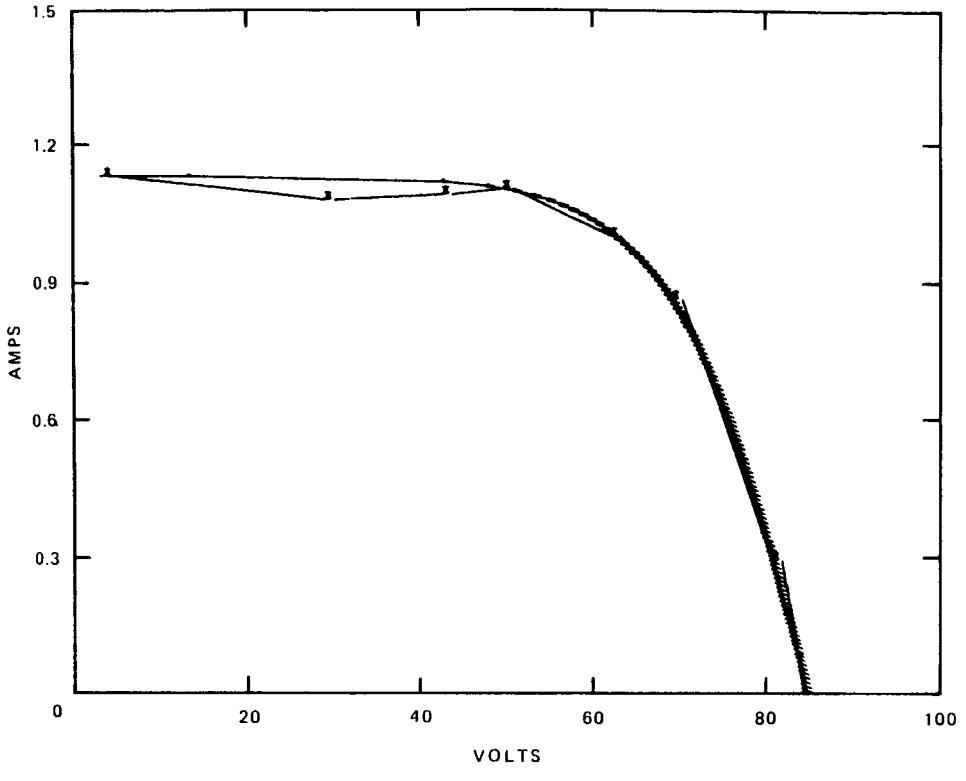

Figure 26. Solar cell module IV curve (2 cm × 4 cm cells).

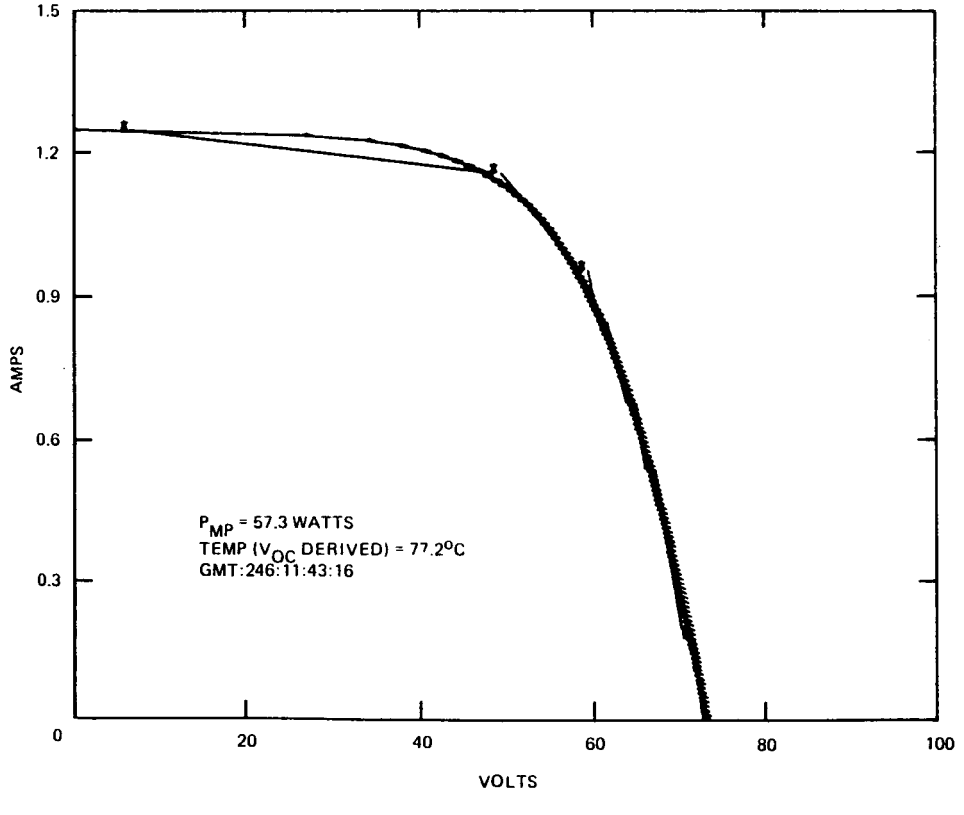

Figure 27. Solar cell module IV curve (5.9 cm × 5.9 cm cells).

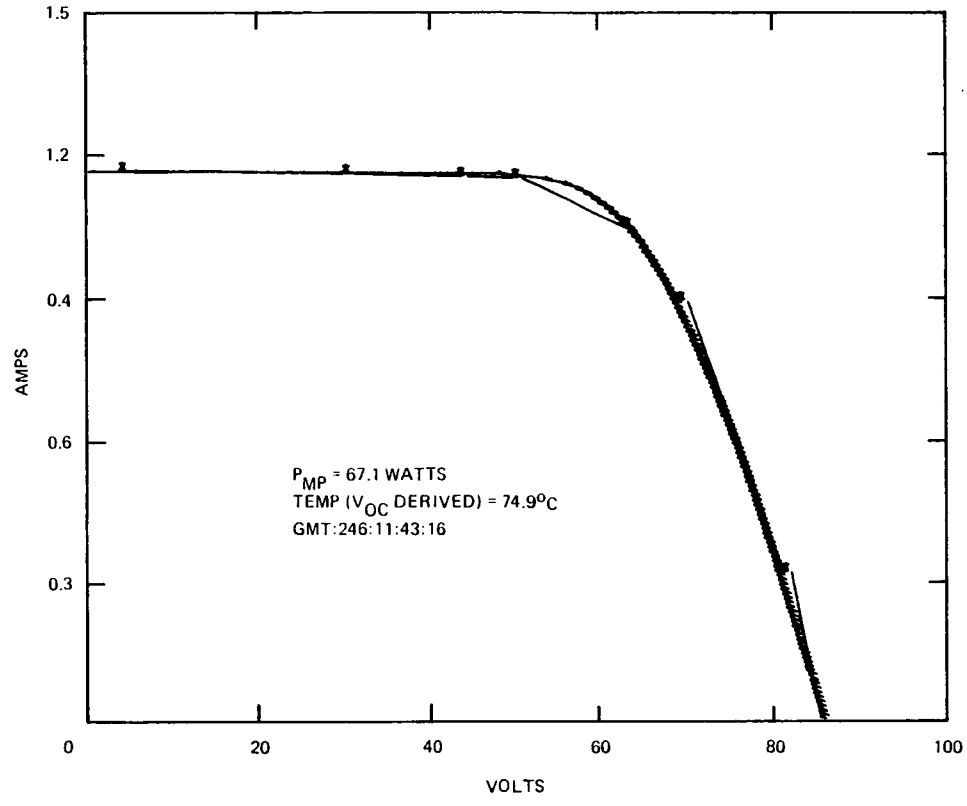

Figure 28. Solar cell module IV curve (2 cm × 4 cm cells).

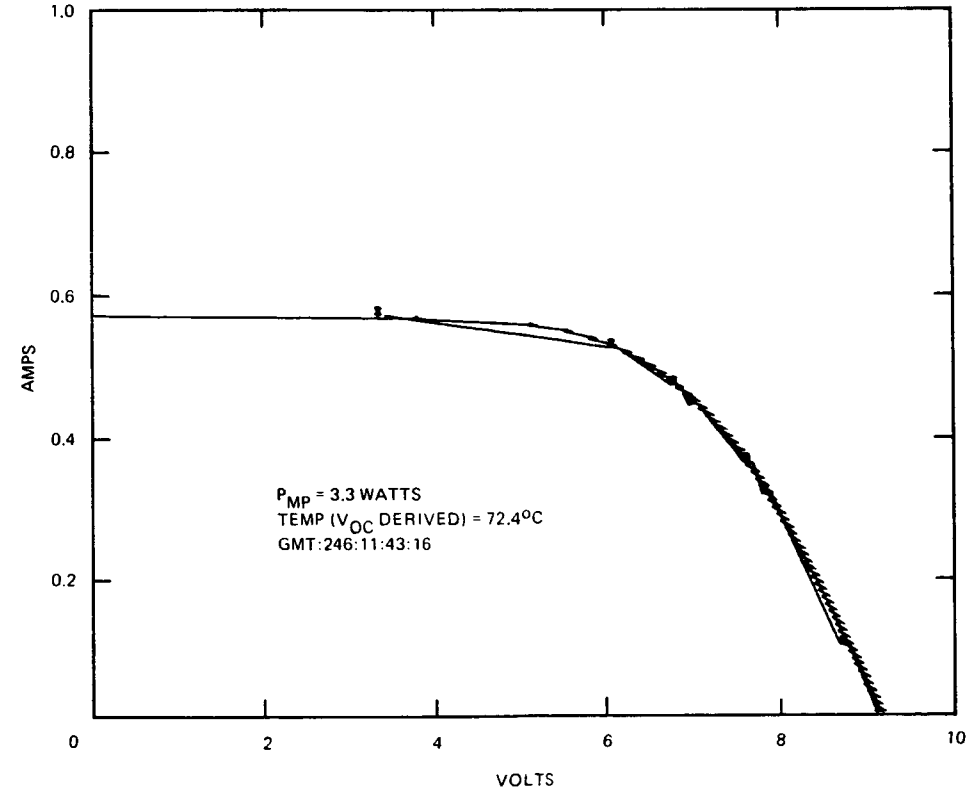

Figure 29. IV curve, thin cell module.

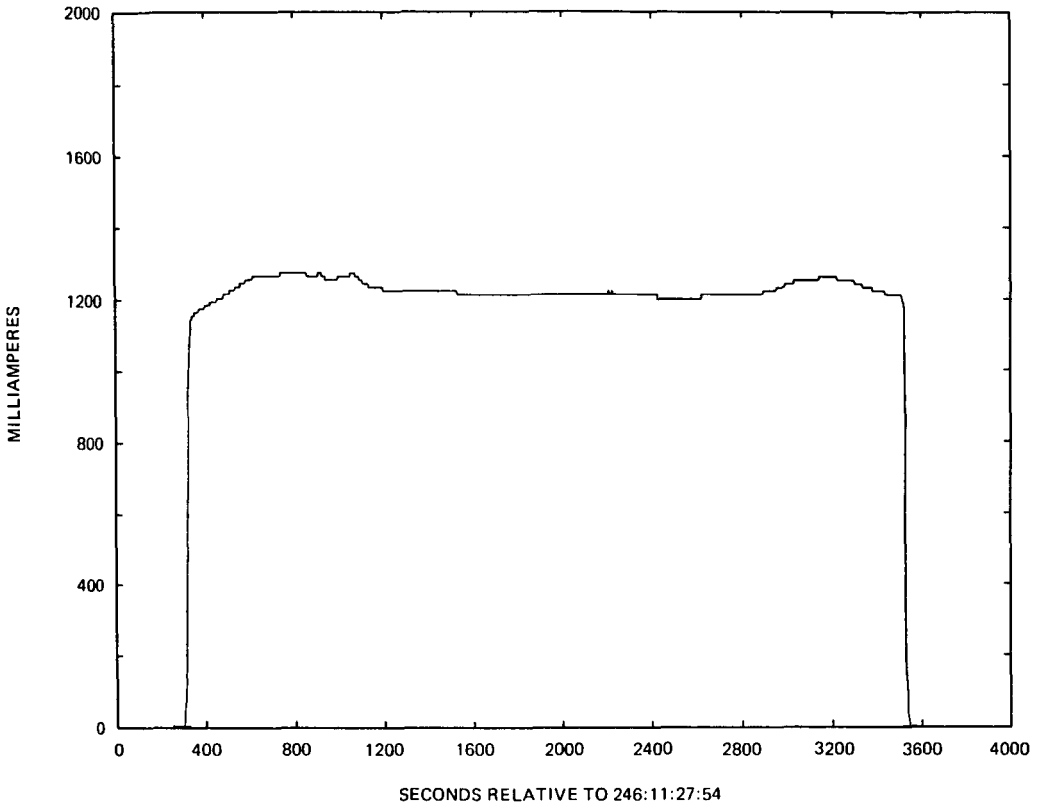

Figure 30. Solar cell module short-circuit current (5.9 cm × 5.9 cm cells).

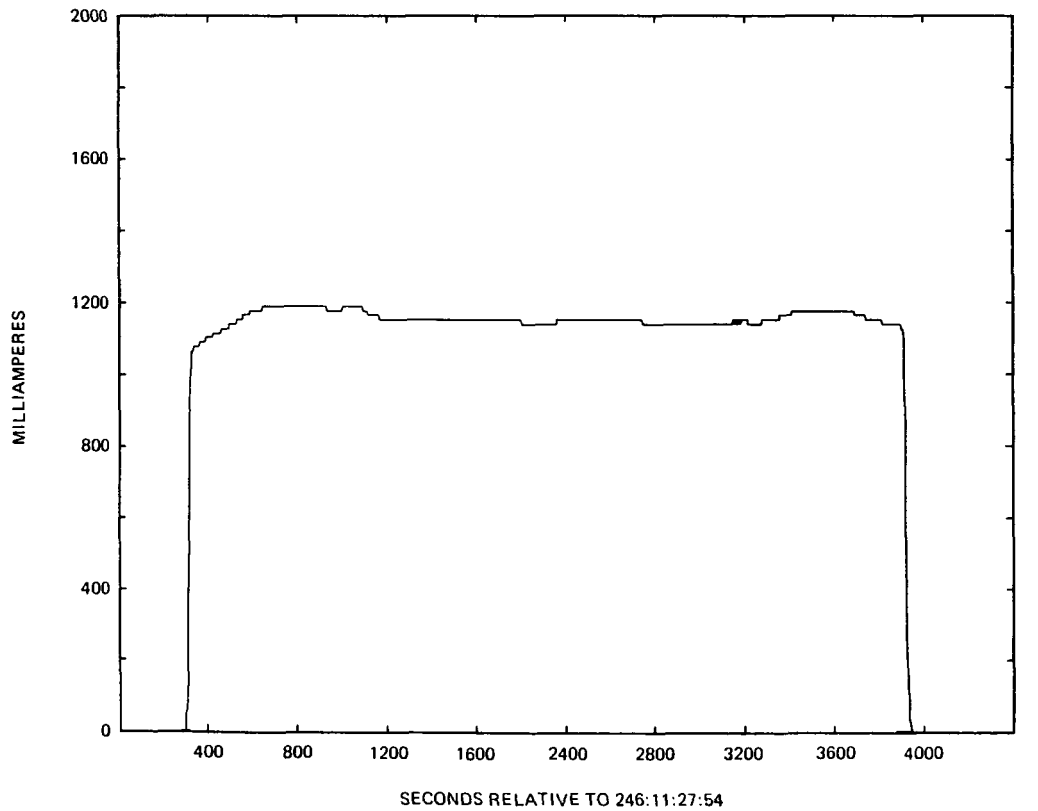

Figure 31. Solar cell module short-circuit current (2 cm × 4 cm cells).

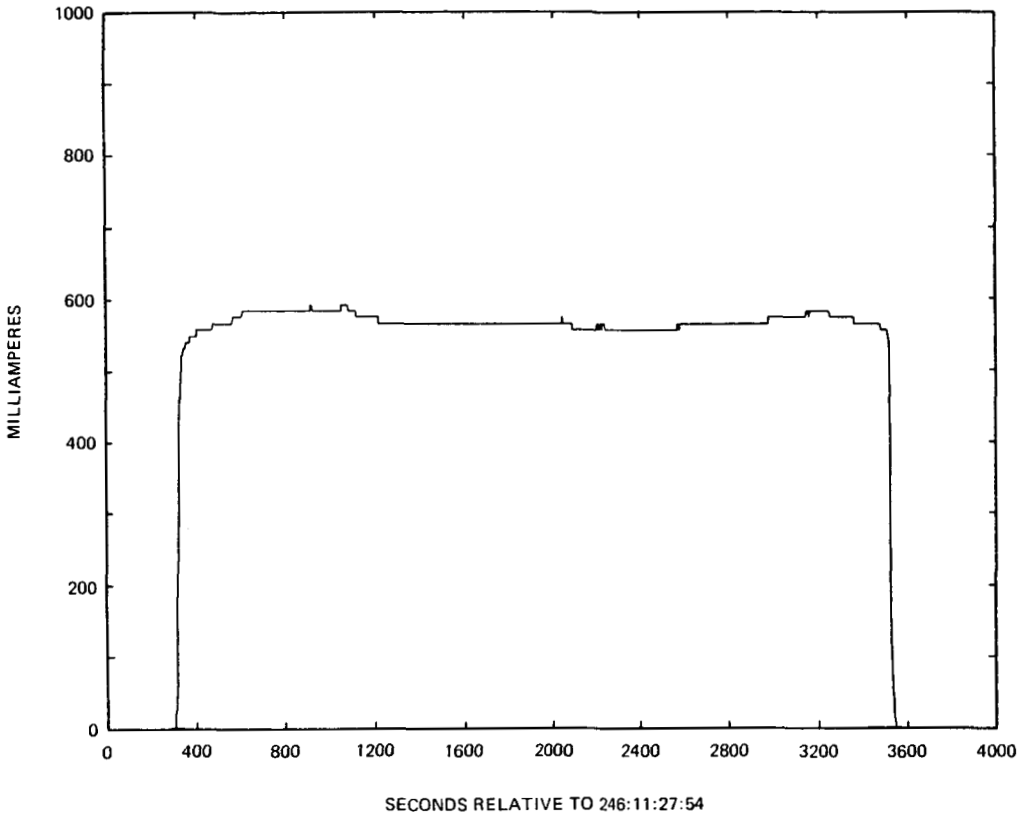

Figure 32. Thin cell module short-circuit current.

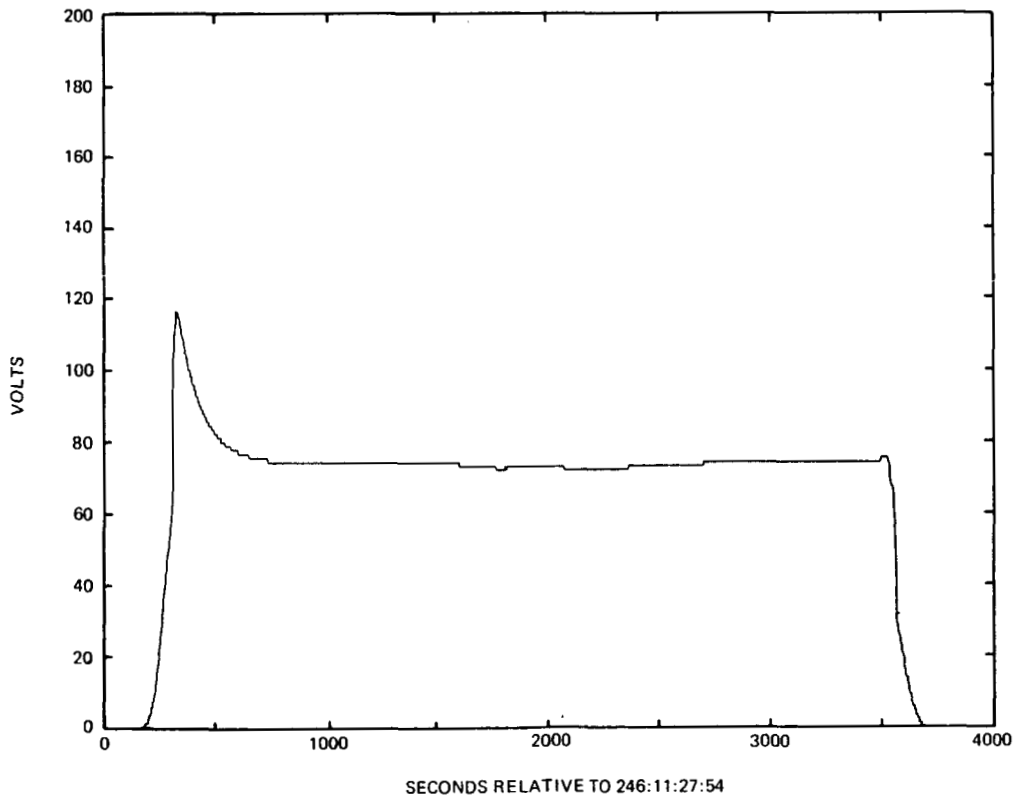

Figure 33. Solar cell module open-circuit voltage (5.9 cm × 5.9 cm cells).

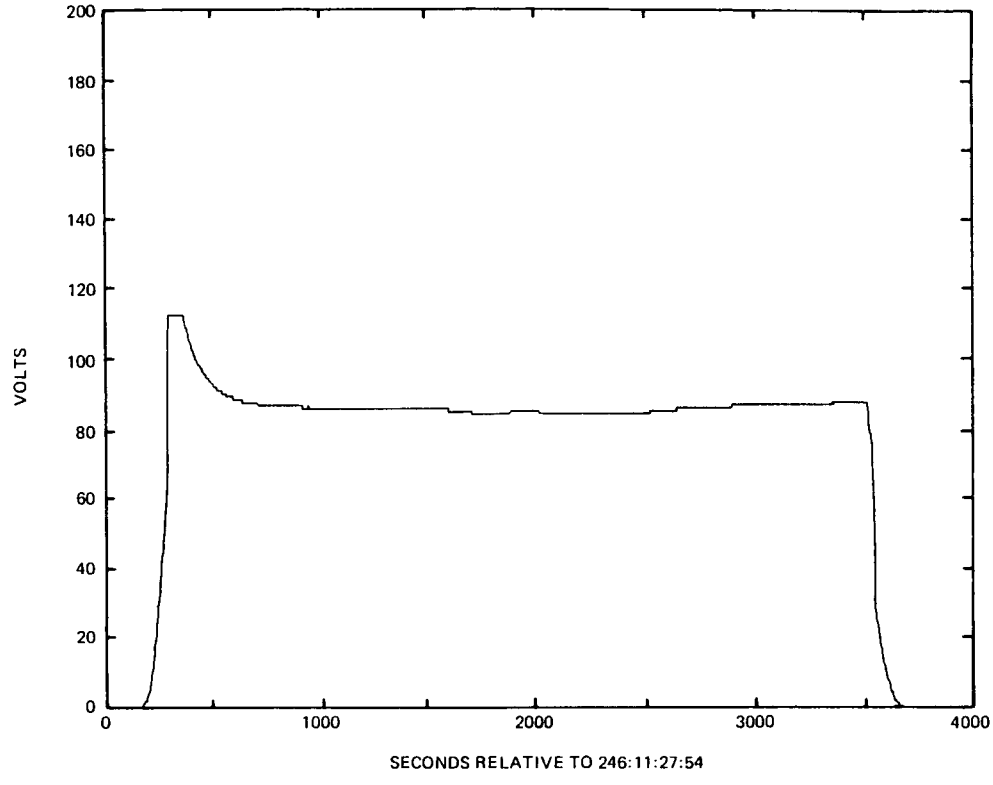

Figure 34. Solar cell module open-circuit voltage (2 cm × 4 cm cells).

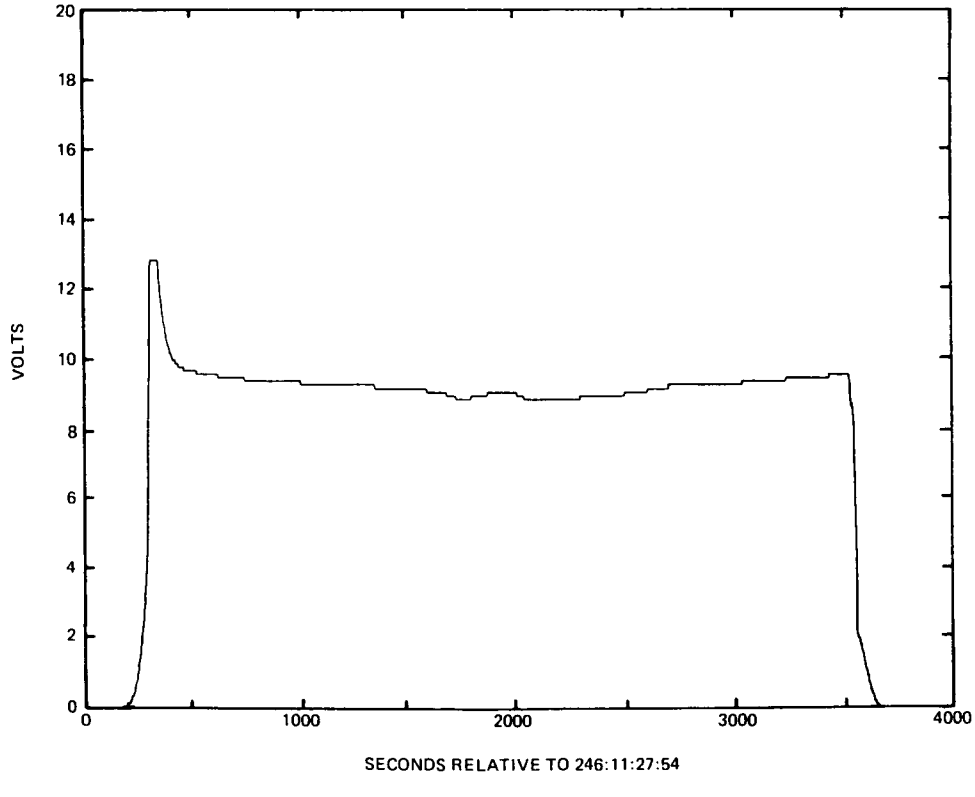

Figure 35. Thin cell module open-circuit voltage.

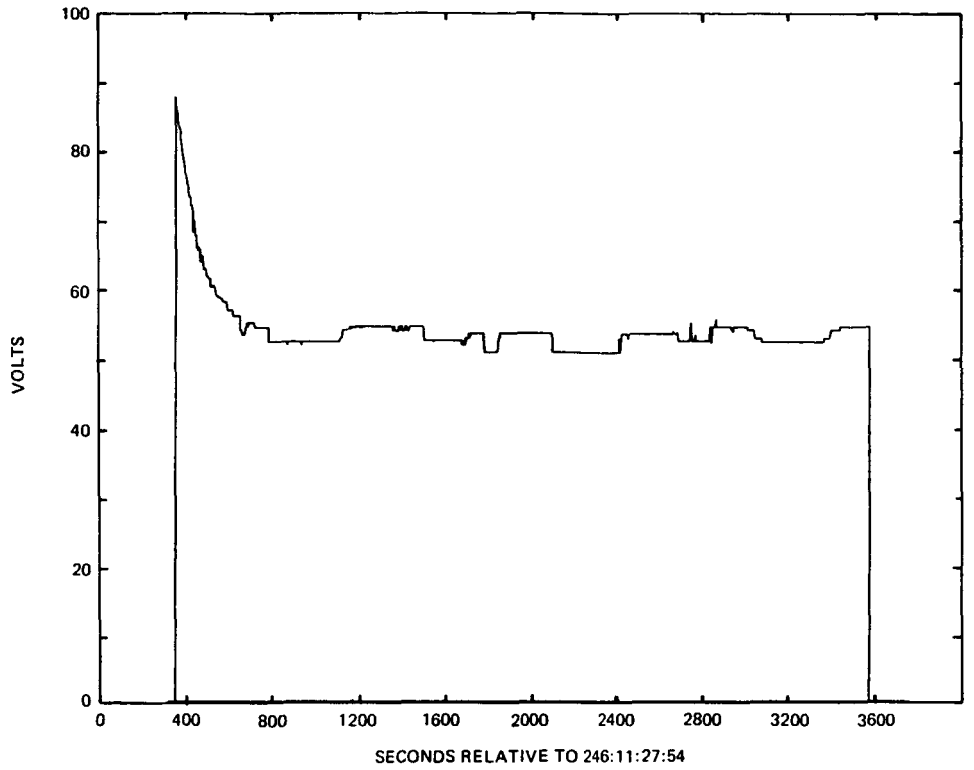

Figure 36. Solar cell module maximum power voltage (5.9 cm × 5.9 cm cells).

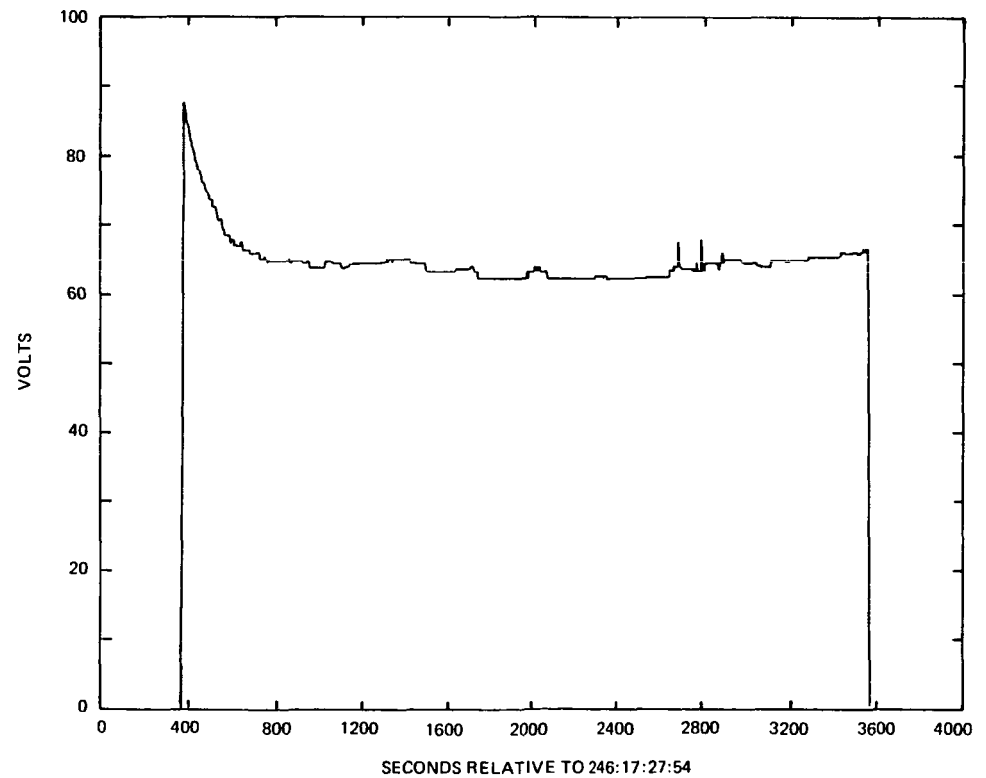

Figure 37. Solar cell module maximum power voltage (2 cm × 4 cm cells).

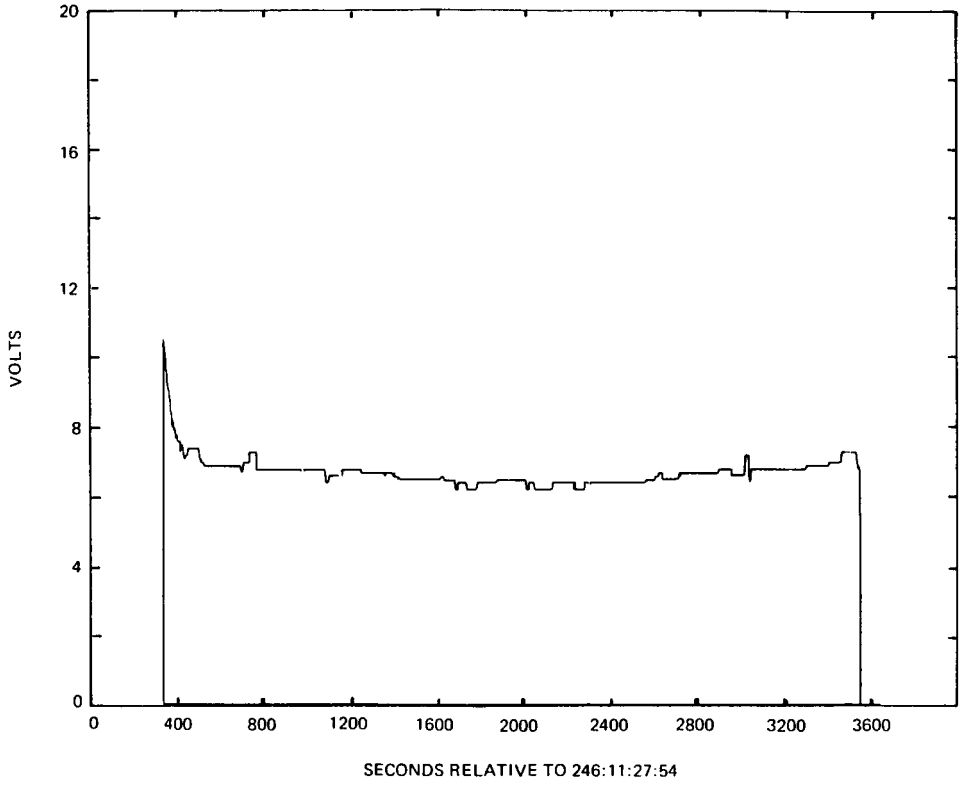

Figure 38. Thin cell module maximum power voltage.

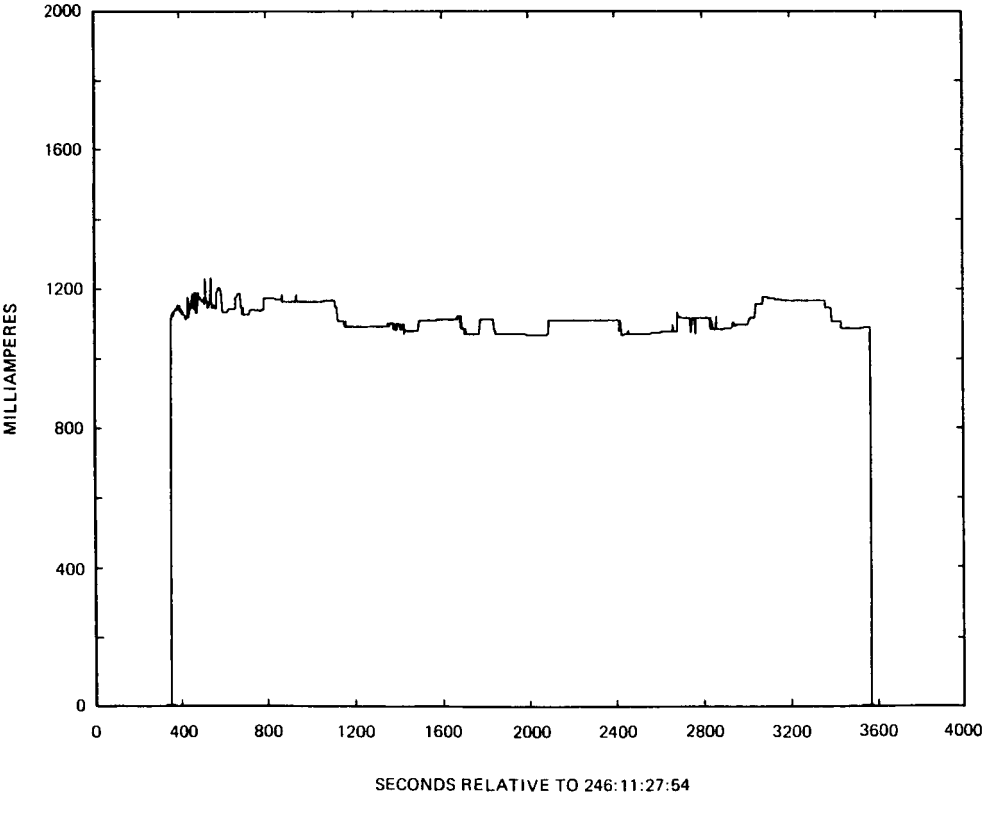

Figure 39. Solar cell module maximum power current (5.9 cm × 5.9 cm cells).

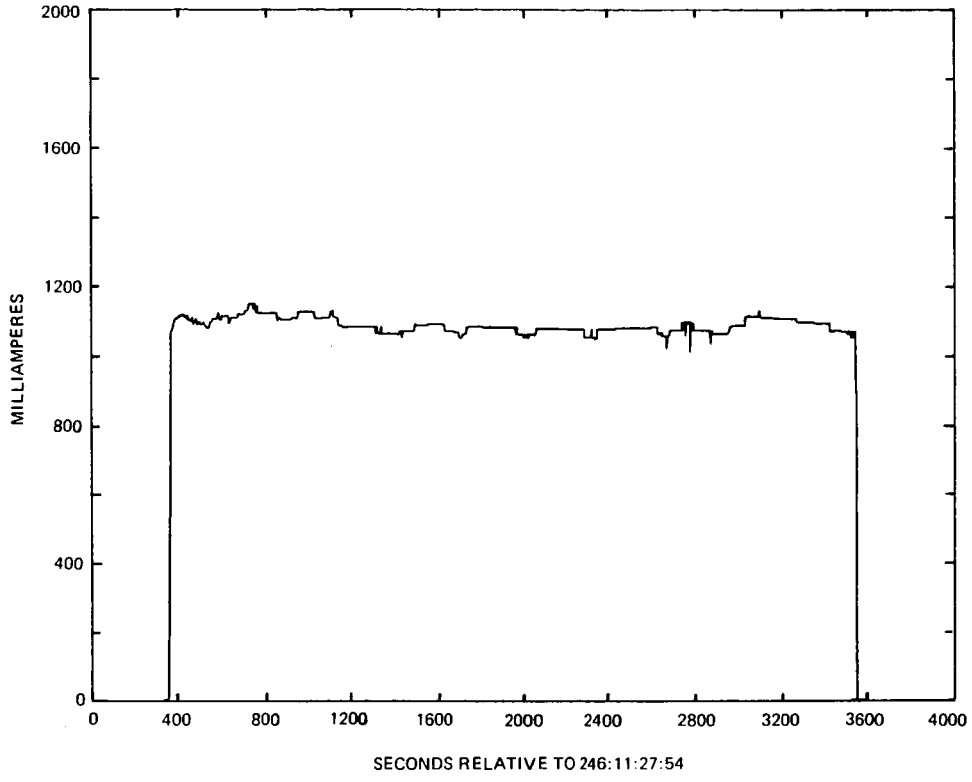

Figure 40. Solar cell module maximum power current (2 cm × 4 cm cells).

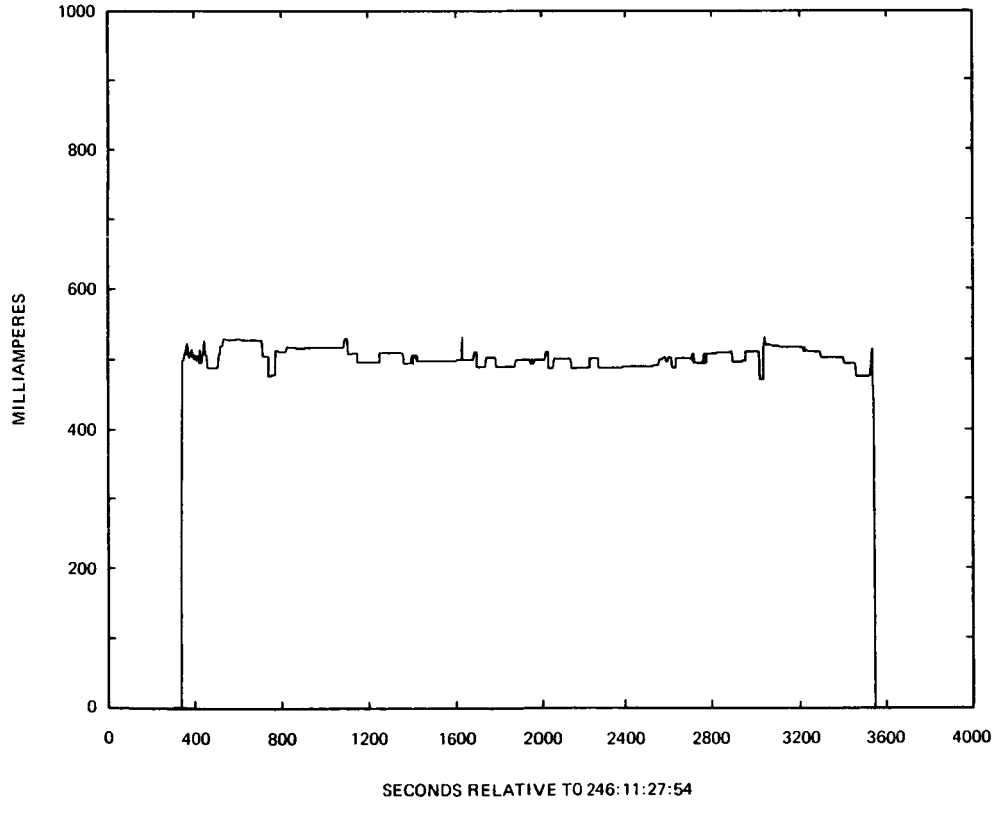

Figure 41. Thin cell module maximum power current.

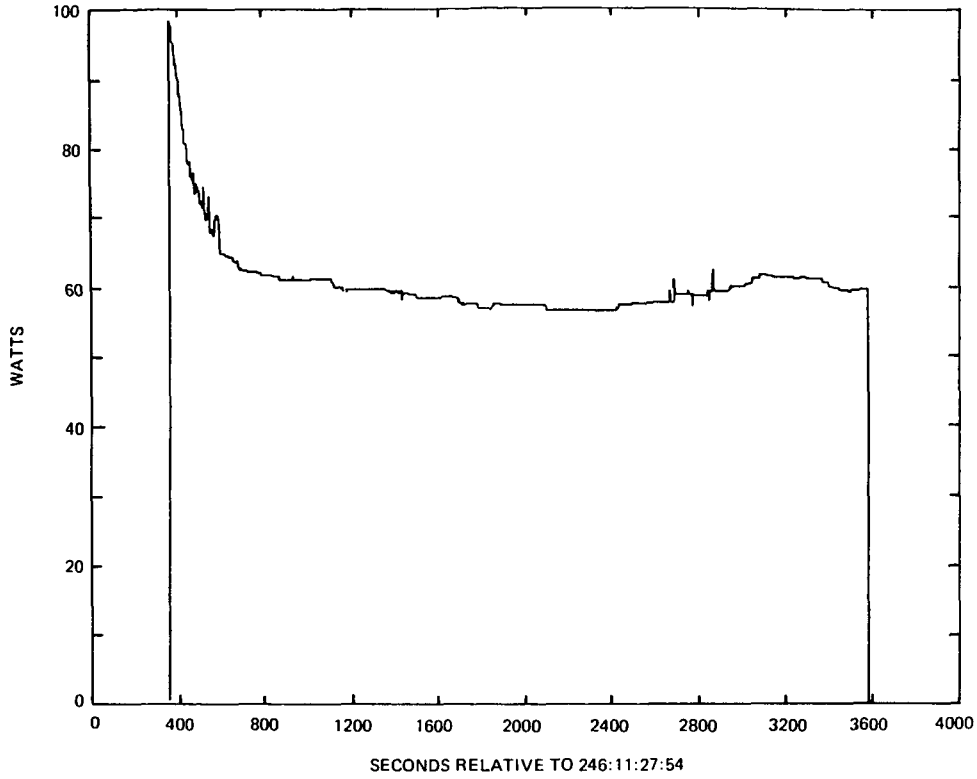

Figure 42. Solar cell module maximum power (5.9 cm × 5.9 cm cells).

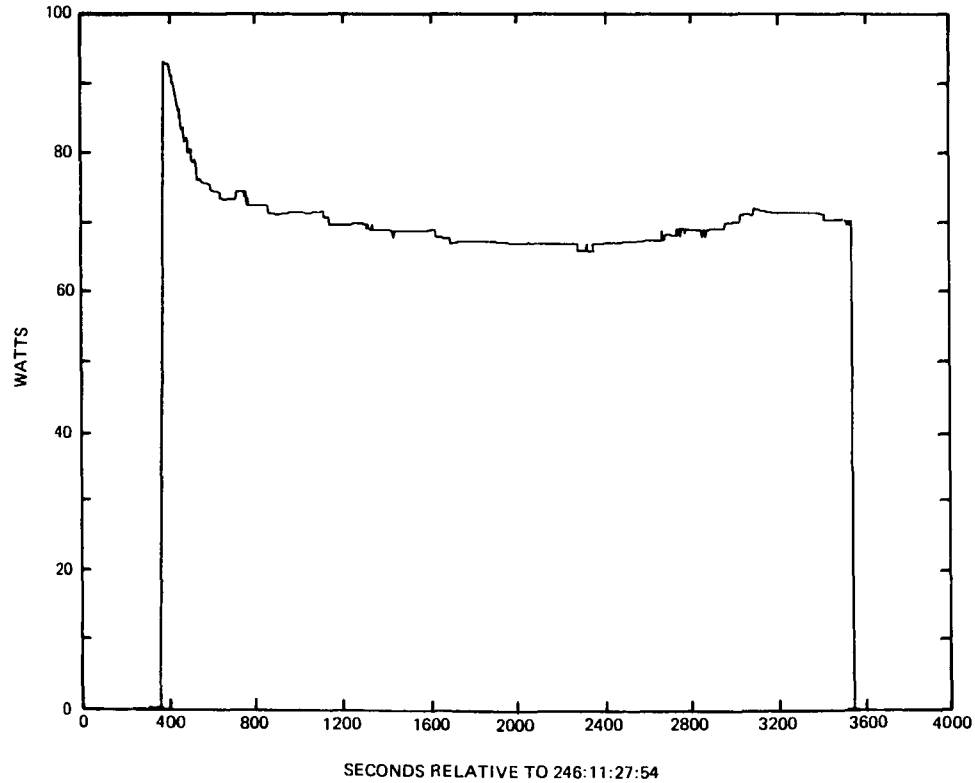

Figure 43. Solar cell module maximum power (2 cm × 4 cm cells).

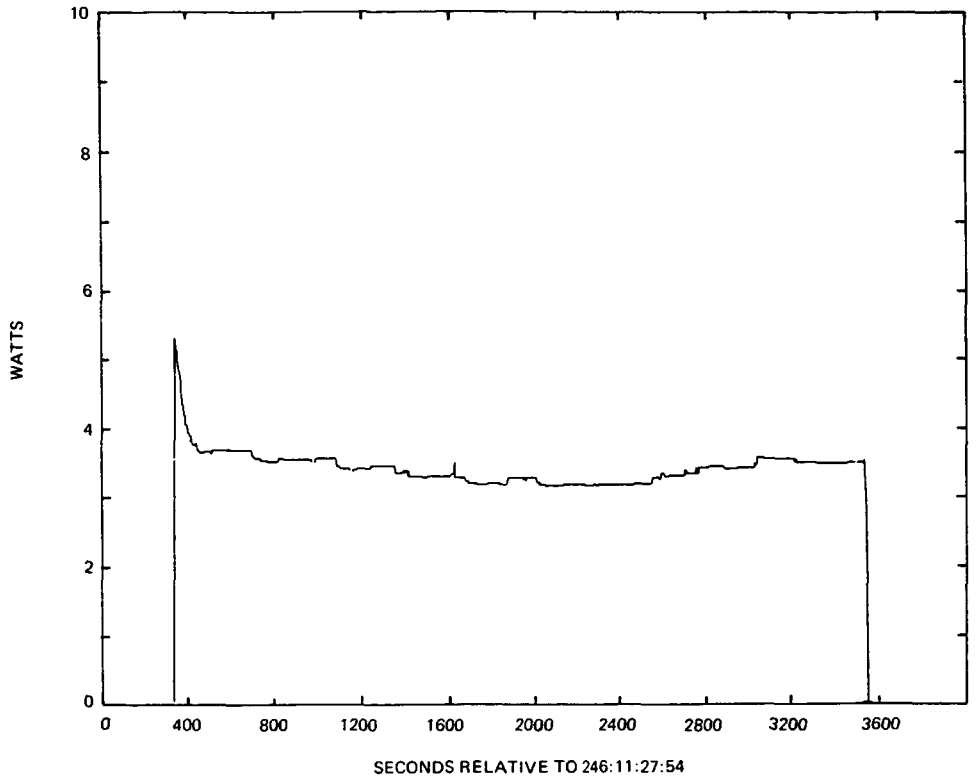

Figure 44. Thin cell module maximum power.

2. Analyses and Performance Predictions. Analyses were performed to compare actual performance in space with predicted performance, based upon laboratory measurements. Postflight flash solar simulation data, from tests conducted in the LMSC laboratories, were used as reference data for the 2 cm × 4 cm and the 5.9 cm × 5.9 cm modules. The postflight data were selected for reference because: (1) it agreed within 1 percent (for I_{sc}) with the preponderance of the preflight data (see Table 11); (2) tabular data were available from which to obtain parameter values and make interpolations; (3) ambient room temperature was accurately recorded; (4) postflight visual inspections revealed no detectable damage. Reference data for the thin cell module were taken from Reference 11. These data were used instead of LMSC data, because it was not known whether the LMSC standard solar cell used in the flash testing had a matching spectral response to the thin cell module. Slight adjustments of the ground test data for the 2 cm × 4 cm and the 5.9 cm × 5.9 cm modules were made as the result of a check of the LMSC standard cell calibration against a cell that was calibrated aboard the Solar Cell Calibration Facility (SCCF) that accompanied the SAFE on the STS-41D mission. The SCCF cell had the same essential design characteristics to produce a matching spectral response with the LMSC modules.

Actual versus predicted performance comparisons were made at the output of each module to eliminate the effect of power harness resistance changes with temperature. Changes in the resistances of the three module interconnect systems, as a result of temperature changes, were not taken into effect.

a. Laboratory data analyses. The maximum power at the 2 cm × 4 cm module and the 5.9 cm × 5.9 cm module terminals was determined by separating out the effects of harness resistance from the postflight LMSC flash simulation test data as follows:

(1) For the power range near the knee of the module IV curve, established for the base of the wing, subtract the power loss in the harness; i.e. P(module) = P(base) – I^2R where P (base) = I × V(base); R = 2.22 ohms at the room ambient temperature.

TABLE 11. LABORATORY SHORT CIRCUIT CURRENTS

	MILLIAMPERES (1)		
	5.9 cm x 5.9 cm	2 cm x 4 cm	THIN CELL (2 cm x 2 cm)
JUNE 4, 1982	1220	–	–
JUNE 7, 1982	–	1180	530
MARCH 11,1983	1220	1150	530
NOVEMBER 4, 1983	1270	–	–
NOVEMBER 8, 1983	–	1148	566
JANUARY 10, 1985 (2)	1227	1139	532

(1) MEASURED AT APPROXIMATELY 20°C EXCEPT 1985 DATA
(2) POSTFLIGHT – MEASURED AT 16°C

(2) Use the maximum value for P(module) from (1) as the maximum power at the module, with the corresponding voltage and current as the module maximum power point voltage (V_{mp}) and maximum power point current (I_{mp}), respectively.

Terminal performance data for the thin cell module were taken from Reference 11.

b. Predicted space performance. The operational performance of the modules in space was predicted from laboratory measured parameters as follows:

$$P_{mp(p)} = K_I P_{mp(m)} + K_I K_{mp} P_{mp(m)} (T_S - T_L)$$

$$V_{mp(p)} = V_{mp(m)} + K_{vmp} V_{mp(m)} (T_s - T_L)$$

$$I_{mp(p)} = K_I I_{mp(m)} + K_I K_{Imp} I_{mp(m)} (T_s - T_L)$$

$$V_{oc(p)} = V_{oc(m)} + K_{Voc} V_{oc(m)} (T_s - T_L)$$

$$I_{sc(p)} = K_I I_{sc(m)} + K_I K_{Isc} I_{sc(m)} (T_S - T_L)$$

The above symbols are defined in the List of Acronyms and Symbols. Except for K_I, parameter coefficients (K_{mp}, K_{Vmp}, K_{Imp}, etc.) are given in Table 12. Temperature coefficients for the 2 cm × 4 cm module and the 5.9 cm × 5.9 cm module were available from LMSC single cell test data. Temperature coefficients for the thin cells were determined from Reference 12. K_I (0.9954) corrects the LMSC test data for the calibration difference between the LMSC standard cell and SCCF cell. Since Reference data for the thin cell module was not LMSC test data, the value for K_I in the above equations for the thin cell module was taken as 1.0.

TABLE 12. TEMPERATURE COEFFICIENTS, PERCENT/°C

	MODULE		
COEFFICIENT	2 cm x 4 cm	5.9 cm x 5.9 cm	THIN CELL
MAX PWR. $-K_{MP}$	−0.4305	−0.4305	−0.4672
MAX PWR VOLTAGE−$K_{V_{MP}}$	−0.4191	−0.4191	−0.4641
MAX PWR CURRENT $-K_{I_{MP}}$	−0.0149	−0.0149	−0.005
OPEN CIRCUIT VOLTAGE $-K_{V_{OC}}$	−0.3427	−0.3427	−0.3914
SHORT−CIRCUIT CURRENT − $K_{I_{SC}}$	0.0364	0.0364	0.0699

c. Actual space performance. Module terminal performance in space was determined for all three modules, using the same method given in paragraph a above for determining the terminal performance of the 2 cm × 4 cm and 5.9 cm × 5.9 cm modules from laboratory test data. Harness resistance losses were subtracted from the actual space performance measured at the base of the wing. The resistances at operational temperature were determined by analyses to be 2.46 ohms and 1.23 ohms for the 2 cm × 4 cm/5.9 cm × 5.9 cm and the thin cell modules, respectively. A point in the orbit, near orbital noon, was selected for performance calculations to minimize the contribution of light reflected from Earth (Earth's albedo) upon module performance. The temperatures of the modules were near their highest values at this point, but did not differ much from average quasi-static hot temperatures. V_{oc} derived temperatures were used in this analysis because thermistor derived temperatures appeared suspect. Thermistor temperatures were typically cooler because of a heat conduction path from the thermistor to the rear surface of the cooler cell substrate. Additionally, there was a thermal lag between the cell temperature and the thermistor temperature, caused by a thermal resistance between the cell and the thermistor. The 1 bit resolution capability of the data system does however limit the accuracy of the V_{oc} derived temperatures to 2.3°C for the 2 cm × 4 cm and thin cell modules, and 3.4°C for the 5.9 cm × 5.9 cm module.

3. Actual Versus Predicted Performance. Tables 13, 14, and 15 depict the comparison of actual module performance with predicted performance. It is noted that short-circuit current predictions were pessimistic in all three cases; however, excluding a 1/2 to 1 bit inaccuracy in the data system, the accuracy achieved is probably typical of what is generally experienced because of the difficulties encountered in establishing uniform air-mass zero, 1-sun light intensities and current temperature coefficients in the laboratory. Except for the 2 cm × 4 cm module, power predictions exceeded what was achieved, i.e., 1.7 percent for the thin cell module and 2.5 percent for the 5.9 cm × 5.9 cm module. Power measured for the 2 cm × 4 cm module exceeded predictions by 1.5 percent. These deviations are within the 1 bit resolution capability of the data system at the temperature, voltage, and current of interest. Using the 5.9 cm × 5.9 cm module as an example, we have:

a. For temperature: 3.4°C (1 bit) gives 3.4°C × 0.43 percent/°C = 1.46 percent.

b. For maximum power voltage: 1.125V (1 bit) divided by 55V = 2.04 percent.

c. For maximum power current: 0.010 A (1 bit) divided by 1.11 A = 0.9 percent.

TABLE 13. SOLAR CELL MODULE ELECTRICAL PERFORMANCE (5.9 cm × 5.9 cm CELLS)

	LAB.@ 16°C		A=SPACE PREDICTION[1] @77.2°C[4]		MEASURED IN SPACE[2] @77.2°C[4]		B=K x MEASURED[3] @77.2°C[4]		RATIO[5]
PARAMETER	WING BASE	MODULE	WING BASE	MODULE	WING BASE	MODULE	WING BASE	MODULE	B/A
MAX. PWR. WATTS	82.510	85.317	–	62.839	57.282	60.189	58.313	61.272	0.975
MAX. PWR. VOLTAGE VOLTS	73.55	76.052	–	56.55	53.498	55.327	53.498	55.327	0.978
MAX. PWR CURRENT AMPS	1.122	1.122	–	1.112	1.071	1.0879	1.090	1.108	0.996
OPEN CIRCUIT VOLTAGE VOLTS	92.57	92.57	–	73.15	73.150	73.150	73.150	73.150	1.0
SHORT-CIRCUIT CURRENT AMPS	1.221	1.221	–	1.248	1.244	1.244	1.266	1.266	1.014

TABLE 14. SOLAR CELL MODULE ELECTRICAL PERFORMANCE (2 cm × 4 cm CELLS)

	LAB.@ 16°C		A=SPACE PREDICTION[1] @74.9°C[4]		MEASURED IN SPACE[2] @74.9°C[4]		B=K x MEASURED[3] @74.9°C[4]		RATIO[5]
PARAMETER	WING BASE	MODULE	WING BASE	MODULE	WING BASE	MODULE	WING BASE	MODULE	B/A
MAX. PWR. WATTS	91.412	93.9803	–	70.135	67.0743	69.9656	68.282	71.225	1.015
MAX. PWR. VOLTAGE VOLTS	85.19	87.583	–	65.949	62.084	64.360	62.084	64.360	0.976
MAX. PWR. CURRENT AMPS	1.073	1.073	–	1.064	1.080	1.087	1.099	1.107	1.040
OPEN CIRCUIT VOLTAGE VOLTS	107.13	107.13	–	85.492	85.492	85.492	85.492	85.492	1.0
SHORT-CIRCUIT CURRENT AMPS	1.136	1.136	–	1.160	1.171	1.171	1.192	1.192	1.028

TABLE 15. THIN CELL MODULE ELECTRICAL PERFORMANCE

	LAB. @ 28°C		A=SPACE PREDICTION[1] @72.4°C[4]		MEASURED IN SPACE[2] @72.4°C[4]		B= K x MEASURED[3] @72.4°C[4]		RATIO[5]
PARAMETER	WING BASE	MODULE	WING BASE	MODULE	WING BASE	MODULE	WING BASE	MODULE	B/A
MAX. PWR. WATTS	–	4.671	–	3.702	3.266	3.5747	3.325	3.639	0.983
MAX. PWR. VOLTAGE VOLTS	–	9.250	–	7.344	6.578	7.114	6.578	7.114	0.969
MAX. PWR. CURRENT AMPS	–	0.505	–	0.504	0.4965	0.5024	0.505	0.511	1.014
OPEN CIRCUIT VOLTAGE VOLTS	–	11.210	–	9.262	9.262	9.262	9.262	9.262	1.0
SHORT-CIRCUIT CURRENT AMPS	–	0.545	–	0.562	0.5636	0.5636	0.574	0.574	1.021

NOTES:
(1) SOLAR INTENSITY = 135.3 mw/cm^2
(2) SOLAR INTENSITY AT TIME OF FLIGHT (1ST WEEK OF SEPTEMBER) = 132.9 mw/cm^2
(3) K=CORRECTION FACTOR TO 1 SOLAR CONSTANT = 135.3/132.9
(4) FLIGHT TEMPERATURE AS DERIVED FROM V_{OC} MEASUREMENT
(5) RATIO PERFORMED USING MODULE VALUES

Summing the possible 1 bit inaccuracies, we could have a total inaccuracy of 4.4 percent. Based on the data system design, gain and scaling factor inaccuracies are approximately 0.5 percent. Since, on the average, the data system inaccuracy should be less than 1/2 bit, the average system error for the 5.9 cm × 5.9 cm module should be no worse than 4.4 percent divided by 2 + 0.5 percent = 2.7 percent. A similar value would also be determined for the 2 cm × 4 cm and thin cell modules if the same assessment were made for them. Comparing the data system inaccuracy with the differences between predicted performance and actual performance, it can be said that performance predictions were good. This statement is based upon predictions being made at measured space temperatures; but for the 2 cm × 4 cm and 5.9 cm × 5.9 cm modules, V_{oc} derived temperatures agree with the LMSC predicted temperatures within 1°C at the point where module performance predictions were made (Figs. 45, 46, and 47). The accuracies achieved in the predictions also imply that ground test data and temperature coefficients (Table 12) were good.

4. Performance Comparison Between Modules. An interesting comparison to make between modules is degradation in power performance from a given laboratory test condition to a selected point/condition in orbit. The laboratory test condition was 1 sun, air-mass zero at 28°C. This requires that maximum power from lab tests for the 2 cm × 4 cm and the 5.9 cm × 5.9 cm modules be corrected for differences incurred between 16°C and 28°C. Using the temperature coefficients from Table 12 and laboratory power performance from Tables 13, 14, and 15, the following comparison is made:

Module	Lab Power (Watts) at 28°C	Space Power (Watts) (1 Sun, AM0)	Degradation (%)
2 cm × 4 cm	89.125	71.225	20.1
5.9 cm × 5.9 cm	80.910	61.272	24.3
Thin Cell	4.671	3.639	22.1

Disregarding temperature differences, the degradation in performance for the 2 cm × 4 cm and 5.9 cm × 5.9 cm modules should be the same. However, the 5.9 cm × 5.9 cm module operates at a higher temperature (2.3°C measured/3°C predicted) than the 2 cm × 4 cm module, accounting for about 1.1 percent of the difference. The remaining difference (3.1 percent) could be accounted for by 1 or more of the following conditions:

a) Flight data system inaccuracies.

b) Fewer points near the knee of the IV curve for the 5.9 cm × 5.9 cm module makes it more difficult to accurately establish the maximum power point. Visual observation of the IV curves (Figs. 27, 28, and 29) for the three modules indicates that the analytical model, used to establish the curves, fits the actual data better on the 2 cm × 4 cm and thin cell modules than the 5.9 cm × 5.9 cm module. It can be noticed for the latter module that for a given current near the knee of the IV curve, model predicted voltage lies below the actual voltage. This condition certainly accounts for part of the difference between the 2 cm × 4 cm and 5.9 cm × 5.9 cm performances.

c) Inaccuracies in laboratory measurements.

d) Actual electrical performance differences.

Assuming the data system accurately measured the power, 0.55 percent of the difference in degradation between the thin cell module and the 2 cm × 4 cm module can be accounted for by the higher temperature coefficient for the thin cell module.

Taking these considerations into account, it can be stated that performance in space was reduced from that measured in the laboratory by a similar amount for the three modules.

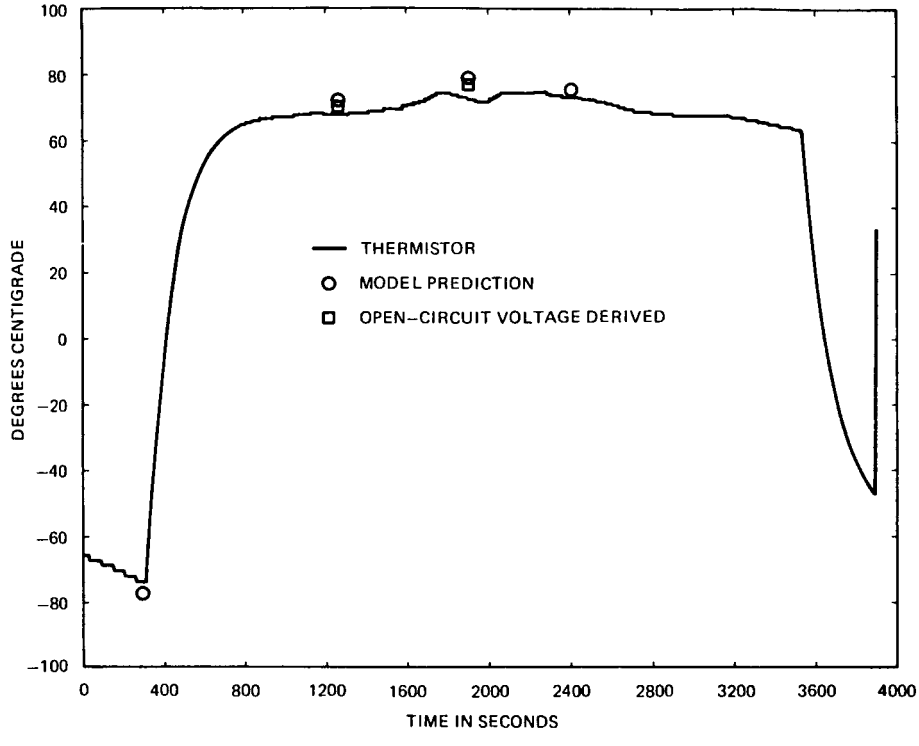

Figure 45. Solar cell module cell temperature (5.9 cm × 5.9 cm cells).

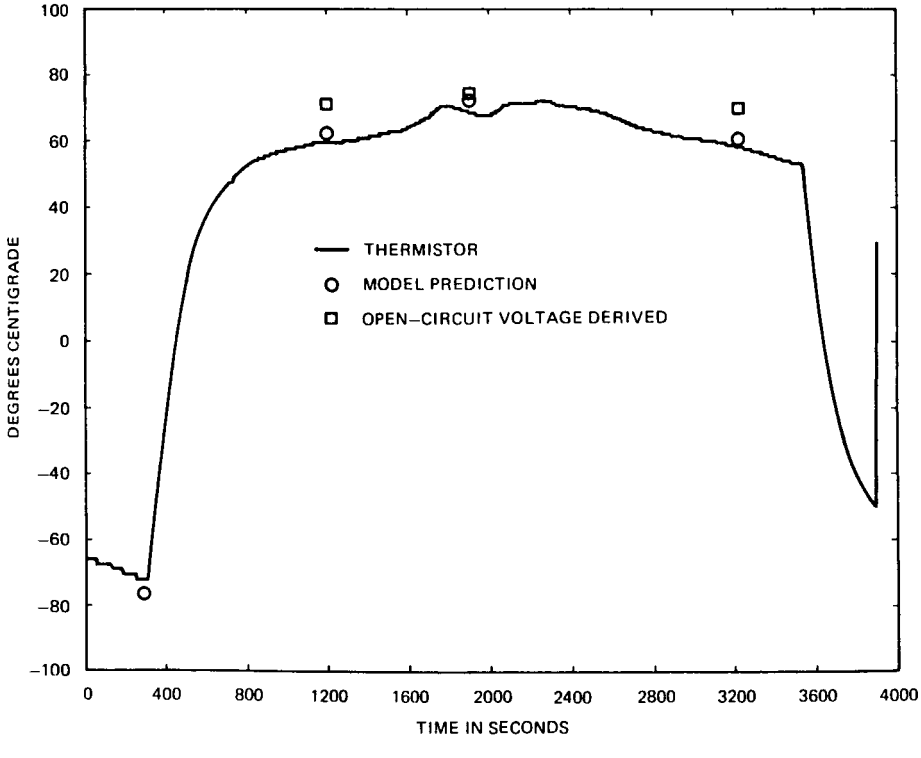

Figure 46. Solar cell module cell temperature (2 cm × 4 cm cells).

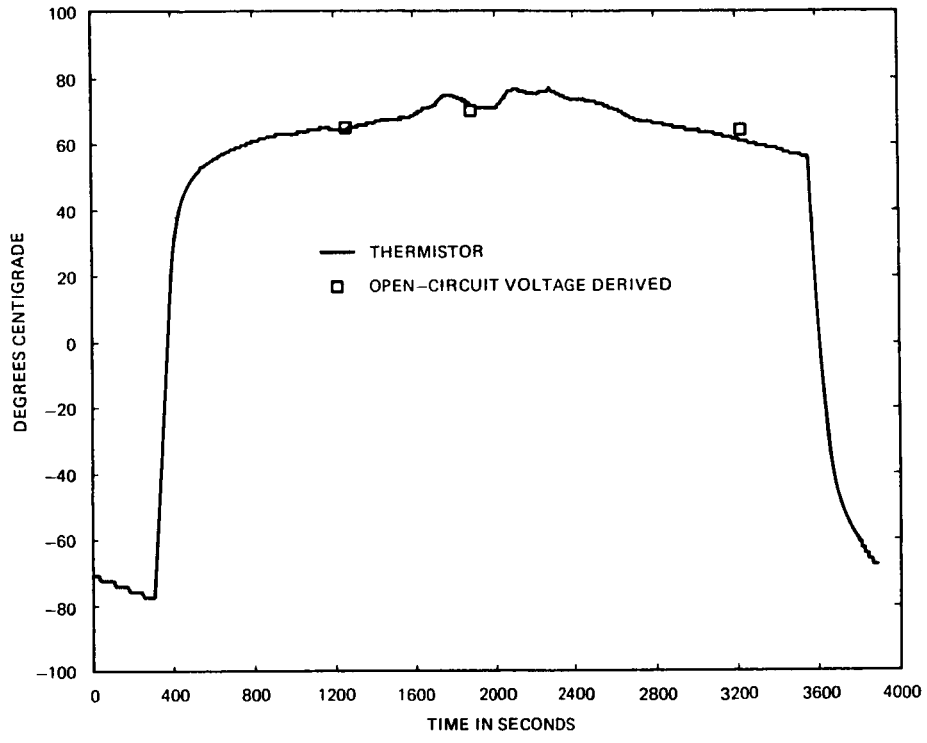

Figure 47. Thin cell module substrate rear surface temperature.

5. Degradation Resulting from Extension/Retraction Operations. Another objective of the experiment was to determine if degradation in electrical performance of the modules would occur as a result of extension/retraction operations. A second performance test (Event 24 in Table 3) was performed after extend to 100 percent, retract fully, extend to 70 percent, retract fully, and extend to 70 percent operations were performed. A point in the second test was selected where the open-circuit voltages and short-circuit currents were as close as could be found to the earlier condition. This ensured that temperatures and intensity conditions were sufficiently alike to make good comparisons. If degradation in module current-voltage performance occurred under these conditions, it would be manifested in a "drooping" IV curve, typical of increased module series resistance. Open-circuit voltage and short-circuit current conditions were found for all three modules that were equivalent to those analyzed in the first performance test. Compare Figures 48, 49, and 50 with Figures 27, 28, and 29. Table 16 compares module performances between the two tests. Module performance at the base of the wing was the basis for this comparison. The data given in Table 16 indicate that module performance was not degraded by extension/retraction operations. This is further verified by postflight visual inspections and tests that revealed no detectable damage to either of the modules.

6. Electrical Performance from Earth's Albedo. Eight dynamics tests were conducted with the orbiter in a gravity gradient mode and the active side of the array blanket facing Earth. These tests were conducted about orbital noon, each taking about 5 min. Since the SAFE tape recorder was on for each of these tests, solar cell module performance data were obtained in addition to accelerometer dynamics data. Short-circuit current for each of the modules was analyzed to obtain data for use in future studies of the effect of Earth's albedo on power output. Table 17 summarizes the results of this analysis. The lower performance exhibited by the thin cell module is caused by its location on the most outboard panel of the blanket. In this location, the thin cell module does not have as large a view factor of Earth's surface as the other two modules.

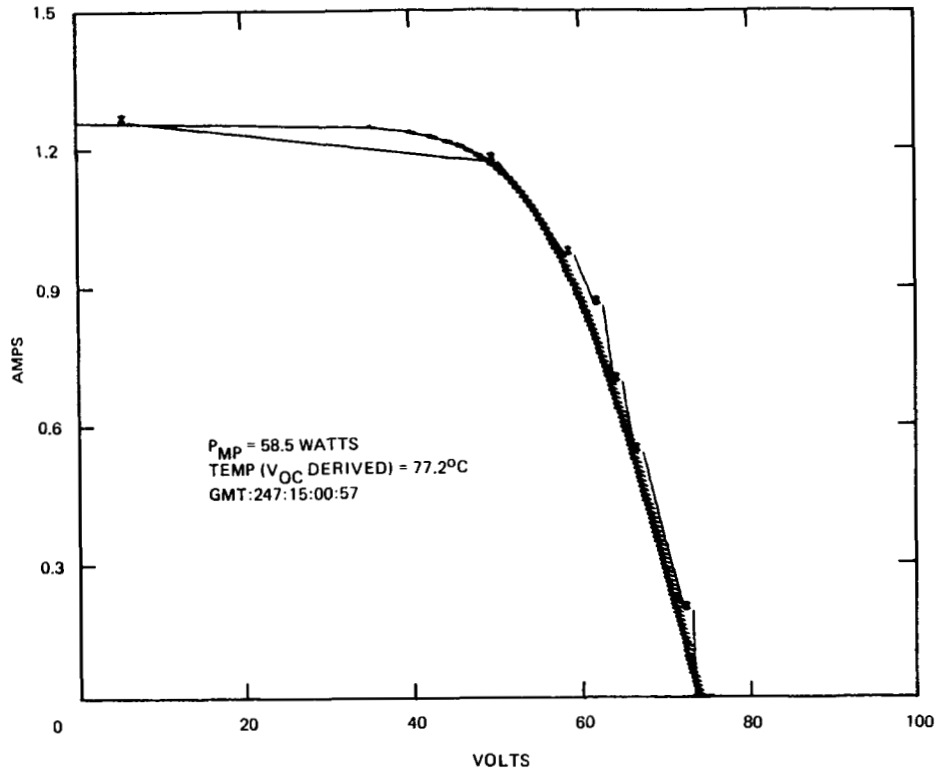

Figure 48. Solar cell module IV curve, second performance test (5.9 cm × 5.9 cm cells).

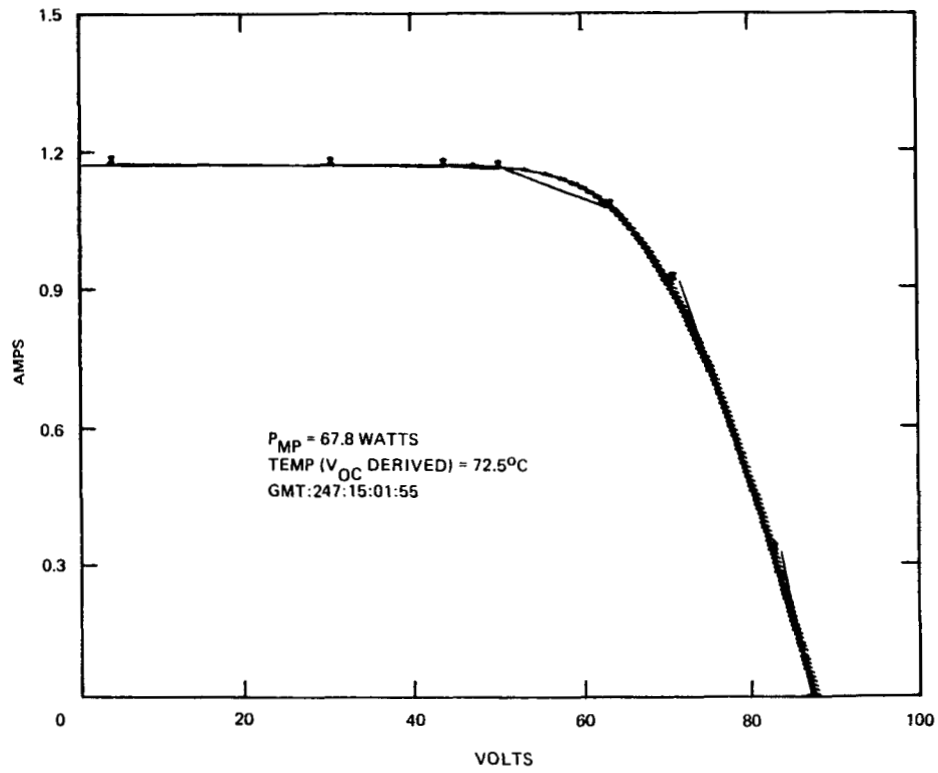

Figure 49. Solar cell module IV curve, second performance test (2 cm × 4 cm cells).

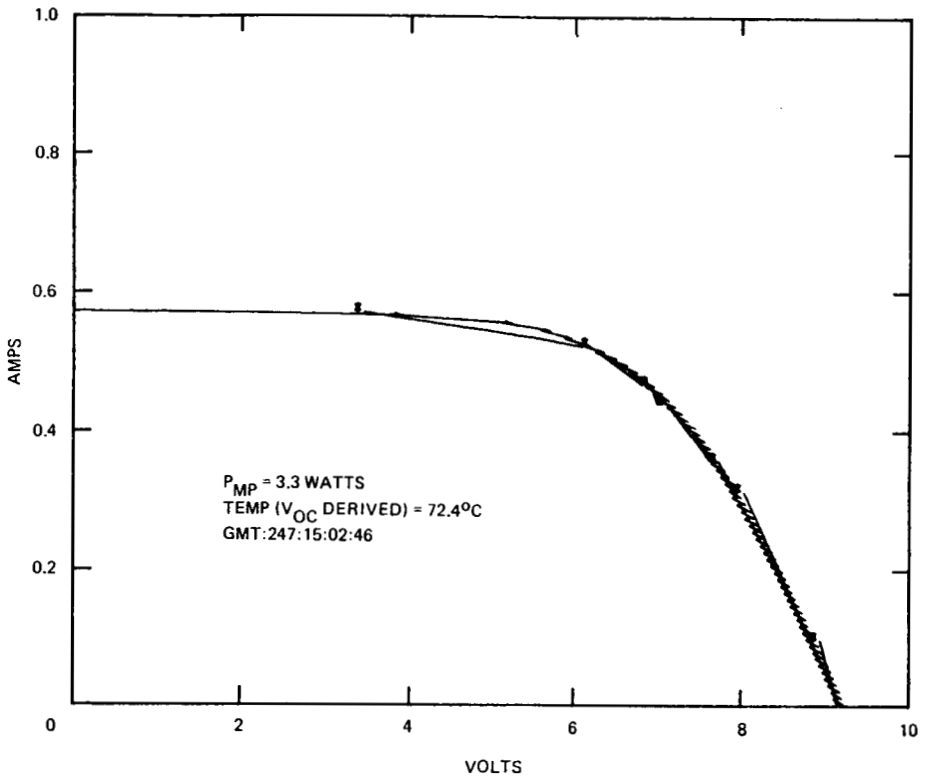

Figure 50. IV curve, thin cell module, second performance test.

TABLE 16. SOLAR CELL MODULE PERFORMANCE COMPARISON BEFORE AND AFTER EXTENSION/RETRACTION OPERATIONS

	POWER (WATTS)		
MODULE / TEMPERATURE*	FIRST PERFORMANCE TEST	SECOND PERFORMANCE TEST	Δ%
5.9 cm x 5.9 cm / 77.2°C	57.282	57.617	+0.6
2 cm x 4 cm / 74.9°C	67.074	67.148	+0.11
THIN CELL / 72.4°C	3.267	3.267	0

*MEASURED TEMPERATURE OF FIRST TEST: POWER MEASURED IN SECOND TEST NORMALIZED TO SAME TEMPERATURE. DIFFERENCE LESS THAN 3°.

TABLE 17. I_{SC} PERFORMANCE FROM EARTH'S ALBEDO, NEAR ORBITAL NOON

	PERCENT OF DIRECT SUNLIGHT CAPABILITY		
	2 cm x 4cm MODULE	5.9 cm x 5.9 cm MODULE	THIN CELL MODULE
HIGHEST I_{SC}	47.7	46.9	41.0
LOWEST I_{SC}	6.7	8.0	4.8
AVERAGE I_{SC}	21.0	21.0	16.7

VI. CONCLUSIONS AND RECOMMENDATIONS

The Solar Array Flight Experiment/Dynamic Augmentation Experiment was successfully tested during the Shuttle STS-41D mission and all objectives were met. As a result of flight data analyses, the following conclusions can be stated.

a) The unfold/fold method of deploying/retracting large flexible, lightweight solar arrays works well in outer space. The SAFE demonstrated the method to be tolerant of off-nominal operational conditions when the array was successfully deployed and retracted under conditions of blanket curl and panel oscillations. These conditions are anomalous to array operations and can be eliminated through proper design and testing.

b) Analyses of dynamic test data show that the array was well behaved dynamically with frequencies being close to predictions. Motion decayed quickly after completion of excitation inputs, which means that the array had desirably high damping values. These results are verified by all three means of measuring dynamic performance: i.e., accelerometers, photogrammetry, and the Dynamic Augmentation Experiment.

c) Measured space electrical and thermal performance of the solar cell modules were close to predictions. Comparison of preflight, flight, and postflight test results indicates that module performance was not degraded by launch, space extension/retraction and dynamics testing, or reentry environments.

d) Both CCTV photogrammetry and the Dynamic Augmentation Experiment were used to remotely measure solar array dynamic characteristics. The results show both techniques are capable of measuring dynamic responses of large, low frequency structures which cannot be adequately instrumented with accelerometers.

Recommendations that can be made as a result of the SAFE/DAE program are as follows:

a) During future developments of flexible, lightweight solar array blankets for space application, (1) conduct thermal-vacuum tests to characterize the susceptibiilty of the blanket to curl in its operational environment; (2) develop a mast design that will not act as an excitation force for the natural frequencies of oscillation of the deploying/retracting array.

b) Perform the work necessary to make flexible, lightweight solar arrays resistant to atomic oxygen interactions.

c) Digital data acquisitions systems in future experiments should utilize at least a 10 bit word to improve data accuracy and ease data analyses.

d) Exercise extreme care in performing solar simulation testing of solar array electrical modules to minimize the data scatter inherent therein.

REFERENCES

1. Lockheed Missiles and Space Co.: Solar Array Flight Experiment Final Report. Marshall Space Flight Center, Contract NAS8-31352, Report No. LMSC-F087173, April 1986.

2. Brumfield, M. Larry, Pappa, Richard S., Miller, James B., and Adams, Richard R.: Orbital Dynamics of the OAST-1 Solar Array Using Video Measurements. AIAA/ASME/ASCE/AHS 26th Structures, Structural Dynamics, and Materials Conference, Orlando, FL, April 15-17, 1985, AIAA Paper No. 85-0758-CP.

3. Slaby, Jerry: Solar Array Flight Experiment. NASA TM-86506, April 1985.

4. Slaby, Jerry: Evaluation of Solar Array Flight Experiment Response During Flight for Extension/Retraction Phase. NASA TM-86551, June 1986.

5. David, Sidney S., Fay, Stanley, Kirchwey, Christopher B., Sackett, Lester L., and Satter, Celeste M.: Space Shuttle On-Orbit Flight Control System/OAST-1 Payload Dynamic Interaction Study. The Charles Stark Draper Laboratory, Inc., CSDL-R-1596, February 1983.

6. Muller, Gary: Post Flight Additional Parametric Studies of Solar Array Flight Experiment (SAFE). MSFC Memorandum ED22-85-110, May 24, 1985.

7. Venator, T.: Updated Solar Array Flight Experiment Models. Lockheed Missiles and Space Company, SD/R-536, April 5, 1983.

8. Pinson, Earl: Discrete Mechanism Damping Effects in the Solar Array Flight Experiment. 20th Aerospace Mechanisms Conference, Cleveland, OH, May 7-9, 1986, NASA Conference Publication 2423.

9. Juang, Jer-Nan, and Pappa, Richard S.: An Eigensystem Realization Algorithm (ERA) for Modal Parameter Identification. JPL Workshops on Identification of Flexible Space Structures, San Diego, CA, June 1984.

10. Schock, Richard W.: Solar Array Flight Dynamics Experiment. NASA TP-2598, May 1986.

11. TRW "Final Report on High Temperature – Low Mass Solar Blanket." JPL Contract No. 955139, TRW No. 32809.00, August 1979.

12. Anspaugh, B. E., Beckert, D. M., Downing, R. G., Miyahira, T. F., and Weiss, R. S.: Characterization of Solar Cells for Space Applications, Volume XII. Electrical Characteristics of Solarex BSF, 2-Ohm-cm, 50-Micron Solar Cells (1978 Pilot Line) as a Function of Intensity, Temperature, and Irradiation, JPL Publication 78-15, Volume XII, March 1, 1980.

1. REPORT NO.	2. GOVERNMENT ACCESSION NO.	3. RECIPIENT'S CATALOG NO.
NASA TP-2690		

4. TITLE AND SUBTITLE	5. REPORT DATE
Solar Array Flight Experiment/ Dynamic Augmentation Experiment	February 1987
	6. PERFORMING ORGANIZATION CODE
7. AUTHOR(S) Leighton E. Young and Homer C. Pack, Jr.	8. PERFORMING ORGANIZATION REPORT
9. PERFORMING ORGANIZATION NAME AND ADDRESS George C. Marshall Space Flight Center Marshall Space Flight Center, Alabama 35812	10. WORK UNIT NO. M-545
	11. CONTRACT OR GRANT NO.
	13. TYPE OF REPORT & PERIOD COVERED Technical Paper
12. SPONSORING AGENCY NAME AND ADDRESS National Aeronautics and Space Administration Washington, D.C. 20546	14. SPONSORING AGENCY CODE

15. SUPPLEMENTARY NOTES

Prepared by the Information and Electronic Systems Laboratory and the Systems Dynamics Laboratory, Science and Engineering Directorate.

16. ABSTRACT

This report presents the objectives, design, testing, and data analyses of the Solar Array Flight Experiment/ Dynamic Augmentation Experiment (SAFE/DAE) that was tested aboard Shuttle in September 1984. The SAFE was a lightweight, flat-fold solar array that employed a thin polyimide film (Kapton) as a substrate for the solar cells. Extension/retraction, dynamics, electrical and thermal tests, were performed. Of particular interest is the dynamic behavior of such a large lightweight structure in space. Three techniques for measuring and analyzing this behavior were employed. The methodology for performing these tests, gathering data, and data analyses are presented.

The report shows that the SAFE solar array technology is ready for application and that new methods are available to assess the dynamics of large structures in space.

17. KEY WORDS	18. DISTRIBUTION STATEMENT
Solar arrays, large space structures, dynamics, remote dynamic sensing techniques, solid state trackers.	Unclassified - Unlimited Subject Category 20

19. SECURITY CLASSIF. (of this report)	20. SECURITY CLASSIF. (of this page)	21. NO. OF PAGES	22. PRICE
Unclassified	Unclassified	72	A04

For sale by National Technical Information Service, Springfield, Virginia 221

NASA-Langley, 19